SYSTEMS FOR NONINVASIVE ASSESSMENT OF BIOMECHANICAL LOAD IN THE LOWER LIMB

A Dissertation
Presented to
The Academic Faculty

by

Nicholas B. Bolus

In Partial Fulfillment
of the Requirements for the Degree
Doctor of Philosophy in
Bioengineering

Georgia Institute of Technology
May 2020

SYSTEMS FOR NONINVASIVE ASSESSMENT OF BIOMECHANICAL LOAD IN THE LOWER LIMB

Approved by:

Dr. Omer Inan, Advisor
School of Electrical and Computer Engineering
Georgia Institute of Technology

Dr. Gregory Sawicki
School of Mechanical Engineering
Georgia Institute of Technology

Dr. Young-Hui Chang
School of Biological Sciences
Georgia Institute of Technology

Dr. Aaron Young
School of Mechanical Engineering
Georgia Institute of Technology

Dr. Geza Kogler
Masters in Prosthetics and Orthotics Program
Kennesaw State University

Date Approved: April 14, 2020

To Mom, Dad, David, Michael, and Vince.

May we never grow apart, no matter the distance.

ACKNOWLEDGEMENTS

Looking back on these five years, I arrive at a simple truth: that this has all been a lesson in perseverance, faith, and gratitude.

Not many PhDs have the good fortune to work under someone like Dr. Omer Inan. Despite the fact that I came from an entirely different background with very little research experience, he put his faith in me and gave me the chance to prove myself. As my advisor, he was always there to offer me guidance, technical assistance, excessive patience, helpful brainstorming sessions, freedom to pursue at-times hairbrained ideas, prompt replies to purchase requests, and incisive writing critiques (sorry if I left any "in order to"s in here!). As my friend, he was there to provide moral support, much-needed votes of confidence, gallons of coffee, and a hearty guffaw.

I would like to extend my thanks to all members of my committee: Drs. Young-Hui Chang, Geza Kogler, Greg Sawicki, and Aaron Young. Each of you has rendered a unique and helpful perspective, and you have offered more than your fair share of time and effort to helping me think through problems and shore up knowledge gaps of my own. I am honored to have worked with many of you on various projects and manuscripts, and I am excited to see what future collaborations are in store between the Inan Research Lab and you wizards of biomechanics.

Speaking of the Inan Research Lab, I would be remiss not to mention my fellow IRLers, many of whom have become dear friends, and all of whom I have plagued with inane conversation and often unhelpful answers over the years. Because I have reason to thank

each and every one of you, please allow me to do so (and forgive me if I've forgotten anyone—what a massive lab!). Thank you, Andrew Carek. Thank you, Caitlin Teague. Thank you, Sinan Hersek. Thank you, Dotun Ode. Thank you, Daniel Whittingslow. Thank you, Brandi Nevius. Thank you, Mohsen ("Mohsy") Safaei. Thank you, Venu Ganti. Thank you, Hyeon Ki Jeong. Thank you, Samer Mabrouk. Thank you, Nil Gurel. Thank you, Kristy Scott Richardson (congratulations!). Thank you, Hewon Jung. Thank you, Mobashir ("Mobster") Shandhi. Thank you, Beren Semiz. Thank you, Sevda Gharehbaghi. Thank you, Jacob Kimball. Thank you, Jon Zia. Thank you, Asim Gazi. Thank you, Nordine Sebkhi. Thank you, newer members of the lab: Keaton Scherpereel, Goktug Cihan Ozmen, David Lin, Daniel Hochman, and Arpan Bhavsar. Thank you to the early members of the lab: Hazar, Jambu, Hakan, Abdul, Ozan, Lara, and especially Jordan. Thank you to my superstar undergrad, Bradley Blaho. Thank you to my friends from other labs, including Krishan Bhakta, Amrit Kashyap, Yogi Patel, Matt Wittbrodt, and Chris Waiblinger.

I must thank a few lab mates in particular, though. First and foremost, I want to thank Caitlin for sitting across from me and suffering my interminable anecdotes and petty quibbles for five whole years. She has been a constant presence and an immense help in more ways than she realizes, and I am truly grateful. Even though he roots for the wrong team, I have to thank Carek for being such a stalwart friend, eager brainstorming partner, and occasional rival during my time here. I hope your spelling skills have improved. Let's see if Dabo comes on home when he's called. A sincere thanks to Hyeon Ki and Keaton, with whom I've thoroughly enjoyed working closely over the past year. Thank you to Venu, Brandi, and Dotun for the hilarious and monotony-breaking conversations. Thank you to Mohsen for being a great mentor, even in so short a time. Thank you to Daniel

Whittingslow for being a dependable friend and consultant on all things medical (and for giving me the chance to bag my first deer!).

I would also like to thank Laura Paige, the academic advisor for Bioengineering. She was the very first voice I heard from GT when I called to inquire about the BioE graduate program in my junior year of college, and she has been a source of abiding positivity and exuberance since.

It would take me far too long to list all the friends and extended family from life before GT who have provided me with the memories, love, and support that I needed to get by, but rest assured that you are all in my mind and in my heart. One whom I couldn't possibly leave unmentioned is my Sitty, who has given me so much over the course of my life, but particularly in the last five years—a bed to sleep on, a feast three meals a day, a care package that fills up my car's trunk, and a loving embrace every time I come back home.

But most importantly, I want to thank my family. I have begun to realize just how rare it is for a family to be as close as we are. Without your support and unwavering confidence in me, especially when I lacked it myself, I would never have made it through. Vince – you brighten up every interaction you take part in, and you are the wellspring of joy in our family. The motto really has become "What would we do without Vince?" David – you're the smartest person I know (with one obvious exception) and also the most compassionate. Your advice on meditation, yoga, and Daoism truly helped me through some rough times, and I admire your intimidating level of creativity and ability to draft Pulitzer-worthy text messages in a matter of seconds. Dad – it should be obvious that you're

the #1 smartest person I know, and you're also my greatest role model. Every morning I have the classic Dadisms ringing in my ears, and I will carry them with me always. Mom – nobody has carried me through more troubled waters than you. It's funny how, even with a simple phone call from half a world away, you know just what to say. You have the selflessness of a saint, but you're way funnier than any saint ever was.

More than anyone, though, I want to thank Michael. My brother, my roommate, my best friend. We have now lived together 25 of my 27 years, which may seem strange to some, but I wouldn't have had it any other way. I came to GT, in part, because you made it feel like home, and because I knew I would always have someone there to rely on, to celebrate and commiserate with, to run ideas by, to play music with, to do stupid impressions with, to make the same three dinners over and over with, to watch the same three TV shows over and over with, to serve as a role model for hard work and perseverance—all of which kept me going. For the sake of earnest adulthood, we will move out, but I pray we never move on.

TABLE OF CONTENTS

LIST OF TABLES

LIST OF FIGURES

estimates of knee JRF and tibial vibration response characteristics and (c) the potential for real-time estimation of JRF during walking.

LIST OF ABBREVIATIONS

ADL	Activities of daily life
AFO	Ankle-foot orthosis
AT	Achilles tendon
CI	Confidence interval
COP	Center of pressure
CV	Cross-validation
DAQ	Data acquisition unit
DF	Dorsiflexion
DFR	Dorsiflexion resistance
DOF	Degrees of freedom
EMG	Electromyography
EOM	Equation of motion
FE	Flexion-extension
FPGA	Field programmable gate array
FSR	Force-sensing resistor
GRF	Ground reaction force
GUI	Graphical user interface
iAFO	Instrumented ankle-foot orthosis
ICC	Intraclass correlation
IMU	Inertial measurement unit
JRF	Joint reaction force
LOSO	Leave-one-subject-out

LRA	Linear resonance actuator
MDF	Median-normalized frequency of the power spectrum
MEMS	Microelectromechanical system
ML	Machine learning
PF	Plantarflexion
PFR	Plantarflexion resistance
R^2	Coefficient of determination
RMS	Root-mean-squared
RMSE	Root-mean-squared error
ROM	Range of motion
SD	Standard deviation
SNR	Signal-to-noise ratio
TA	Tibialis anterior

SUMMARY

Every move you make—and, yes, every step you take—is the result of action at a joint, and so proper joint function is pivotal to the way we explore and interact with the world around us. Unfortunately, joint function is often disrupted by injuries, chronic disorders, or neurological deficits, which can, in turn, disrupt quality of life. Many forms of joint dysfunction derive from adverse biomechanical loading conditions—that is, the forces and torques to which our limbs are subjected—and, thus, techniques for monitoring these loads during daily life may improve our understanding of how injuries and disorders arise and progress—and, most importantly, how best to treat them.

The standard methods for assessing these loading conditions, however, are almost all benchtop-bound and confined to laboratories or clinics, so their utility in at-home or ambulatory settings—where they may be most impactful—is limited. In an attempt to address this void, in this work, we present three novel techniques for extracting information related to joint loading using a synthesis of noninvasive / wearable sensing and machine learning. First, we detail the development of an adjustable-stiffness ankle exoskeleton with multimodal sensing capabilities and use it to explore how humans interact with external elastic loading of the ankle during walking. Then, in an attempt to peer "under the skin," we develop a novel form-factor for capturing joint sounds—the skin-surface vibrations produced by articulating structures internal to the joint—and demonstrate that these noninvasive measurements can be used to discriminate levels of axial loading at the knee. Finally, taking the concept of joint acoustics one step further, we introduce a new, active acoustics-based technique whereby the tensile loading of a particular tissue—the Achilles

tendon—can be estimated by measuring the tissue's mechanical response to a burst vibration on the skin surface. Using this approach, we are able to assess this loading state (and, by association, the net moment at the ankle) reliably across several activities of daily life, and, through a proof-of-concept study, we demonstrate how the technique can effectively translate to a fully wearable device.

Collectively, the efforts reported in this thesis represent a novel, multi-path approach to assessing biomechanical loading states in the lower limb and the effects thereof. These tools and insights may serve as a basis for future development of wearable, accessible technologies for monitoring joint load during daily life, thereby reducing injury risk, tracking disease progress, assessing the efficacy of treatment, and accelerating recovery.

CHAPTER 1. INTRODUCTION

1.1 Motivation

Injuries, neurological disorders, and other chronic conditions affecting joint function are prevalent and degrade quality of life for millions of individuals [1]–[3]. For those affected, joint health and function are assessed nearly exclusively during clinical visits—which occur relatively infrequently, if at all, and often involve costly tests and/or subjective evaluations. Wearable, unobtrusive, and accessible technologies for monitoring the functional status of joints and their associated tissues over time could provide valuable subclinical information as to an individual's injury risk, response to treatment, and rehabilitation progress.

Importantly, mechanical loading of joints—the forces and torques to which they are subjected—is central to many aspects of joint health such as acute injury onset (e.g., joint sprain, tendon rupture), disease progression (e.g., osteoarthritis (OA), plantar fasciitis), injury rehabilitation (e.g., bracing, functional exercises), and assistive strategies for functional impairments (e.g., orthoses) [4], [5] (Figure 1). The joints of the lower limbs are particularly susceptible to adverse loading effects due to their role in weight bearing and their high-volume, cyclical exposure to mechanical stress [6]. Thus, wearable methods to assess joint loading and the effects thereof may provide deeper insight into how best to mitigate and treat lower-limb joint dysfunction, accelerating an individual's rate of recovery or generally improving quality of life. Dysfunction aside, as these loading states dictate how we move and interact with our environment, developing a better understanding of these loading conditions could yield valuable insight into motor behaviors in general.

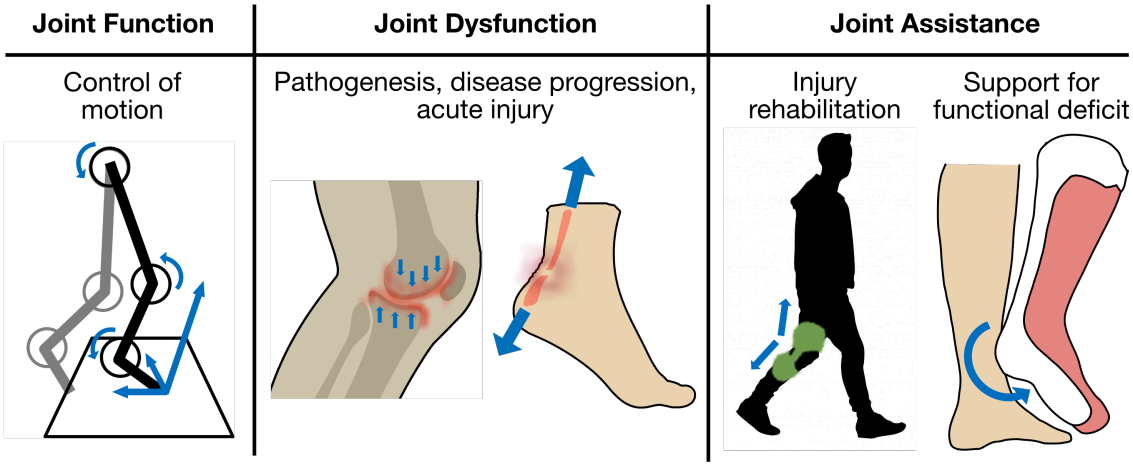

Figure 1. Role of biomechanical loading in joint function.

Table 1. Selection of musculoskeletal impairments, their prevalence, and the role of biomechanical load in their etiology.

Pathology	Epidemiology	Role of mechanical loading
Osteoarthritis	32.5M in US [1]	Caused by cyclical stress on bones at a joint
Ankle sprain	> 2M per year in US (15% of all injuries in athletics) [7]	Caused by out-of-plane joint moment → excess ligament stress
Achilles tendon rupture	1M athletes per year [8]	Caused by sagittal plane ankle moment → excess tendon stress
ACL tear	250K per year in US [9]	Caused by out-of-plane joint moment → excess ligament stress
Plantar fasciitis	1M doctor visits per year in US [10]	Caused by cyclical stress on fascial tissue
Foot drop	~20% of stroke survivors (among others) [11]	Characterized by insufficient ankle dorsiflexion moment

In general, measuring biomechanical load on a limb is a difficult task. For instance, to calculate a net joint moment during walking using the conventional gait analysis approach requires knowledge of the full 3-D kinematics of the lower limbs (acquired via video motion capture) and ground reaction force/moment vectors (measured by a force plate system installed in the floor) to inform an inverse dynamics model of the limb [12].

And even then, this approach only yields a *net* moment and is therefore agnostic of co-contraction—an important feature of the neuromuscular system—as the moments produced by agonist and antagonist muscles will cancel out [13]. Estimation of internal joint reaction forces adds yet another layer of complexity and assumptions on top of the inverse dynamics [14]. In either case, the instrumentation required to calculate these values is extensive, expensive, and unsuitable for any application outside the lab or clinic. The same can be said of implantable load sensors [15], [16], which are rarely used (almost exclusively in research settings) and which also entail the usual detriments of invasive techniques (i.e., need for surgical intervention, pain, risk of complication).

Despite these limitations in the current technological standard, and despite the weight of the challenge, there currently exists a void of wearable or out-of-lab / out-of-clinic solutions that are capable of effectively monitoring biomechanical loading parameters of the lower limb during activities of daily life (ADL). The work reported herein represents three novel approaches to addressing this technological gap through a combination of noninvasive sensing techniques.

1.2 Major Contributions of This Work

The core theme of this work is the development of wearable, minimally obtrusive technologies to estimate loading conditions at the ankle and knee. We have worked toward this objective, in part, by developing three devices that capture unique information from noninvasive sensors and relating these data to either (1) an external elastic load at the ankle, (2) axial load through the knee, or (3) tensile load in the Achilles tendon (AT). In specific, the following represent the major contributions of this thesis:

1. We designed, built, and validated a first-of-its-kind exoskeletal device with both multimodal sensing and adjustable stiffness capable of mimicking the function of the conventional ankle-foot orthosis (AFO) for the purposes of measuring, through a rich set of clinically useful biomechanical parameters, humans' response to an external stiffness at the ankle.
2. We developed a novel technique for reliably acquiring joint acoustical emissions using a hand-worn system and validated it alongside conventional techniques by demonstrating its ability to discriminate mechanical loading states of the knee.
3. We designed and validated a novel technique for noninvasively estimating the loading state of the AT across a variety of ADLs by measuring the tendon's response to burst vibrations on the skin surface.

1.3 Document Organization

The work presented in this thesis is grouped thematically based on the major contributions detailed above. As the central concept of "load estimation in the lower limbs" is rather broad, information that is common amongst the major contributions is discussed in CHAPTER 2 ("General Concepts"), including overviews of the relevant anatomy and physiology of the lower limbs (and the role of mechanical loading therein), basic mechanics of locomotion, conventional techniques for noninvasive biomechanical sensing, the as-yet unconventional technique of joint acoustics, and the general machine learning (ML) framework used to estimate loading states from wearable sensor data. Within each of the subsequent three chapters, since each one concerns a unique device or technique, you will find chapter-specific introductory information and concluding statements. CHAPTER 3 concerns the development of an exoskeletal device, the Instrumented Ankle-

Foot Orthosis ("iAFO"), for measuring the effect of an external load on the mechanics of the ankle joint. To move the challenge of estimating load "underneath the skin" (i.e., to determine a biological load as opposed to one applied by an exoskeleton), we explore the potential of joint sounds as a biomarker of knee loading through the use and validation of a custom-designed, vibration-sensitive glove ("Phalanx") in CHAPTER 4. Then, in CHAPTER 5, we focus more specifically on estimating the load in a particular tissue (the AT) through the use of a novel active acoustics technique ("Patroclus"). Finally, in CHAPTER 6, we provide net conclusions, discuss potential long-term impacts of this work, and propose future efforts for which this thesis may serve as a basis.

1.4 Chapter Summaries

CHAPTER 3. In this chapter, we will detail the development and use of the iAFO [17], a clinical assessment tool designed to quantify the effects of selectively altering orthotic ankle joint stiffness, particularly for individuals with locomotor deficits such as foot drop. In Section 3.2, we will discuss the sensing capabilities of the system, which include ankle joint kinematics and kinetics, electromyography, and orthosis interface pressures. We will further describe the mechanical design of the device, which allows for user-defined manipulation of orthotic stiffness through an interchangeable extension spring mechanism. Initially, we will demonstrate the capabilities of the iAFO's full sensor suite by presenting results both of benchtop testing and of a preliminary human-subject study. Expanding upon this initial validation study, in Section 3.3 we will use the iAFO as a scientific tool to explore how humans interact with an external stiffness at the ankle during locomotion. Using the data collected by the iAFO, we will establish relationships between exoskeletal joint stiffness and ankle joint mechanics during walking. Using ML techniques, we will

present a regression model capable of reliably estimating the stiffness applied to the joint based solely on information derived from a joint angle sensor.

CHAPTER 4. This chapter marks a crossing of a threshold into the concept of acoustical / vibrational analysis for assessing loading states in the leg. In it, we will explore the use of a novel form factor for non-invasively acquiring acoustic / vibrational signals from the knee joint: an instrumented glove with a fingertip-mounted accelerometer [18]. We will present a validation of the glove-based approach by comparing it to conventional mounting techniques (tape and foam microphone pads) in an experimental framework previously shown to reliably alter healthy knee joint sounds: the vertical leg press. Measurements from healthy subjects (N = 11) in this proof-of-concept study demonstrate a highly consistent, monotonic, and significant ($p < 0.01$) increase in low-frequency signal root-mean-squared (RMS) amplitude—a straightforward metric relating to joint grinding loudness—with increasing vertical load across all three techniques.

CHAPTER 5. In contrast to the work performed in CHAPTER 4, a "passive" acoustics approach to assessing joint load (i.e., simply listening to the sounds produced by joint articulation), in this chapter we will employ an "active" approach, whereby we control the vibrational input to a tissue and measure its response. Specifically, we will present a novel method of noninvasively estimating tension in the AT using burst vibrations. These vibrations, produced by a small vibration motor on the skin superficial to the tendon, are sensed by a skin-mounted accelerometer, which measures the tendon's response to burst excitation under varying tensile load. In this study, healthy subjects (N = 12) perform a variety of everyday tasks designed to expose the AT to a range of loading conditions. To approximate the vibration motor-tendon system and provide an explanation for observed

changes in tendon response, a 2-degree-of-freedom mechanical systems model is developed. Reliable, characteristic changes in the burst response profile as a function of AT tension are observed during all loading tasks. Similar to CHAPTER 3, using an ML-based approach, we develop a regression model capable of accurately estimating tendon tension across a range of walking speeds and across subjects ($R^2 = 0.85$). Simulated results of the mechanical model accurately recreate behaviors observed *in vivo*. Finally, preliminary, proof-of-concept results from a fully wearable system will be presented that demonstrate the potential of this technique to monitor AT loading outside the confines of a lab during ADL.

CHAPTER 2. GENERAL CONCEPTS

2.1 Anatomy, Physiology, and Pathophysiology of the Lower Limbs

2.1.1 The Ankle Joint

The ankle is a complex synovial joint with three degrees of freedom, allowing relative rotation between the shank and foot segments of the lower leg, primarily in the sagittal plane (Figure 2). It is actuated mainly by four muscles: the triceps surae (medial gastrocnemius (MG), lateral gastrocnemius (LG), and soleus)—often collectively referred to as the "calf"—which act as joint extensors (extension in the sagittal plane of ankle joint rotation is referred to as plantarflexion (PF)), and the tibialis anterior (TA), which acts as a joint flexor (flexion of the ankle joint is referred to as dorsiflexion (DF)). The ankle joint is surrounded by many soft tissues, including the AT (chiefly important for this work), into which the triceps surae flow, which inserts at the calcaneus (heel bone).

The ankle joint is particularly important for generating positive work during walking (mainly through activation of the calf and recoil of energy stored in the AT), as it is estimated that about half of the power generated in the lower limbs during a typical step is attributable to ankle action [19]. The ankle, being the major joint of the lower limb most proximate to the ground, is also critical for negotiating changes in terrain and also happens to be the most commonly injured joint in the body [1]. Injuries or disorders in tissues associated with ankle joint function (e.g., the AT or TA) therefore greatly affect stability and efficiency of locomotion, which can have a deeply detrimental impact on an individual's quality of life [20].

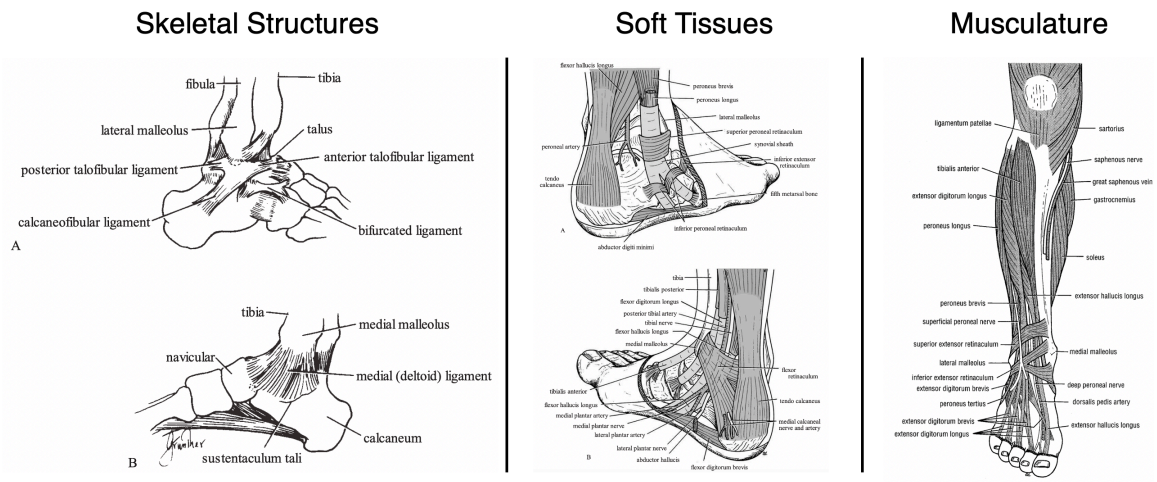

Figure 2. Anatomy of the ankle joint. Adapted from [21]**.**

2.1.2 The Knee Joint

The knee is a synovial hinge joint that allows for relative rotation between the thigh (femur) and shank (tibia) segments of the leg (Figure 3). It is a complex structure with an intricate arrangement of soft tissues for stabilization and permittance of polycentric motion. It is actuated predominantly in the sagittal plane by a set of flexor (hamstrings) and extensor (quadriceps) muscles. Joint articulation involves contact between the distal end of the femur, the proximal end of the tibia, and the patella, which tracks in the groove between the medial and lateral femoral condyles. This articulation is mediated by several structures, including the meniscus, which is a soft tissue that sits atop the tibial plateau and acts as a mating surface between the femur and tibia; the joint capsule, which is a fibrous membrane that lines the inner surfaces of the joint and contains lubricating synovial fluid; and four stabilizing ligaments.

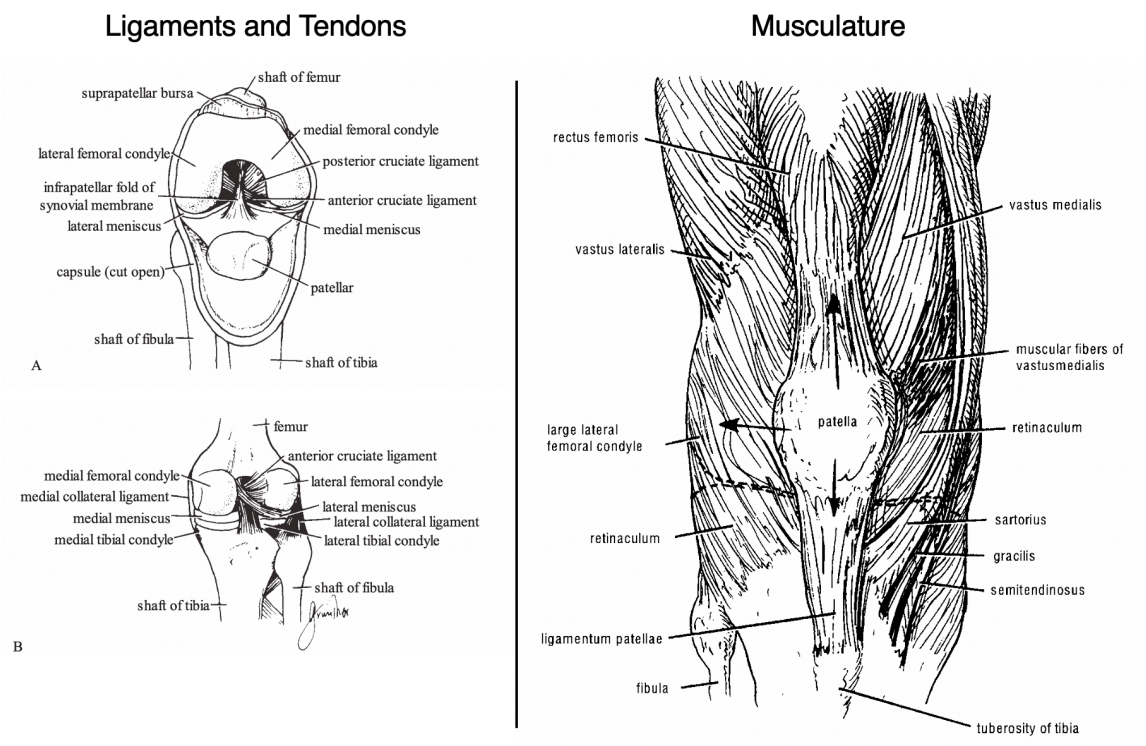

Figure 3. Anatomy of the knee joint. Adapted from [21]**.**

During locomotion, the knee is especially important as a dissipator of energy, performing negative work to absorb the energy of collision between steps and to decelerate the forward motion of the lower leg caused by inertia and interaction torques when the limb is not in contact with the ground [20]. As a consequence of its prime role in weight bearing and its exposure to high, repetitive mechanical stress, coupled with its complex structure and limited DOF, the knee is particularly susceptible to injury [20].

2.1.3 Joint Load: Definition, Origin, and Implications

In this work, we define "joint load" broadly, referring to any force or moment acting at a joint. (*NB*: The terms "torque" and "moment" represent the same phenomenon—the rotational effect of a force acting at a distance from a rotation center—and are used

interchangeably.) These loads can either originate within the body ("internal" or "biological" loads) or stem from interactions with the environment ("external" or, as in CHAPTER 3, "exoskeletal"). Biological joint loads come as a consequence of muscle contraction or, in some cases, passive mechanics of tendons, ligaments, skin, and other non-contractile tissues. Contraction of muscle across a joint produces a torque—as the muscle force line of action lies some moment arm distance away from the joint center—as well as a reaction force between the bones that meet in the joint space, which we will refer to as joint reaction force (JRF). External joint loads might be caused, for instance, by the weight of a backpack compressing the spinal vertebrae, a stiff knee brace producing a reaction torque to resist joint motion, or the ground pushing back up on the bottom of the foot during walking. External loading states are often easier to measure than internal loading states simply because they are easier to access, whereas internal loads require invasive techniques (e.g., tendon buckles or implantable strain gages [16])—which are considered the bona fide "ground truth"—or else some modelling component built on top of knowledge of external loading conditions (e.g., inverse dynamics, neuromuscular / musculoskeletal models, calibrated radiography / ultrasound). Joint loads exist in three dimensions (i.e., in all three planes of joint rotation), though the vast majority of work in this thesis will focus on sagittal plane mechanics.

In this thesis, we also consider the loading state of specific tissues—in particular, tensile loading of the AT. As this parameter is not a "joint load," per se, we will use the umbrella term "biomechanical load" to refer to the mechanical loading state of any tissue or joint treated as a target variable. To be explicit, these targeted biomechanical loads include (external) elastic load at the ankle (CHAPTER 3), (external) axial load at the knee

(CHAPTER 4), (internal) tensile load of the AT (approximated by biological joint torque at the ankle) (CHAPTER 5), and (internal) JRF at the knee (by way of internal reaction forces on the tibia) (Section 6.3) (see Table 2).

Table 2. Biomechanical loads targeted in this work and the noninvasive techniques used to assess them.

Chapter / Section	Biomechanical load of interest	Related / estimated parameter	Noninvasive technique / measurement
CHAPTER 3	Exoskeletal ankle reaction moment	Stiffness of elastic exoskeleton	Ankle angle
CHAPTER 4	Knee JRF	Leg press weight	Passive acoustics (joint sounds)
CHAPTER 5	AT tension	Net ankle moment	Active acoustics
Section 6.3	Knee JRF	Tibial force	Active acoustics

To reiterate, it is important to understand the loading conditions under which our body operates, as these govern how we move, how injuries and other pathologies arise, and how we might recover from them.

2.1.4 Joint Pathologies

Out of the litany of possible joint dysfunctions, the three main types that warrant discussion in this thesis include (1) neuromuscular impairments, (2) acute musculoskeletal injuries, and (3) osteoarthritis (OA). These conditions are of particular interest since they either are the direct result of excessive / irregular mechanical load and/or have a direct impact on the body's ability to generate suitable joint loads to accomplish tasks such as walking. As such, they represent the clearest clinical targets for the work presented herein.

Neuromuscular impairments arise from a failure of the nervous system to communicate properly with the musculature that it innervates. The pathogenesis is quite broad, as these deficiencies can be caused by acute damage to the nerve itself (i.e., trauma), genetic factors (e.g., muscular dystrophy, Charcot-Marie-Tooth disease), infection, diabetes, and even pregnancy [22], [23]. One deficit that is a particular motivation for the work in CHAPTER 3 is known as "foot drop" (or "drop foot"), which is characterized by paresis (weakness) or paralysis of the ankle dorsiflexors (e.g., TA) often caused by lesion of the peroneal nerve, resulting in an inability to lift the foot up [22]. This condition, which can either be permanent or recoverable, can make many locomotor tasks difficult, heightening the risk of tripping and falling and significantly increasing the metabolic cost of walking [22]. The standard treatment for this condition, as well as many other neuromuscular deficits, is the use of a brace—also called an "orthosis"—to stabilize the limb and mitigate gait deviations. More details on foot drop and orthosis prescription will be discussed in Sections 2.1.5 and 3.1.1.

Musculoskeletal injuries are caused by excessive mechanical stress in tissues of the musculoskeletal system (i.e., bones, muscles, tendons, and ligaments) leading to acute damage. Studies suggest that proper monitoring of the stresses in these tissues could help mitigate injury risk and accelerate recovery [24]–[27]. A very common and debilitating injury affecting the lower limb—and one which heavily motivates the work presented in CHAPTER 5—is rupture of the AT [28]. This tendon is subjected to some of the highest loads in the human body and is critical for proper gait function [29]. It is also a very prominent, superficial, and accessible tissue, making it a prime candidate for mechanical

assessment via a wearable system. More details on this particular type of injury and our approach to monitoring its loading state will be elaborated in CHAPTER 5.

OA is the most common form of arthritis (joint inflammation) and is caused by "wear and tear" (i.e., repetitive loading) on a joint, leading to cartilage damage, deterioration of bone and other connective tissues around the joint, and inflammation of the joint lining [30]. These defects can induce joint pain, stiffness, and swelling and can lead to other comorbidities [31]. As mentioned above, monitoring of joint loading parameters could allow one to track the volume of mechanical stress affecting the joint and thus meter activity levels or inform other therapeutic strategies for mitigating the effects of OA, which is the central thrust behind the work presented in CHAPTER 4 relating knee joint load to joint acoustic parameters acquired noninvasively at the skin surface.

2.1.5 Orthoses: Wearable Joint Load Manipulators

A common clinical approach to manipulating the mechanical load on a joint is through the use of an orthosis. An orthosis—effectively, a brace—is a wearable device that controls joint motion by applying external loads to a skeletal structure, with the goal of rectifying some functional impairment. These devices provide a simple, effective, nonoperative treatment for myriad neuromuscular and musculoskeletal deficits [32], [33]. Orthoses can be used to reduce the reaction forces at the articular surfaces of a joint, offload some of the mechanical work normally performed by muscles, and correct skeletal misalignments. Improvements to gait mechanics as a result of orthotic intervention are generally quite apparent and have been studied in some detail [34]–[38].

However, precisely how an orthosis ought to manipulate joint loading conditions depends on the nature of the impairment and on user priorities. For instance, an individual with osteoarthritis in the knee might use a knee orthosis to decrease the peak joint reaction forces that occur when the foot impacts the ground each stride. An athlete recovering from an injury may benefit from a brace that tapers joint constraint over the course of rehabilitation, thereby maximizing allowable range of motion and minimizing muscle atrophy over time. An individual with a neuromuscular deficit known as foot drop might primarily need an AFO to provide enough external torque to keep the foot up during the swing phase of gait, thereby providing toe clearance and reducing the risk of tripping. To take AFOs for the treatment of foot drop as a test case, studies suggest that patient-matching of AFO stiffness can significantly improve individual outcome measures [39]–[41], and improper device mechanics can cause discomfort and exacerbate gait deficits, potentially leading to muscle disuse (and eventual atrophy) and reduced patient compliance [42]–[45]. These findings suggest that properly manipulating the loading conditions at an impaired joint can significantly improve joint function in tasks such as walking. Whatever the circumstance, proper management of joint impairment will require knowledge of the loading conditions at a joint and the functional consequences thereof.

2.2 Locomotion Mechanics

2.2.1 Gait Cycle Definitions

As much of the work reported in this thesis is performed in the context of locomotion, we will define some relevant terms associated with gait biomechanics. We define ankle angle, θ_a, as the angular displacement of the ankle joint from the anatomical neutral position

($\theta_a = 0°$), which is defined as when the shank and foot segments are perpendicular. DF ($\theta_a > 0°$) refers to the act of lifting the foot up towards the shank, while PF ($\theta_a < 0°$) refers to the act of pointing the toes downward. The anatomically neutral angular position of the knee ($\theta_k < 0°$) is defined as when the thigh and shank segments are collinear (i.e., straight-legged); knee flexion is defined as the act of making the angle between the thigh and shank more acute, while knee extension brings the limb closer to the neutral position.

Each gait cycle, or stride, is comprised of a series of "phases" (Figure 4) to which we will refer throughout this document. We discriminate gait phases based on either changes in ground reaction force (GRF)—the equal-and-opposite force between the ground and the foot during locomotion—or inflection points in the ankle angle waveform, which signify distinct changes in GRF at the heel and toe (the so-called ankle "rockers" of the gait cycle [20]). Each gait cycle begins at initial contact (also referred to as "heel strike"), which denotes the beginning of stance, the phase of gait in which the foot is in contact with the ground. "Loading response" (~0-10% gait) (also called "weight acceptance") is the phase of gait in which the limb absorbs the energy associated with the foot colliding with the ground and in which body weight is transferred onto the leg through both ankle PF and, more importantly, knee flexion. (Individuals with foot drop often suffer from "foot slap" during this phase of gait, as the TA is unable to generate forces to decelerate the foot through eccentric muscle contraction.) Once the plantar surface of the foot is fully on the ground ("foot flat"), the tibia begins to process over the ankle joint in the phase of gait we will refer to as "mid-stance." This phase ends when the ankle achieves peak DF and the heel begins to lift off the ground ("heel rise"), signifying the beginning of "terminal stance," or "push-off," which is the propulsive phase of gait characterized by rapid ankle

PF due to elastic recoil of the AT and activation of the calf muscles, which generate considerable positive mechanical power. (Disruption of AT mechanics can therefore have a markedly negative effect on locomotor performance.) Once peak PF is reached, the toes lift off the ground ("toe off") and the limb enters the swing phase of gait (when the foot is no longer in contact with the ground). (Individuals with foot drop often present gait deviations here, as they have difficulty achieving toe clearance, leading to "toe drag," which often results in tripping or drives less efficient strategies such as hip circumduction or "hiking" the knee). During swing, the knee joint reaches peak velocity in flexion, which is decelerated by eccentric contraction of the hamstrings, and ankle DF is decelerated either by eccentric contraction of the calf or by passive stretch of the AT, both of which stabilize the limb in preparation for the next step.

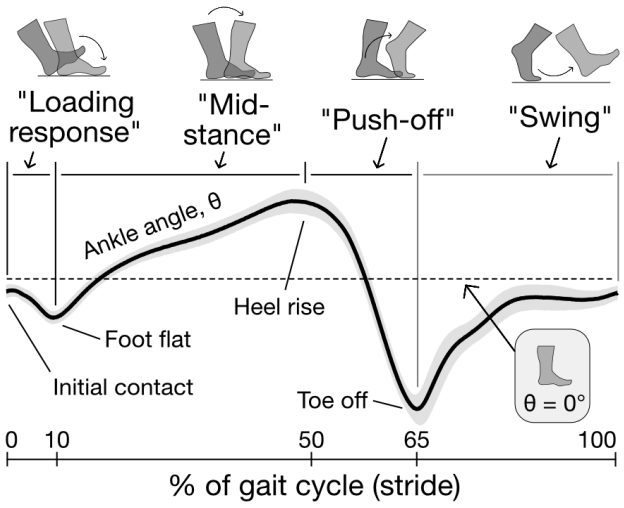

Figure 4. Definitions of gait phases and events pertaining to ankle motion during normal, level walking.

Throughout this document, we will refer to features of gait related purely to motion (e.g., joint angle, velocity, and acceleration) as "kinematic" and those related to the loading

conditions that cause motion (e.g., joint torques, reaction forces) as "kinetic." The term "mechanics" refers to the combination of these two terms.

2.2.2 Sensing in Gait Analysis

Throughout this work, we use a variety of different approaches for measuring kinematics (motion information) of the lower limbs. The "gold standard" in conventional gait analysis remains video motion capture, in which subjects are instrumented with retroreflective markers at various anatomical landmarks on the limbs; the positions of these markers are tracked in space using cine cameras, and with a coordinate system of the capture space defined, these positions can be used to derive full 3D kinematics of the joints and segments of the human body. An increasingly common kinematic sensor is the inertial measurement unit (IMU), which is a device that contains a 3-axis accelerometer (measuring linear accelerations), a 3-axis gyroscope (measuring angular velocities), and often a 3-axis magnetometer (measuring orientation / heading relative to the Earth's magnetic field). IMUs are popular for use in wearable systems due to their low footprint, relatively low power consumption, and ease of integration, as algorithms have been developed for calculating joint angles without the need for strict placement schemes [46] or the additional mechanical hardware that shaft-type encoders and potentiometers require. Rotary encoders and potentiometers offer a simple and accurate solution for 1-DOF systems, as they rely on the rotation of a shaft to measure angular displacements. We performed a thorough comparison of different types of rotary encoders and potentiometers [47] (Figure 5) before selecting the sensors used in the iAFO, which will be discussed in further detail in Section 3.2.

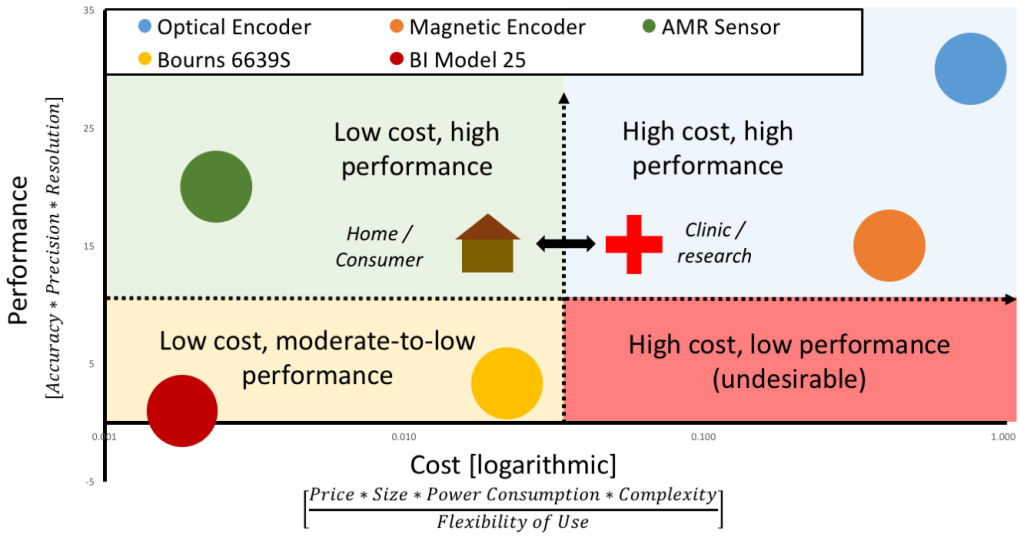

Figure 5. "Performance" versus "cost" analysis chart for various shaft-type angle sensing modalities.

GRF is conventionally measured using force plates, which are instrumented with load cells and are often integrated into treadmill systems such that GRF data can be collected continuously from step to step. Though this method is considered the gold standard, these systems are confined to laboratory environments. Wearable systems exist that are capable of capturing GRF and even plantar pressures underfoot using arrays of capacitive force sensors embedded in shoe insoles [48], [49]. (A similar style of capacitive sensor is used in CHAPTER 4 to measure accelerometer contact force as applied by the fingertip in a vibration-sensing glove prototype.) A more accessible option is to use force-sensitive resistors (FSRs), though these offer limited force resolution (or heavily restrictive full-scale force ranges which are incompatible with typical GRF magnitudes) and can be unreliable.

Joint moments can be calculated by way of inverse dynamics, which is a technique developed for robotics in which the torques at each joint of an articulated structure can be

directly calculated—assuming joint kinematics and endpoint forces are known—by way of a Jacobian matrix [12], [50]. This approach remains the most common amongst gait biomechanists, and many inverse dynamics algorithms have been previously developed and validated in the context of gait [51], [52]. The reaction moments produced by exoskeletal devices can be measured using a variety of strain gage-based sensors, such as the reaction torque sensor used in the iAFO.

Muscle activity is also often important to monitor during locomotion or other activities, and the most common method is to measure electromyography (EMG) on the surface of the skin. EMG is a signal that represents the collective (electrical) activation of a group of motor units, which are comprised of motor neurons and the muscle fibers that they innervate.

Wearable sensing represents a promising alternative to conventional, lab- or clinic-based techniques for biomechanics analysis (e.g., motion capture and force plates). By, for instance, instrumenting an orthosis with wearable sensors to monitor kinematics, kinetics, interface pressures, and/or muscle activity noninvasively, clinically relevant information could be acquired at home and used to monitor the user's biomechanical response to orthotic loading and potentially adjust these loading conditions over time to optimize treatment/recovery. And while these wearable sensing modalities can provide useful information, they do not (with the exception of EMG) directly reflect an underlying physiological state of the joint. They do not, for instance, provide information about the internal structure of the joint. To that end, recent work has demonstrated the viability of using the acoustical emissions produced by joints in motion—in particular, the knee—as an indicator of underlying joint health, which will be discussed below.

2.3 Joint Sounds

When a joint articulates, surfaces of structures within the joint (bones and other soft tissues) abrade against one another, producing vibrations that propagate into surrounding tissues and eventually reach the skin surface, where they can be detected noninvasively. The clinical potential of this phenomenon was perhaps first explored in 1902 when a physician named Blodgett used a manual stethoscope to auscultate the knee joint and observed idiosyncrasies in the sounds produced as the joint rotated [53], [54]. These sounds have a particular character and are often described as creaking (crepitus), grinding, clicking, clunking, popping, etc. Measurement of these sounds is sometimes referred to as vibroarthrography [55], [56] or vibration arthrometry [57], though our lab has adopted the term "joint sounds" or "joint acoustical emissions" (AEs) to refer to the acoustic response caused by internal vibrations measured at the surface of the knee.

Research conducted by members of the Inan Research Lab has previously demonstrated that joint sounds contain clinically useful information related to joint health and morphology [58]. In these studies, researchers demonstrated that features of AEs could be used to differentiate healthy and acutely injured knee joints and track joint health status over the course of rehabilitation in a cohort of athletes [59], [60], identify cases of juvenile idiopathic arthritis and gauge the effectiveness of therapeutic strategies in a longitudinal study in a rheumatology clinic [61]–[63], classify various stages of simulated meniscus tears in a cadaver model [64], and coarsely determine the level of axial load applied to the knee in healthy subjects [65].

Ongoing efforts from members of the lab include, among others, (1) the development of a fully wearable "smart brace" capable of acquiring joint sounds from the knee as well as measures of electrical bioimpedance, actigraphy and joint kinematics (through IMUs), and skin temperature; (2) translation of the joint sounds measurement technique to other joints (e.g., the wrist) and in other affected populations (e.g., individuals with rheumatoid arthritis); and (3) estimation of knee JRF during locomotion for potential use in control schemes of exoskeletons. All of these applications evince the potential use of joint sounds as a window into internal states of the knee—which have previously been almost solely accessible by medical imaging techniques (e.g., radiographs) or invasive interventions—using technology that is well suited to wearable form factors and ambulatory, at-home, or austere environments.

2.3.1 Sensing of Joint Sounds

Broadly speaking, AEs have previously been acquired in two ways: either with an air microphone placed some distance away from the skin surface or with a contact microphone / accelerometer coupled directly to the skin. The former is able to capture AEs that possess enough energy to overcome the impedance mismatch between skin and air (potentially discounting internal vibrations of lower frequency or amplitude), while the latter captures whatever accelerations are able to propagate to the skin surface (possibly mingling the effect of skin stretch or other artifact). The latter technique has been adopted as the standard for our research and is used as the means of acquiring acoustic information from tissues in this thesis. More detailed information can be found in Sections 4.2.1 and 5.2.2.

2.3.2 Analysis of Joint Sounds in Prior Studies

An extensive set of analysis techniques has been used in previous research for interpretation of AEs, from simple qualitative assessment / manual annotation [55], [56] to adaptive filtering [66], [67] to probabilistic models [68] to various machine learning classifiers built on extraction of temporal, amplitudinal, and spectral features [69]. Our lab has developed various biomarkers / scores related to joint health, most of which are based on sophisticated machine learning models such as unsupervised graph mining analysis [59] and boosting of regression trees (i.e., the XGBoost algorithm) [62], which use a rich set of acoustic features extracted from the local skin acceleration signals as inputs. The interpretability of these models remains a bit tenuous, though the general trend across studies appears to be that joints in a diseased or injured state produce AEs that are more complex and heterogeneous—and often simply "louder" on average—than do healthy joints. This result is somewhat intuitive and grounded in physiology, as any structural defects in an otherwise smooth and well-lubricated joint such as the knee would likely produce more spurious vibrations (clicking, popping, grinding, etc.) than the healthy case. As the analysis of joint acoustics in this thesis is focused on healthy subjects with no considerable deformities, these differences often become more nuanced and difficult to identify, as will be discussed in later sections.

2.4 Machine Learning: General Approach

Some central results of this thesis (i.e., that of Section 3.3 and CHAPTER 5) rely on the use of machine learning (ML) techniques to estimate a difficult-to-measure state based on information extracted from more accessible, wearable sensors. In both cases, we

performed *supervised* ML, which is a branch of ML in which both the input (predictor/s) and output (response / target/s) are known, and since our aim was to estimate continuous variables (i.e., orthosis stiffness and net ankle moment / AT load), we relied on the use of regression models (as opposed to classifiers, which sort data into discrete groups). Our general approach consisted of a series of 4 major steps: (1) feature extraction, (2) feature ranking / dimensionality reduction, (3) model selection and tuning, and (4) model evaluation.

The key challenge of step 1, which we found required the most time, ingenuity, and creativity, was to translate qualitative observations about the signal/s of interest (and how they change as a function of the target variable) into quantitative values, preferably with some basis in physical / physiological phenomena. We did this often by comparing waveforms side-by-side and identifying unique characteristics of each, which were generally based on attributes of signal amplitude, timing, or frequency content.

To avoid the so-called "curse of dimensionality" (sparsity of data relative to the number of features used to determine statistical significance) [70], [71], it is often necessary to reduce the dimensionality of the input feature space (i.e., whittle down the list of features used as inputs or fuse them together through projection into lower dimensions), which is the purpose of step 2. In our work, we chose to reduce the number of features by first ranking them in order of "importance," which is either defined in terms of information gain (as in Section 3.3.2.4) or in terms of the strength of correlation (e.g., coefficient of determination, R^2) from simple univariate linear regression (as in Section 5.3.3), and then selecting the top "performers." This approach also gave us more intuition about what

attributes of the input signals changed most significantly and reliably in response to changes in the target variable / test condition.

As ML is an increasing popular and rich area of study, the number of available regression algorithms is immense. Selecting and tuning a suitable model involves striking a balance between performance (i.e., estimation/prediction accuracy) and generalizability (i.e., avoidance of overfitting to one's dataset). During the model selection stage (step 3), we performed 10-fold cross validation (CV), in which a dataset is randomly divided into 10 subsets, 9 of which are used to train a model while the remaining one is reserved as a test set; this process is repeated 10 times such that each isolated 10% of the dataset is tested upon once. This approach helps to avoid overfitting to one particular tranche of one's data (though it has limitations in studies involving subject-specific responses to an intervention or test condition, a solution to which will be discussed in step 4), which allows models to be compared more favorably and with more confidence that the eventual model will generalize to unseen data, which is the ultimate goal of ML. The validation error from 10-fold CV (e.g., root-mean-squared error (RMSE) between the model estimation and the true output) is then used as the basis for selecting the final regression model for analysis (i.e., the model with the lowest validation error is selected). This same approach is used to tune the model's hyperparameters (e.g., for decision trees, these parameters include tree depth and minimum leaf size). The two models selected for use in this thesis are referred to as "extreme gradient boosting" ("XGBoost") and "bootstrap aggregation" ("bagging") of regression trees as employed in Sections 3.3 and 5.3.3, respectively. The detailed internal mechanisms of each algorithm are beyond the scope of this thesis, but they can be explored in associated references [72], [73].

Once a model is selected, it is then evaluated (step 4) on subject data by another form of cross-validation called “leave-one-subject-out” (LOSO). In LOSO-CV, instead of the dataset being randomly split, validation folds are comprised of isolated data from individual subjects; each subject takes a turn acting as the testing set for a model trained on the remaining subjects’ data, which simulates a real-world scenario in which a new subject (unseen data) is included in a study. Estimation performance is then quantified in terms of the strength of correlation (R^2) and error (RMSE) between ground truth values and those estimated by the model via LOSO-CV.

CHAPTER 3. IAFO: ELASTIC LOADING OF THE ANKLE AND ESTIMATION THEREOF

3.1 Introduction

3.1.1 Clinical Motivation: Optimizing Orthotic Interventions

Orthoses—wearable devices used to control joint motion and provide corrective support for, or improve the functionality of, impaired limbs/joints—provide a simple, non-operative, inexpensive, and effective treatment for myriad neuromuscular and musculoskeletal disorders [32], [33]. The most commonly prescribed orthosis is an ankle-foot orthosis (AFO) [74]. In many individuals with a loss of volitional lower limb motor function, an AFO can provide the necessary stability for standing and walking to enhance functional mobility for the user [34], [75], [76]. The inability to dorsiflex the foot (i.e., foot drop) is one of the most common lower limb conditions. Foot drop is associated with peripheral nerve injury, stroke, diabetes, and an array of neurological disorders such as multiple sclerosis and Charcot-Marie-Tooth disease [77]. With reduced ability to lift the foot up towards the shin and thus achieve toe clearance during the swing phase of gait, patients with foot drop often compensate for this deficit, leading to degeneration of normal gait mechanics. The resultant abnormal gait can engender both higher metabolic cost of walking and heightened risk of tripping and falling [22]. Use of lower-limb orthoses to provide stability is common in elderly populations, as the weakening of the ankle dorsiflexors compromises postural control and balance, increasing the risk of injuries caused by falls [78]–[80]. With the rising aging population and incidence of stroke [81],

the burden on the orthotics and orthopedics communities will undoubtedly grow heavier, presenting a need for more effective, affordable, and personalized home-use orthoses to improve patient mobility and safety.

AFOs have generally been shown to improve locomotor function (e.g., gait velocity, stride length, walking efficiency, balance) and mitigate injury risk in hemiplegic gait [35]–[38], [82], [83]. However, several studies have shown that, if the devices are not designed or fit properly, such improvements can be relatively insignificant and can in fact cause discomfort and further compromise gait mechanics, perhaps leading to muscle disuse (and eventual atrophy) and reduced patient acceptance of the intervention [39], [42], [44], [45], [84], [85]. Presently the methods for determining the proper amount of orthotic resistance are qualitative and subjective. An orthotist typically relies on experiential estimates of the AFO's stiffness by manually deflecting the orthosis, thereby assessing whether the device offers the requisite corrective forces to overcome the motor deficit (e.g., foot drop). The desired treatment outcome of "toe clearance during swing phase" is then clinically confirmed by observational gait analysis. Since the improvements in gait are generally so apparent when adequate resistance to foot drop— and thus swing-phase toe clearance—are achieved, little attention has been devoted to the optimization of orthotic resistance nor to the functional consequences of varying device stiffness—despite studies which have suggested that patient-matching of orthotic constraint of motion can significantly influence individual outcomes [39]–[41]. There lacks an objective way of observing and quantifying various parameters of gait in the clinic to identify an optimal set of orthosis properties for each patient, which may depend on the degree of paresis, paralysis, and spasticity of the lower limb as well as his/her anthropometrics and capacity for recovery. To address this

need, we propose the use of an instrumented ankle foot orthosis (iAFO) as a clinical assessment tool to monitor the gait parameters of individuals with disorders affecting movement of the ankle joint.

Numerous efforts have been made to develop powered, active, and adaptive orthoses to assist individuals with movement disorders [86]–[89], employing techniques such as biofeedback via functional electrical stimulation [90], [91], actuated robotic assistance [92]–[96], and variable-impedance joints [97], [98]. While these devices represent major scientific and engineering advances and indeed demonstrate potential as rehabilitation aids, they are currently bulky, complicated, expensive, and unconducive to mass production, making them presently unsuitable for home use. Therefore, in order to maximize clinical impact and most effectively address current patient needs, we elected to focus our work on the domain of passive AFOs.

To that end, the iAFO is a passive exoskeletal device comprising an orthotic control feature, which permits a clinician / researcher to modulate ankle joint stiffness with a series of interchangeable extension springs, study a patient's biomechanical response to such a perturbation, and ultimately identify and prescribe an optimal orthosis stiffness on a patient-specific basis (Figure 6). Our method for achieving modular orthotic stiffness—i.e., unilaterally applied extension springs—is analogous to the action of a commercial orthosis known as a posterior leaf-spring AFO. This AFO design relies on the elastic deformation of its constituent material (often carbon fiber, metal, or plastic) to control joint motion during walking. And though most solid-ankle AFOs constrain joint motion bidirectionally (in contrast to our design, which only imposes rotational resistance in one direction at a time), the iAFO preserves the critical functions of a clinically prescribed AFO

(i.e., controlling PF after initial contact and achieving toe clearance during swing), with comparable mechanical properties to several of the conventional AFOs characterized by Yamamoto *et al* [99]. Moreover, the benefit of bidirectional orthotic resistance is still debated; some suggest that resistance to PF alone (thus, unimpeded DF) is sufficient or even preferable for improving gait by enabling smooth ankle joint motion during stance phase [100].

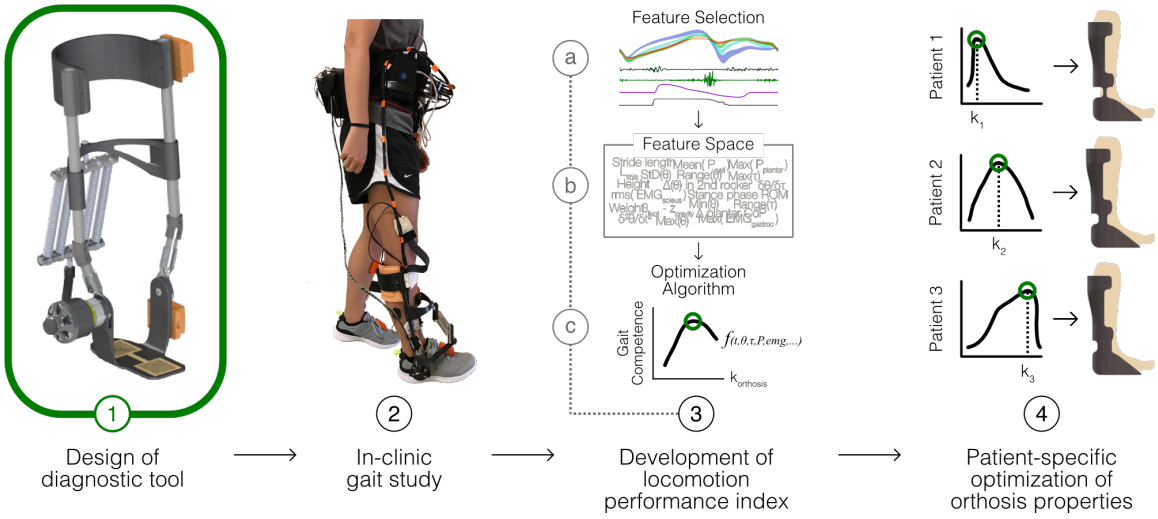

Figure 6. Broad vision and purpose of the iAFO. In this paper, we focus on the design and fabrication step of device development (Phase 1 above). The iAFO is designed to be used as a clinical tool for studying the biomechanics and gait parameters of a pathological gait patient in response to user-defined manipulation of orthotic resistance (Phase 2). Informed by the results of such gait studies, we then intend to develop an index of walking performance and an algorithm for estimating the optimal mechanical properties of an orthosis on a patient-specific basis (Phase 3), which will prime the modeling and fabrication of AFOs customized to each user (Phase 4).

The iAFO's sensing capabilities allow for monitoring of a patient's sagittal-plane ankle kinematics, kinetics (i.e., applied torque), muscle activity, plantar pressures, and orthotic interface pressures between the device and the user (Figure 7). While previous studies using passive AFOs with adjustable stiffness elements have investigated the effect of joint impedance and/or orthosis properties on user joint kinematics [40], [41], [101]–

[105], to the best of our knowledge, no prior investigation nor device has employed as comprehensive a sensor suite—in particular, systems to measure orthotic torque and interface pressures *directly*—to study how gait mechanics change in response to altered joint stiffness. The fact that the iAFO is a wearable and portable system (with the exception of the desktop computer used to store and display data, to which the device is cabled) gives it the distinct advantage of being usable in tasks other than normal level walking—to which many gait studies are limited—such as sloped walking, stair walking, and uneven terrain / obstacle evasion tasks (though perhaps difficult, given the device's lack of inversion / eversion rotation), with the potential to be used outside the confines of a gait analysis lab. Wielding this information, a clinician will be able to make informed decisions about how best to modify device geometry, "dose" orthotic stiffness, and even "titrate" this treatment parameter over the course of rehabilitation to optimize locomotor performance, accelerate recovery, minimize atrophy, and improve patient outcomes overall.

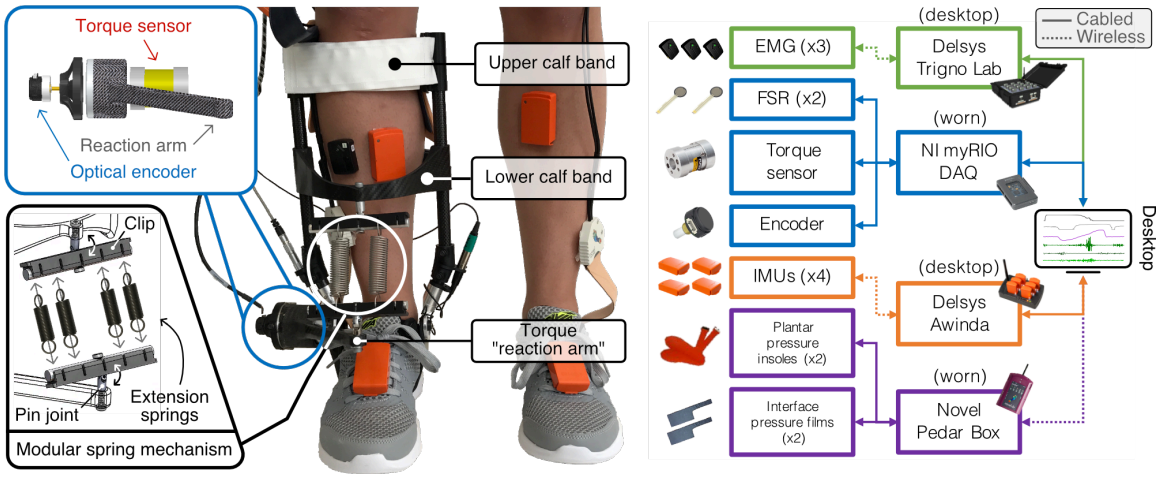

Figure 7. System-level hardware block diagram. The photo on the left shows a fully instrumented subject, equipped with the *i*AFO with its embedded sensors (torque sensor, optical encoder, and force-sensing resistors) and other standalone sensing systems (EMG, IMU, and pressure-sensitive capacitive films). Sensors that are not visible are the two FSRs and plantar pressure measurement insoles located in the sole

of the shoe, as well as the interface pressure sensors located both anteriorly and posteriorly within the calf band. The output of each sensing system is acquired by its corresponding data acquisition unit, synced in time using the myRIO as the master triggering device, and ultimately sent to a desktop computer.

3.1.2 Scientific Motivation: Studying the Effects of Elastic Ankle Loading

In addition to pursuing the clinical application outlined above, we also considered the iAFO a powerful scientific tool with the potential to shed light on some more basic questions about humans' neuromotor response to and interaction with exoskeletal devices.

Humans have a remarkable capacity for motor adaptation [106]–[109]. Understanding how we deal with perturbations to normal joint mechanics imposed by exoskeletons is an important step toward optimizing these devices for augmentative, corrective, or rehabilitative purposes. Specifically, human locomotion offers a powerful and practical space in which to study these effects, because the joint motions are often cyclical, coordinated, and well defined, and because locomotor impairments are so common [20].

As mentioned previously, the ankle joint is critical for mobility, as ~50% of the positive power generated during walking is produced at the ankle [19]. It also plays an important role in absorbing energy during the step-to-step transition and in negotiating uneven terrain [110]. Acute injuries and chronic conditions affecting the ankle are prevalent [22], and the downstream effects of impaired ankle function are drastic and detrimental. Individuals who suffer from gait deficits such as foot-drop use considerably more metabolic energy during locomotion than healthy individuals [111], and it has long been observed that corrective devices such as AFOs can greatly improve walking mechanics for these individuals [35], [112]. Though the effect of AFO stiffness on impaired

walking mechanics has been studied in some detail [41], [83], [113], the full relationship between exoskeletal ankle stiffness and joint mechanics—that of both healthy and affected populations—is still unresolved.

Exoskeletal ankle stiffness has been found to be an important factor affecting energetic cost of walking [82], [114]. In healthy individuals, a passive-elastic device even reduced the energetic cost of walking beyond that of natural gait when an optimized elastic ankle load is applied [115], [116]. This finding—that a parallel, engineered system can improve upon evolution-driven biological efficiency—ran counter to longstanding intuition about how humans adapt their walking mechanics in response to perturbation. By better understanding the relationship between the mechanical properties of an ankle exoskeleton and the behavior of the ankle joint during gait, we will be better equipped to design an exoskeleton around an individual's needs.

To explore this concept, we leveraged the iAFO's sensory and customizable stiffness features to simultaneously perturb and measure ankle joint mechanics locally. In Section 3.3, we present the results of experiments using the iAFO to investigate how ankle exoskeletal stiffness affects the mechanics of a healthy ankle joint during locomotion (Figure 8). Using an array of sensors on the iAFO, we extract kinematic and kinetic features of gait at a variety of loading conditions and demonstrate how a given exoskeletal load at the ankle maps to a change in ankle joint behavior. Additionally, we use ML techniques to develop a model for estimating exoskeletal loading conditions from only a subset of these features. Finally, we present a feature importance ranking to demonstrate the individual contribution of the gait parametric features to our model. This data-driven, model-based estimation approach can be leveraged in future work to inform the design of instrumented

exoskeletons whose mechanical properties can be tuned in a personalized and dynamic manner.

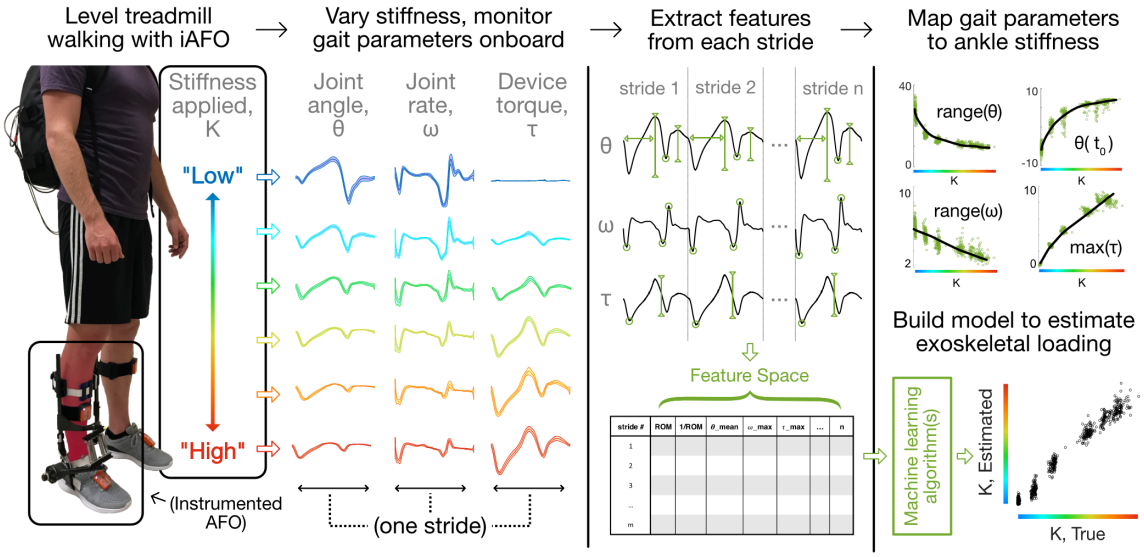

Figure 8. Overview of iAFO ML-based stiffness estimation experiment methodology and goals. An able-bodied subject walks on a level treadmill while wearing the iAFO on the right leg. Graded levels of torsional stiffness are applied to the ankle joint through the iAFO, which also enables monitoring of various parameters of ankle joint behavior during gait. These continuous walking data are spliced into individual strides, from which a set of features is extracted. These features are then plotted against the stiffness condition to reveal the effect that artificially applied stiffness has on healthy ankle joint mechanics. Finally, through machine learning techniques, a limited subset of this feature space can be used to construct a regression model for estimating ankle exoskeletal stiffness.

3.2 iAFO: System Design and Initial Validation

3.2.1 Custom Chassis Design

The frame of the iAFO is comprised entirely of custom-built hardware designed in SolidWorks (Dassault Systèmes, Waltham, MA), with the exception of the tubular uprights, which were purchased from McMaster-Carr Supply (Atlanta, GA). The AFO stirrup and both calf bands—one serving as the upper attachment point for the spring

mechanism, the other serving to secure the user's lower leg to the device—are made of a custom carbon composite. Both calf bands are height-adjustable, allowing the researcher to (1) modify the device fit based on each user's anatomy, (2) adjust the moment arm of force application to the user's shin / calf in proportion to his/her leg length, (3) accommodate extension springs of different free (i.e., unstretched) lengths, and (4) tune the angle-torque curve to a desired setting. The torque "reaction arm," formed of the same carbon composite, is fixed to the outer face of the torque sensor and extends medially and anteriorly to the sagittal plane of the user's lower leg. This component allows the torque sensor to directly measure the torque applied by the springs at the ankle joint. The torque reaction arm can be unscrewed and rotated 180°, allowing the springs to be installed either anterior to the shank (thereby resisting PF) or posterior (thus resisting DF). The angled joints which insert into either side of the stirrup are milled out of aluminum 6061-T6, while the custom elbow joints directly superior to them are made of acrylonitrile butadiene styrene (ABS) plastic using a Lulzbot Taz 5 3-D printer (Aleph Objects, Loveland, CO). The device frame alone weighs just 0.6 kg; with sensors embedded, the iAFO weighs 0.9 kg; all device peripherals (e.g., data acquisition, interface circuitry, cables), which can be worn in a backpack or (as shown here) in a belt, weigh 2.3 kg.

3.2.2 Modular Stiffness Mechanism

The key feature of the iAFO is the capacity for user-defined modulation of its torsional stiffness, which is accomplished via interchangeable extension springs. These springs are mounted either anterior or posterior to the shank of the user, enabling one to study the effect of resistance to ankle PF or DF independently (mostly). Springs of various spring rates are mounted in parallel, with each end spaced evenly along an aluminum rod

and anchored with a custom clip made out of ABS plastic. The mechanism supports up to five springs installed in parallel, enabling the researcher to study the effects of a wide stiffness gamut. Both ends of the spring attachment mechanism are fixed to the frame of the iAFO. When the angle between the device uprights and footplate changes, so too does the distance between spring mounting points, thus deflecting the spring(s). The force developed in the spring(s) causes a resistive torque at the device's joint axis, causing the user to experience a torsional stiffness at the ankle in the direction of either ankle PF or DF. Therefore, in effect, the iAFO acts simply as a torsional spring in parallel with the anatomical ankle joint. When the springs are installed anterior to the limb, they impede PF, which we refer to as plantarflexion resistance (PFR) (Figure 9, left pane). Likewise, when the springs are mounted posterior to the limb, they perform dorsiflexion resistance (DFR) (Figure 9, right pane). It should be noted that, due to the design of this elastic mechanism, when the iAFO is in its PFR mode, the springs not only fight PF but also *assist* DF in certain phases of the gait cycle. The converse is true when the device is operating in its DFR mode, both impeding DF and assisting PF. This is an important point to consider from a device- and gait-mechanics perspective. At this time, our device is unable to resist both DF and PF simultaneously, so we perform testing under DFR and PFR independently.

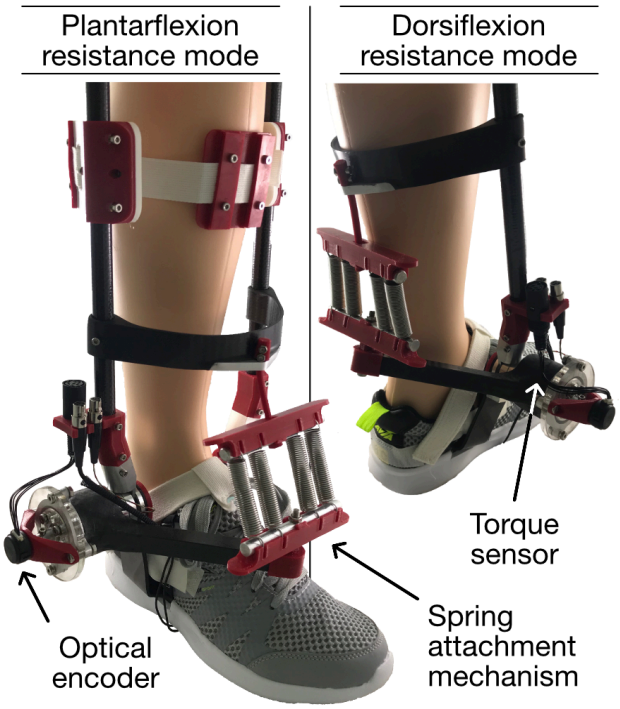

Figure 9. iAFO, shown in both the dorsiflexion and plantarflexion resistance modes. The key components (optical encoder to measure joint angle, reaction torque sensor to measure device resistive torque, and spring attachment mechanism for applying graded levels of torsional stiffness) are labeled.

3.2.3 Sensing and Data Acquisition

To maximize the utility of the *i*AFO as a clinical tool, we equipped it with an extensive sensor suite designed to capture a wide range of clinically relevant biomechanical measures, which are listed in Table 3 and illustrated in Figure 7. Signals from the optical encoder, reaction torque sensor, and force-sensitive resistors (FSRs) were acquired directly by a myRIO real-time field programmable gate array (FPGA)-based data acquisition device (National Instruments, Austin, TX), while the remaining sensing systems—IMU, plantar/interface pressure sensors, and EMG—required their own proprietary data collection hardware and software. The optical encoder was found to be the optimal angle sensing modality for our application, based on its high resolution, repeatability, and

reliability in simulated joint kinematic tests [47]. As they were installed in parallel and not physically integrated into the device, the IMU and EMG systems were considered auxiliary/supportive. As depicted in Figure 2, in addition to the sensors worn on the ipsilateral limb (the limb with the iAFO), two IMUs and one plantar pressure insole were worn on the contralateral limb to investigate potential effects on gait symmetry. (It should be noted that no data collected from the contralateral limb are reported in this work, as these effects are still being explored. Similarly, IMU data are not reported, as they were considered redundant to kinematic data obtained by the encoder.) Signals from the encoder, torque sensor, and FSRs were recorded by the NI myRIO at a sampling rate of 1 kHz, while plantar- and interface pressures were sampled at 50 Hz, IMU data at 75 Hz, and EMG data at 1926 Hz. All acquired signals were synchronized to facilitate concurrent analysis. The myRIO served as a master triggering device, initiating and terminating acquisition of signals on each sensor system simultaneously. Signals from each sensor subsystem were monitored in real-time on a desktop computer. A custom graphical user interface (GUI) was created in LabView (National Instruments, Austin, TX) to analyze, process, and display signals acquired by the myRIO and to allow for streamlined user control of data collection timing and file management. Custom analog interface circuitry was designed to filter and amplify the output of the strain gage-based reaction torque sensor (low-pass filter with cutoff frequency = 50 Hz, gain = 60.1 dB). In theory, orthotic torque can be calculated given knowledge of the spring mechanics and certain geometrical considerations (see Section 3.2.6), but given uncertainties in real-world implementation (e.g., friction, nonlinear spring force, fatigue), we considered direct measurement of torque necessary to obtain the most accurate information possible. All circuitry and peripheral devices (e.g.,

myRIO, synchronization boxes, pressure sensor DAQ, battery power) are worn either at the waist or housed in a backpack.

Table 3. Parameters of gait measured and sensors used.

Parameter	Sensor Type	Manufacturer	Sensor Name	Mfg. Location
Ankle rotation (sagittal plane)	Optical encoder (incremental)	US Digital	S4T	Vancouver, WA, USA
Spatial limb orientation	Inertial measurement unit (IMU)	Xsens	MTw Series	Enschede, Netherlands
Orthosis torque	Reaction torque, strain gage-based	Futek	TFF350	Irvine, CA, USA
Gait states	Force-sensitive resistor (FSR)	Interlink Electronics	Model 402	Westlake Village, CA, USA
Plantar pressures	Pressure-sensitive capacitive film	Novel	Pedar	Munich, Germany
Interface pressures	Pressure-sensitive capacitive film	Novel	Pliance	Munich, Germany
Muscle activity	Electromyography (EMG)	Delsys	Trigno Lab	Natick, MA, USA

3.2.4 System Specifications

A summary of the key features of the iAFO system can be found in Table 4, including metrics of device wearability and functionality as well as a few important sensor specifications. Certain parameters such as orthotic torque capacity and range of linear torque application are setup-dependent (i.e., the former depends on the available range of spring stiffness values, while the latter depends on the calf band height setting, as discussed previously). In all, these attributes suggest a highly modular, versatile, and effective tool for selectively modifying orthotic stiffness and for thorough monitoring of an expansive set of gait parameters.

Table 4. iAFO system specifications.

Parameter	Value
Size and Wearability	
Weight	0.9 kg (fully instrumented)
Overall dimensions	40 x 23.5 x 21 cm
Calf-band height adjustability range	10 to 32.5 cm proximal ankle
Shoe size accommodation	US size 7-13
Sensor Specifications	
Torque measurement range	± 56.5 N-m (500 in-lb)
Angle measurement resolution	0.25°
Sampling Rates	1 kHz (joint angle, torque, FSRs), 50 Hz (interface / plantar pressures), 1926 Hz (EMG), 75 Hz (IMU)
Functionality	
Parameters monitored	Ankle joint angle, orthotic torque, plantar/interface pressures, EMG, lower limb orientation, gait states
Orthotic resistance modes	PFR, DFR (independently)
Orthotic ankle torque capacity[a]	± 15 N-m
Range of linear torque application[b]	-15° to 10°
Angle measurement plane	Leg sagittal

[a]Dependent on springs applied; rated here for stiffest available springs at peak DF/PF angle achieved; likely higher for greater spring rates
[b]Dependent on L_0, preload, and attachment height setting of spring(s) (see appendix section)

3.2.5 Benchtop Testing

3.2.5.1 Benchtop Experimental Setup

To characterize the performance of the iAFO and demonstrate how it resists ankle rotation, we performed benchtop tests and compared the results to those of an actual gait study. In particular, we were interested in the device's angle-torque relationship in the sagittal plane of the foot / ankle. In the benchtop experiments, the device's footplate was clamped to a tabletop and its upper frame was rotated back and forth by hand approximately 15° in both plantarflexion and dorsiflexion. (NB: This work adheres to classical ankle

measurement conventions—i.e., "0°," or neutral, is defined as when the shank is perpendicular to the foot, plantarflexion is defined as the range of negative angles, and dorsiflexion is defined as the range of positive angles.) Two different stiffness conditions—defined simply as the sum of spring rates, as springs were applied in parallel—were applied: 350 and 1540 N/m, as these two values represented the lower and upper ends of orthotic restraint investigated in human subject trials. The device angle and torque were recorded by the optical encoder and reaction torque sensors respectively, and the data were acquired by the NI myRIO data acquisition device. The torque versus angle relationship obtained from the benchtop tests was then compared to that of the human subject experiment (detailed further below). Additionally, we developed a mathematical model (see Section 3.2.6) to describe how the device's geometric parameters inform the shape of the angle-torque curve in the angle range of interest and thus how, for a given stiffness condition, this relationship can be "tuned" by a simple adjustment of the calf-band height setting.

3.2.5.2 Torque vs. Angle Relationship: Device Only

The results of benchtop testing (Figure 10) demonstrate that, in either PFR or DFR mode, the iAFO appears to apply torque linearly across the ankle angle range, comparable to the linear-elastic region of a material's torsional stress-strain curve. The curves of each stiffness condition (i.e., each pair of same-color curves) appear to have similar slopes in both resistance modes (for the "350 N/m" setting: 0.056 Nm/° in DFR and 0.058 Nm/° in PFR, 4.4% difference; for the "1540 N/m" setting: 0.27 Nm/° in DFR and 0.30 Nm/° in PFR, 9.7% difference), suggesting the *i*AFO operates similarly in DFR and PFR.

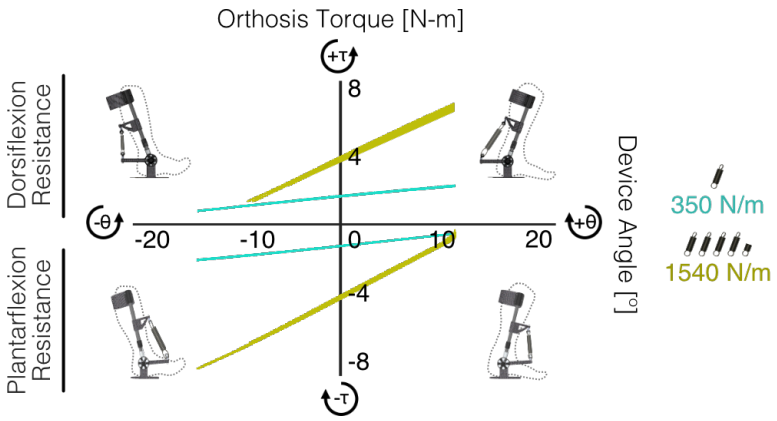

Figure 10. Benchtop testing results: orthotic torque vs. angle relationship in both resistance modes for two stiffness conditions. The two curves above the x-axis were generated with the device in its dorsiflexion resistance mode (i.e., extension springs mounted posterior to the calf), while the curves below the y-axis correspond to the device in its plantarflexion resistance mode. In the angle regime of interest (-15° to 15°), the device applies torque in a linear fashion and does so nearly equivalently in both resistance modes.

3.2.6 Mechanical Model / Simulation

To better our understanding of the mechanical behavior of the iAFO, we endeavored to supplement the insights gained from benchtop testing with the development of a simplified geometric model whereby, given some input parameters (e.g., calf band height, applied stiffness condition), we could predict the angle-torque curve that the device would exhibit within the range of motion of the user's ankle joint. In doing so, we hoped to mitigate issues of end-range torque nonlinearity and incomplete separation of torque application into either rotation direction (DF or PF) by selecting an appropriate calf band height setting. The "calf band" referenced here is the lower one on which the spring attachment mechanism is mounted, *not* the one that bears user force input; therefore, we are effectively describing changes in the mounting position of the spring. Figure 11

illustrates the geometric parameters used in Equations 1, 2, and that are used to construct the mathematical model of the torque versus angle relationship.

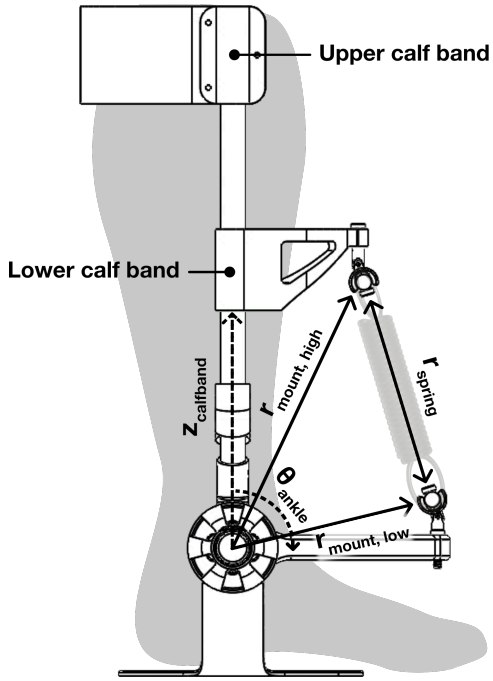

Figure 11. Geometric model of the iAFO, lateral view. As shown, the device is in its plantarflexion resistance mode. Each of the vectors defined here is used to predict the geometric relationship between ankle joint excursion and spring deflection and thus the amount of torque applied by the device, a relationship which defines the degree of orthotic constraint.

$$\vec{r}_{mount,high} = f\left(\theta_{ankle}, z_{calfband}\right) \tag{1}$$

$$\vec{r}_{spring} = \vec{r}_{mount,\,low} - \vec{r}_{mount,high} \tag{2}$$

$$\tau = \vec{r}_{mount,\,low} \times \left\{ k_{spring} \left[\vec{r}_{spring} - \frac{\vec{r}_{spring}}{\left\| \vec{r}_{spring} \right\|} L_0 \right] \right\} \tag{3}$$

Equation 1 suggests that $\vec{r}_{mount,high}$, the vector from the center of rotation at the ankle joint to the upper attachment point of the spring(s), is simply a (trigonometric) function of

$z_{calfband}$, which is the adjustable calf band height setting, and θ_{ankle}, which is the rotation of the user's ankle joint, measured clockwise from the positive vertical axis. Equation 2 defines $\vec{r}_{spring}$ as the vector difference between $\vec{r}_{mount,high}$ and $\vec{r}_{mount,low}$, which is the vector from the center of the ankle joint to the lower attachment point of the spring mechanism. The final calculation relating torque and ankle angle is shown in Equation , where τ is the calculated orthotic torque applied to the user, k_{spring} is the stiffness condition, and L_0 is the free length of the spring(s) used. The term within the curly braces represents the force developed in the extension spring(s) due to lengthening, calculated using Hooke's Law. Since the springs are non-ideal and are manufactured with a preload, k_{spring} was determined experimentally on a benchtop setup for a range of spring deflections in order to improve the accuracy of the model.

Figure 12 shows the result of these calculations for a range of calf band height settings (from 100 to 200 mm, referenced from the ankle joint center) and across a range of ankle angles, with the device in its PFR mode and for the 350 N/m stiffness condition. The model is moderately accurate in predicting true device behavior in the range of PFR torque (i.e., the negative y-axis, in which the springs are extended). The model predictions in the positive torque regime are excluded from the figure, as they are not a faithful representation of the device's behavior in end-range dorsiflexion. The model is useful primarily as a means to understand (in general) how the torque-angle relationship can be modulated, particularly around $\theta_{ankle} = 0°$, by changing the height setting of the spring attachment, which can be gleaned from the plot.

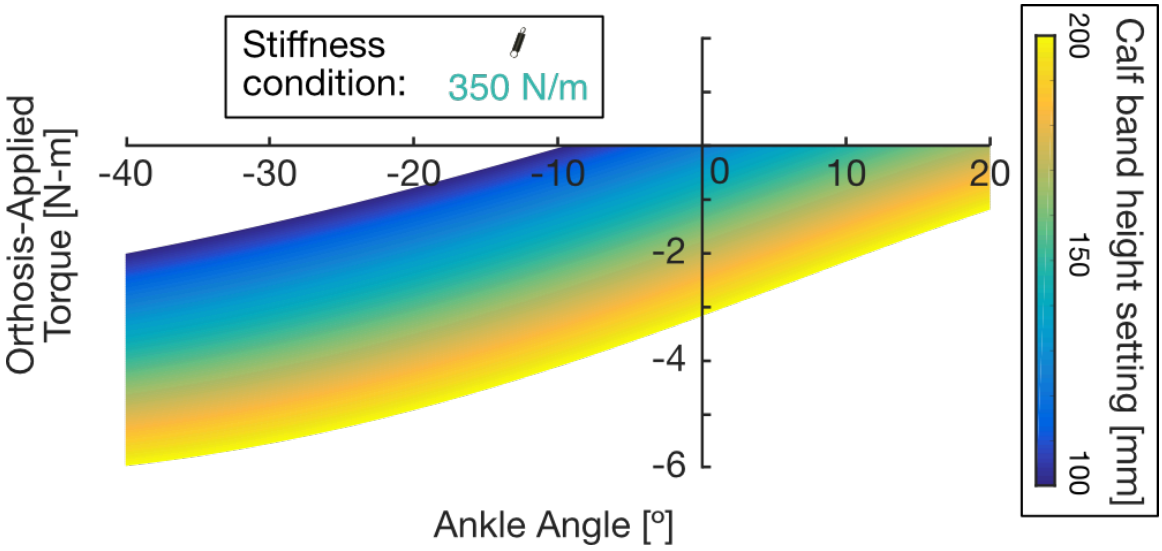

Figure 12. Example of model torque vs. angle output for a range of calf band height settings (resistance mode: PFR, stiffness condition: 350 N/m). Each isochromatic curve corresponds to a specific height setting. For our tests, we chose a height setting of 160 mm, which gave us a good balance for isolating resistance into PF and mitigating nonlinearity at high angles of dorsiflexion. Only torques in the PFR regime are shown.

3.2.7 Proof-of-Concept Human Subject Testing

3.2.7.1 Human Subject Experimental Protocol

To demonstrate the iAFO's potential for use in clinical gait study applications, we fit the device to the right leg of a healthy male subject (age: 23, weight: 68 kg) and performed normal, level walking trials at a variety of orthotic stiffness settings. Locomotion took place on a treadmill at a constant speed of 1.0 m/s. Five stiffness conditions were investigated, including 0 (i.e., unloaded/no springs), 350, 700, 1540, and 1890 N/m. For this range of stiffness values, a maximum of 7 N-m of dorsiflexion-assist torque was reached at 10° of plantarflexion, consistent with the lower end of the range that Yamamoto *et al* suggested is necessary for individuals with pathological gait [101] and consistent with the torques that they found most solid-ankle, plastic AFOs produced [99].

We believe this to be a sensible range for healthy subjects, though the modularity of our stiffness control mechanism allows us to adjust the maximum stiffness, should it be required for users with hemiplegic gait. Data were recorded for 100 seconds per trial. The subject was allowed to walk in the device for an extended period of time (~ 5-10 minutes) before collecting data to minimize the possible confounding effect of motor adaptation on experimental results. Orthotic stiffness challenges were administered randomly, and each condition was repeated three times over the course of data collection to establish the consistency of results. PFR and DFR modes were evaluated independently, though only the results of PFR experiments are presented below, as we believe they more validly represent the effect (and purpose) of an AFO designed for an individual with foot drop, for whom assistance in dorsiflexion (i.e., plantarflexion resistance) is critical.

3.2.7.2 Torque vs. Angle Relationship: Device + Limb

The torque-angle curves obtained during a human subject experiment (Figure 13) were consistently quite linear. The curves shown in Figure 13 resulted from an experiment performed solely in the device's PFR mode, and they represent the relationship between the device's angle and torque curves, averaged over the course of a full data collection trial (~ 50 gait cycles). The torque vs. angle curves for the 350 and 1540 N/m stiffness conditions have slopes nearly equivalent to those obtained in benchtop experiments (for the "350 N/m" setting: 0.72% difference; for the "1540 N/m" setting: 2.9% difference). A small amount of hysteresis—suggesting the orthosis applied torque differently in loading versus unloading at moderately high-frequency cycling—is present in the extreme angles of the three highest stiffness conditions, perhaps due to internal friction of the springs or the viscoelastic influence of the leg's soft tissues.

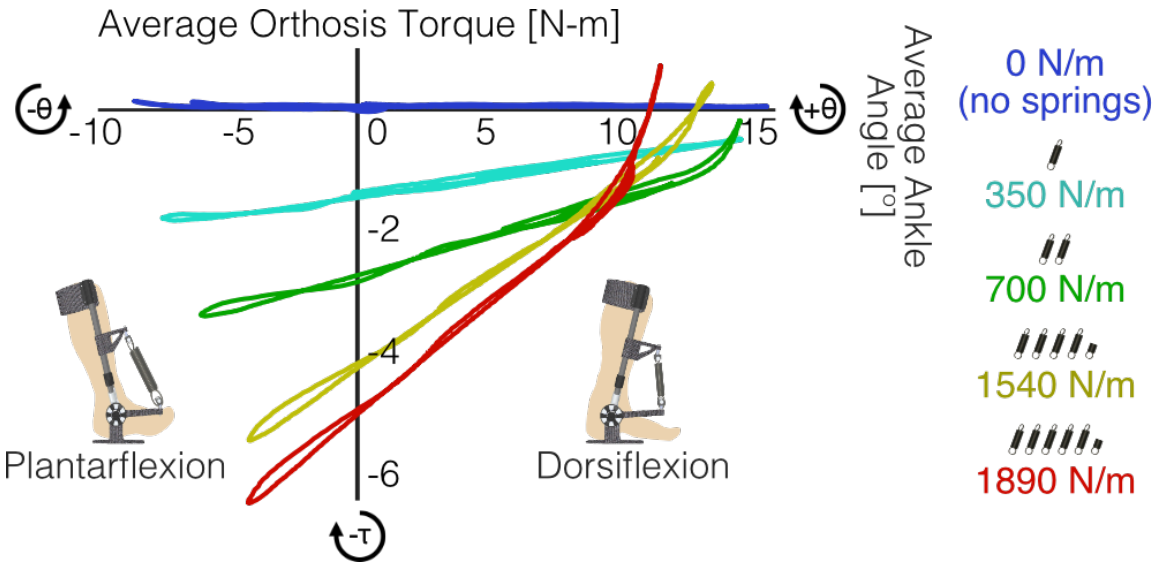

Figure 13. Orthotic torque vs. ankle angle relationship in plantarflexion resistance gait study. Five stiffness conditions were considered, and torque was applied to the user linearly, just as in the benchtop experiments. Some amount of nonlinearity and hysteresis was observed, though these were relatively negligible across most of the ankle range of motion. The curves above represent the ensemble average of individual torque vs. angle curves across approximately 50 steps.

One noteworthy feature of the data from the human subject gait study is the apparent nonlinearity of the angle-torque curve at the end range of dorsiflexion. This aberration occurs when the extension springs, in their fully compressed state, press into the torque reaction arm when the angle between the tibia and the foot is sufficiently acute. This action causes the torque sensor to register values in the opposite direction of desired torque application. This behavior speaks to an inherent limitation in the device's ability to apply end-range orthotic resistance. To minimize this nonlinearity in the PFR mode, we ensured that the springs remained minimally extended at the highest expected angle of dorsiflexion (~ 20°) by adjusting the height setting of the spring attachment mechanism. The tradeoff in doing so is the imperfect separation of orthotic resistance into either DFR or PFR and, effectively, an adjustment of the neutral angle of the device (i.e., the angle at which the

device applies zero torque). We used our geometric model of the iAFO (see Section 3.2.6) as a guide to balance the tradeoff between full directional separation of orthotic resistance and end-range torque-angle curve linearity. Indeed, this ability to select the neutral angle of the device may in some cases be considered a design advantage, as it has been shown that an AFO's neutral (or "initial") angle can greatly impact a user's gait kinematics and mobility [41], [117].

3.2.7.3 Proof-of-Concept Gait Parameters

Figure 14 illustrates several signals of interest that the iAFO is able to record on a continuous, step-to-step basis. All waveforms depict signal behavior across the gait cycle, beginning with initial contact ("heel-strike") and ending with terminal swing. The top six waveforms (FSR, pressure measurement insole, and EMG) are simply representative samples of data isolated for a single step under a single stiffness condition and are left unitless, as (in this discussion) their shapes are more meaningful than their numeric values, and they serve mainly as a demonstration of the sensing capabilities of the system. IMU data are not reported here, as they were considered redundant to the kinematic data obtained by the optical encoder; however, the use of IMUs for discerning deviations between device angle and the user's anatomical joint angle is yet to be explored. Furthermore, only data from the sensors embedded in the device (encoder, torque sensor) are reported across all stiffness conditions.

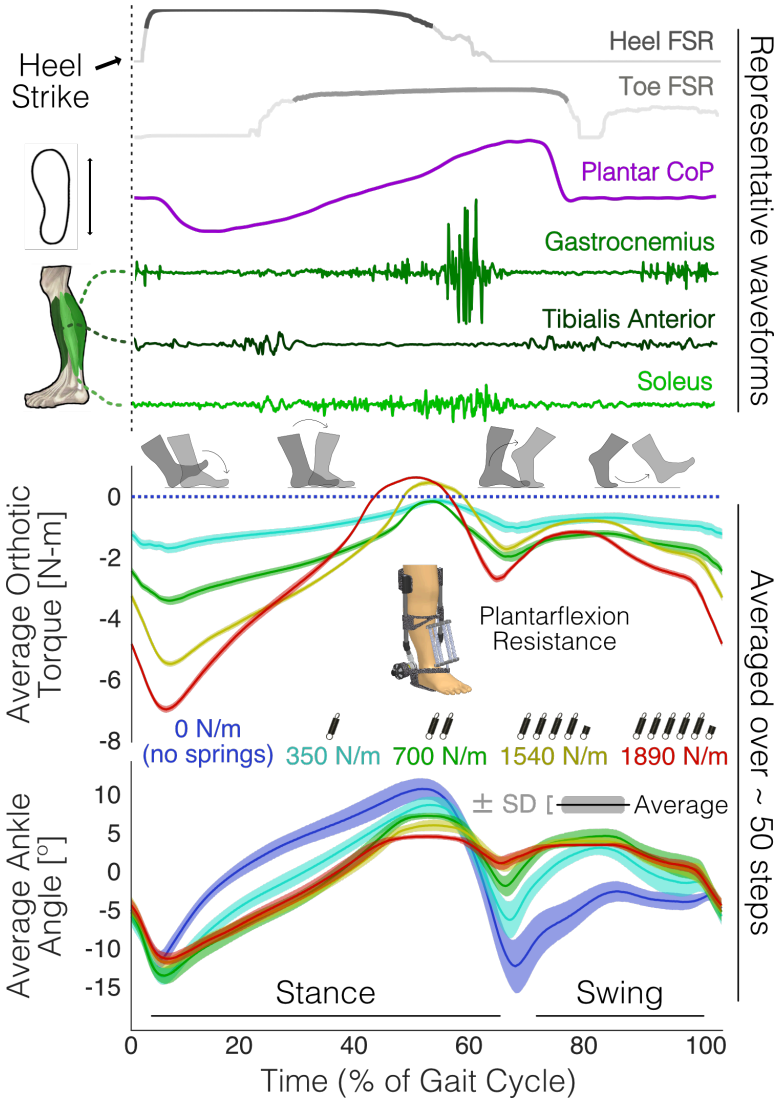

Figure 14. Results of plantarflexion resistance experiment (n=1). All waveforms are synchronized in time across a single gait cycle. The top six waveforms are simply representative of sensor outputs for a single step, and the bottom two plots are comprised (respectively) of orthotic torque and ankle angle waveforms averaged across approximately 50 steps, plotted against the percentage of one gait cycle. A key finding of this experiment, illustrated in the bottom plot, is a marked attenuation of ankle excursion in both the terminal stance and swing phases of gait with increasing orthotic resistance.

3.2.7.3.1 Plantar Pressures

The "Heel FSR" and "Toe FSR" signals (first two waveforms in Figure 14) are used simply to delineate states of gait and to serve as a timing reference for windowing the continuous data into individual steps for subsequent averaging and analysis. The "Plantar Center of Pressure" waveform (third waveform in Figure 14) was obtained from the Novel Pedar plantar pressure measurement system. The curve corresponds to the location of the plantar center of pressure (CoP) along the lengthwise axis of the subject's right foot over the course of a gait cycle: beginning at a neutral location at the very beginning of stance phase, moving closer towards the heel during the loading response phase, and traveling distally along the foot towards the metatarsals at push-off, before finally returning to a neutral position during swing phase. A comparison of the average CoP waveforms across stiffness conditions (shown in Figure 15) reveals a trend towards decreasing peak distance of CoP along the length of the foot with increasing orthotic resistance. This finding suggests that, with a stiffer dorsiflexion-assistive AFO, a person may not be able to apply plantar forces as far forward during late-stance and thus reduce his/her capacity to push off effectively, perhaps reducing stride length and gait efficiency.

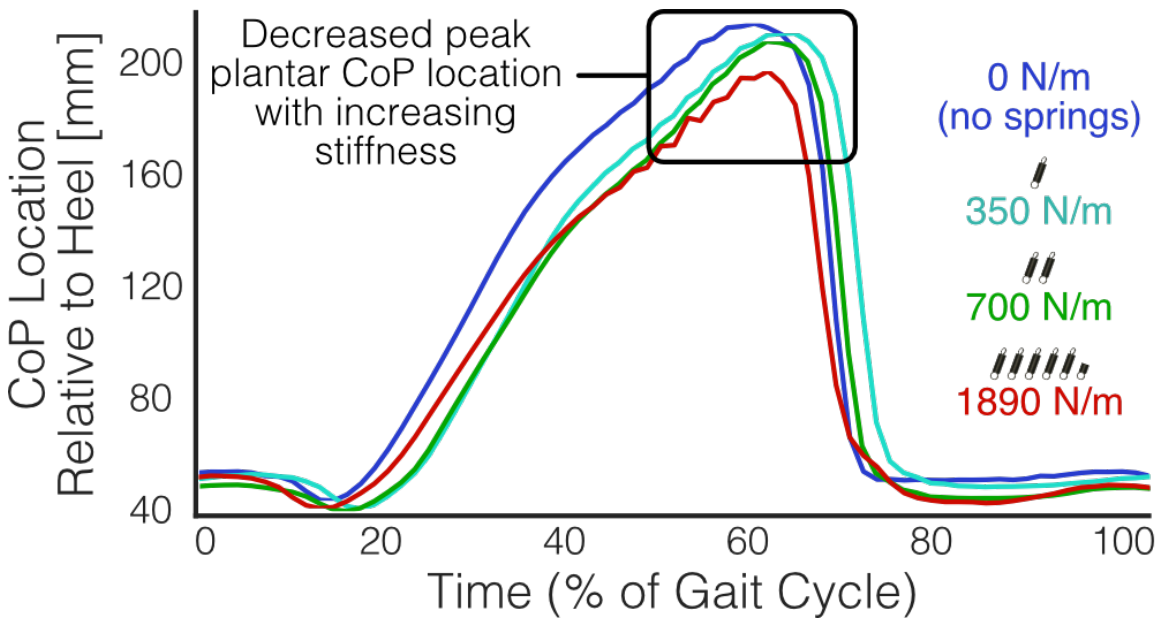

Figure 15. Average plantar center-of-pressure location changes with increasing orthotic resistance. Here CoP location is defined as the lengthwise distance along the right foot beginning at the back of the heel, measured in millimeters. Peak CoP location decreased progressively from 216 to 213.5 to 210.1 and finally to 202.3 mm for each increasing stiffness challenge, suggesting a diminished ability to transfer plantar forces towards the forefoot, likely resulting in a decrease in the anatomical torque produced by the individual at the ankle joint.

3.2.7.3.2 Muscle Activity

The three EMG waveforms shown in green in Figure 14 illustrate respectively the activity of the medial gastrocnemius, TA, and soleus muscles during a single gait cycle, and the recorded waveforms align logically with each one's anatomical function–that is, the plantarflexors (gastrocnemius and soleus) demonstrate increased activity during stance phase and push-off, while the TA (an ankle dorsiflexor) is more active during loading response and swing phase [20]. While not especially revelatory in this preliminary healthy subject experiment, we anticipate EMG data will be particularly useful in discerning the *timing* of muscle activation during each phase of gait and determining whether, or how, this timing is disrupted in hemiplegic gait patients as a result of the modulation of orthotic

constraint. But for the purposes of this work, the waveforms simply demonstrate our system's ability to monitor muscle activity concurrently with various other gait parameters of clinical interest.

3.2.7.3.3 Device Angle and Torque across Five Stiffness Conditions

The bottom two plots of Figure 14 represent the key findings of our preliminary pilot study. Each plot is comprised of several ensemble-averaged waveforms (+/- SD) of orthotic torque (top) and ankle joint angle (bottom) for each of the stiffness conditions listed previously. The average orthotic torque plot, illustrating the change in torque applied by the iAFO to the user, shows a distinct and proportional change in the amount of rotational resistance for each successive applied stiffness. The errant behavior of the highest two stiffness conditions at around 40-50% of the gait cycle where the torques appear to change sign (i.e., from counter-clockwise to clockwise, or PFR to DFR) is a product of the same phenomenon explained above (i.e., the unstretched springs bearing down upon the torque reaction arm during pronounced DF). Nonetheless, the graph clearly demonstrates an increase in torque magnitude with increasing stiffness (as expected) and illustrates the high repeatability of the signal, as evidenced by the low standard deviation error bars on each average waveform. The bottom plot illustrates the marked changes in ankle range of motion resulting from modulation of orthotic stiffness. The most obvious stratifications occur towards the end of stance and beginning of swing, where an embiggened resistance to PF results in a substantial reduction in ankle joint excursion during the second rocker (i.e., when the tibia processes over the ankle)—seen here as a reduction in the peak DF angle at the end of stance phase—as well as a significant attenuation of ankle excursion during "push-off," in which the foot rapidly plantarflexes to

propel the person forward. A significant decrease in full ankle range of motion (i.e., the peak-to-peak amplitude of each average angle waveform) is also apparent with increasing stiffness challenge.

One possible explanation for the reduction in stance-phase dorsiflexion is that the subject is attempting to maintain a symmetrical gait: the springs resist ankle plantarflexion during the loading response phase, thus prolonging that motion; in order to compensate, the subject may then abbreviate the following phase(s), shortening the step and thus not advancing the limb as far forward. Or perhaps it is a product of the subject simply fighting against any perceived perturbation, either resistive or assistive—though a more detailed biomechanical analysis is needed to make a definitive claim.

3.2.8 Discussion

3.2.8.1 Clinical Relevance and Potential Applications

As mentioned previously, the traditional methods for evaluating AFO-assisted gait are often subjective and imprecise. If deployed in a clinical setting, the iAFO could provide practitioners with a wealth of potentially useful information for prescribing an orthosis with optimal stiffness. With the sensors proposed, the system could report—in real-time and with high resolution and temporal detail—gait parameters such as (1) ankle joint range of motion (both overall and in each discrete phase of gait); (2) peak torque applied by the device; (3) biomechanical "power" lost to the device across a gait cycle; (4) time spent in single-limb support on the affected limb; (5) changes to gait symmetry; (6) peak impulse (force-time integral) applied at device-to-user interface (perhaps a measure of discomfort or how much energy is lost to the device); (7) training/motor-learning effects over time;

(8) ankle angle and amount of "shock" (peak acceleration) at initial contact (indicating how effectively momentum is preserved step-to-step). Information of this nature would be impossible to attain through observational gait analysis alone, and much of it would be unattainable even given state-of-the-art motion capture setups.

Coupling these sensory capabilities with the iAFO's modular stiffness feature will allow researchers to understand the implications of orthotic stiffness on a deeper level than previously possible. For instance, studies employing the iAFO may reveal—in great detail and on a case-by-case basis—correlations between AFO stiffness and stance-phase stability, mitigation of toe drag, reduction in steppage gait, improvement in stride length symmetry, etc. With this greater depth of understanding, a clinician could, for example, target a higher dorsiflexion stiffness to prioritize stance stability for an elderly patient whose critical need is the prevention of falls. Likewise, a patient with severe plantarflexion contracture could be prescribed an AFO tuned to a higher plantarflexion stiffness to correct for this malady.

Data collected from iAFO-enhanced gait studies would supplement more traditional clinical criteria such as gait velocity and patients' subjective assessment of comfort to form a comprehensive, evidenced-based AFO stiffness prescription pathway. Furthermore, these gait studies could be performed iteratively along the course of rehabilitation, allowing for adjustments to a patient's "stiffness regimen" over time as results dictate.

3.2.8.2 Limitations

While the iAFO boasts many positive design characteristics (e.g., robust construction, high modularity, extensive sensing capabilities), it also has a few limitations. For instance, the method of applying orthotic restraint (via unilaterally applied extension springs), though simple and user-friendly, is not an ideal way to simulate the mechanical characteristics of a true, solid-ankle AFO commonly used in clinical practice. The reasons for this shortcoming have been discussed previously, but as stated before, we found that our device applied orthotic restraint in a way which corresponds favorably to the results found by Yamamoto *et al* for several commercial AFOs [99]. In the future, we plan to refine our design to incorporate spring-like elements that can provide orthotic resistance in both directions simultaneously and can be adjusted continuously, perhaps using compression springs, series-elastic actuators to serve as "tunable" springs, a disengaging clutch mechanism such as the one used by Collins *et al* [116], or a continuous "mechanical impedance adjuster" such as developed by Morita and Sugano [118]. Additionally, our device requires the use of a set of shoes modified to accommodate its dimensions, meaning it cannot simply be slipped into any patient's preferred footwear. This is done out of necessity to ensure a proper seating of the device in the shoe and to minimize the effect of variations in shoe composition, shape, and overall design on between-subject results. Finally, our device, as with the majority of articulated AFOs, limits ankle joint action to rotation in the sagittal plane, impeding compound joint motions that involve foot inversion and eversion.

3.3 Elucidating the Effects of Exoskeletal Stiffness on Healthy Ankle Joint Mechanics in Locomotion

3.3.1 Experimental Protocol

All studies in this Section (3.3) were approved by the Georgia Institute of Technology Institutional Review Board and the United States Army Medical Research and Materiel Command Office of Research Protections Human Research Protection Office.

3.3.1.1 Subject Recruitment

A total of twelve able-bodied subjects (8 male, 4 female) were recruited for this study (age range: 19-34, weight: 70.5±13 kg, height: 175±11 cm). Six subjects performed the experiment while wearing the iAFO under both PFR and DFR load, and, because a subset of subjects was unable to complete both sets of experiments, the remainder of the subjects were randomly assigned to either PFR (four subjects) or DFR (one subject) loading. Therefore, a total of 10 subjects participated in the PFR arm of the study, and 7 subjects participated in the DFR arm of the study.

3.3.1.2 Loading Conditions

Through pilot testing, we observed that, for the vast majority of subjects, changes in ankle motion began to "level off" when an external load of approximately 1.0 Nm/° was applied in either PFR or DFR. Having identified this asymptotic behavior, we selected six distinct torsional stiffness conditions in this loading range at which we conducted the walking tasks: 0 (unloaded, no springs applied), 0.15, 0.3, 0.5, 0.8, and 1.0 Nm/°.

3.3.1.3 Walking Task Protocol

Subjects were asked to walk on a level treadmill (1.0 m/s) while wearing the iAFO unilaterally on their right leg under either PFR or DFR load. Within each experiment, the six levels of loading were applied by the iAFO in random order, and the subject was asked

to walk under each discrete loading condition for 90 seconds, during which time the iAFO recorded data for ~ 60 strides. Before collecting data, the subject was given an extended period of time (up to 5 minutes) to walk in the device at the given loading condition to minimize the effects of motor adaptation during data collection. Each loading condition was repeated once to confirm a consistent result.

3.3.1.4 Exoskeleton Dynamics: Power and Work

Two important kinetic features explored in this work deal with the flow of power and work through the iAFO. To calculate device power, we simply compute the inner product of the device torque and angular rate measurements:

$$P = \tau \cdot \frac{d\theta}{dt} \tag{4}$$

where P is the calculated mechanical power absorbed by the device, τ is the device torque as measured by the integrated reaction torque sensor, θ is the device angle as measured by the optical encoder embedded in the device joint, and $\frac{d\theta}{dt}$ represents the joint velocity (the time-derivative of θ). We then define the work, which represents the elastic energy stored/released by the springs across each stride, as the cumulative time-integral of P across each gait cycle, from 0 to 100% stride:

$$U = \int_{t_0}^{t_{100}} P \, dt \tag{5}$$

where U is the amount of energy stored in the bank of extension springs, dt is the time-step between samples as defined by the sampling rate (1 kHz), t_0 is the time-stamp at the

beginning (i.e., 0%) of a given gait cycle, and t_{100} is the time-stamp at the end (i.e., 100%) of the same gait cycle.

3.3.1.5 Signal Processing and Data Analysis (Machine Learning)

3.3.1.5.1 Gait Cycle Segmentation and Ensemble-Averaging

In each walking trial, we recorded joint angle and torque continuously across ~60 strides. To understand the general behavior of the ankle joint at each loading condition, we segmented the data into individual gait cycles using initial contact (heel-strike) as the timing reference and then computed the ensemble average across the total number of discrete strides. This process yielded a mean waveform (with some standard deviation error) that described the overall joint trajectory and applied joint load across a single walking trial.

3.3.1.5.2 Stride-Specific Feature Extraction

We extracted a set of kinematic and kinetic features (Table 5) from the optical encoder and torque waveforms, respectively, of each individual stride and inserted these features into an M-by-N matrix (M = number of strides, N = number of features). For each gait cycle, we also computed the average exoskeletal stiffness (the average slope of the torque-angle curve) as the output, or label, to which our machine learning results would be compared. We repeated the above process for every walking trial across all subjects and combined all resulting feature matrices to form an aggregate training/testing set for our machine learning algorithms. From the 10-subject PFR experiment set, the total dataset comprised 44 features across 6913 strides, or instances. For the 7-subject DFR experiment set, the total dataset comprised the same 44 features across 4652 strides.

Table 5. List of gait parametric features extracted from iAFO sensor data.

Feature	Description	Units
ROM	Ankle range of motion ($\theta_{max} - \theta_{min}$) across full stride	°
ROM_{PO}	*ROM* during push-off phase	°
ROM_{Sw}	*ROM* during swing phase	°
$(ROMinv)_{xx}$	$1 \div ROM_{xx}$ | $[ROM_{xx} : f_{1\text{-}2}]$	$(°)^{-1}$
$(ROMinvSq)_{xx}$	$1 \div (ROM)^2$ | $[ROM_{xx} : f_{1\text{-}2}]$	$(°)^{-2}$
$(ROMinvSqrt)_{xx}$	$1 \div (ROM)^{1/2}$ | $[ROM_{xx} : f_{1\text{-}2}]$	$(°)^{-1}$
angleMax	Max. ankle joint angle	°
angleMin	Min. ankle joint angle	°
angleMean	Avg. ankle joint angle	°
angleIC	Ankle angle at initial contact	°
angleRMS	Root-mean-squared angle across stride	°
angleSTD	St. dev. from the mean angle across stride	°
angleCrest	Crest factor of angle (*ROM* ÷ *angleRMS*)	--
omegaDFmax	Peak DF angular rate (ω_{max})	rad/s
$omegaDFmax_{St2Sw}$	*omegaDFmax* in stance-swing transition	rad/s
$omegaDFmax_{St}$	*omegaDFmax* during stance	rad/s
omegaPFmax	Peak PF angular rate (ω_{min})	rad/s
$omegaPFmax_{St2Sw}$	*omegaPFmax* in stance-swing transition	rad/s
$omegaPFmax_{LR}$	*omegaPFmax* during loading response	rad/s
omegaRange	Range of ω (ω_{max}–ω_{min}) across stride	rad/s
$omegaRange_{St2Sw}$	*omegaRange* in stance-swing transition	rad/s
omegaRMS	Root-mean-squared of ω across stride	rad/s
omegaSTD	Standard deviation of ω across stride	rad/s
omegaCrest	Crest factor of ω (*omegaRange* ÷ *omegaRMS*)	--
pctStrideDF	Fraction of the stride (time) spent in DF	--
pctStridePF	Fraction of the stride (time) spent in PF	--
torqueMean	Avg. orthotic torque (τ)	N-m
torqueAbsMax	Peak τ (absolute value)	N-m
torqueCum	Cumulative τ (area under torque curve, angular impulse)	N-m-s
powerMean	Avg. device power	W
powerMax	Peak device power absorption	W
powerMin	Peak device power returned to user	W
powerCum	Cumulative power (area under power curve, total work)	W-s, J
workMean	Avg. work (spring energy)	J
workMax	Max. work (peak spring energy stored)	J
workMin	Min. work (peak spring energy returned)	J
workCum	Cumulative work (spring energy stored) over stride	J

3.3.1.5.3 Regression Modeling

We then used these extracted features to construct a regression model for estimating the loading condition of the ankle exoskeleton given some subset of gait parameters. We partitioned the features into two groups: kinematic features, which were derived exclusively from the angle sensor, and kinetic features, which were derived from the torque sensor. We ran two separate regression analyses that used these two groups of features as inputs to be mapped to a single output variable: stiffness (which, again, was the average slope of the torque-angle curve as calculated for each stride, in units of Nm/°). We performed leave-one-subject-out cross-validation (LOSO-CV) on each dataset, wherein a single subject's data is used to evaluate a regression model trained on the remaining subjects' data. This process is repeated so that each subject's data are tested upon exactly once, and the performance metrics—in our case, root-mean-squared error (RMSE) and coefficient of determination (R^2)—of each validation fold are combined (averaged) to reflect overall performance. We evaluated various regression algorithms with LOSO-CV and selected the model with the lowest mean cross-validation error. We then quantified the selected model's performance in terms of mean LOSO-CV RMSE and R^2 between true and estimated stiffness. While most of these models were able to produce relatively low RMSE and high R^2 values, we found that an ensemble method known as extreme gradient boosting ("XGBoost") of regression trees performed best overall [72]. A feature importance ranking was also obtained by performing XGBoost on the full dataset and then ordering the features in terms of their "weight" in the model, or the number of times each feature is used to split the data across all trees [71].

3.3.2 Results

The major results of the PFR and DFR experiments can be seen in Figure 16 and Figure 17, which show the ensemble-averaged device joint angle, torque, velocity, power flow, and work flow for a single, representative subject. The color of each waveform corresponds to a specific loading condition. Each waveform is comprised of a solid line (mean, μ) with shaded error bars (mean +/- one standard deviation, σ). Every graph with "% Stride" on the x-axis shows how the given parameter changes across the average gait cycle, beginning at initial contact (heel strike) and ending with terminal swing. Exoskeleton joint angle across the average stride is shown in Figure 16a and Figure 17a. Figure 16b and Figure 17b show the amount of torque applied by the iAFO to the user, as measured by the reaction torque sensor. Figure 16c and Figure 17c plot the angle and torque waveforms against each other to form a load-deflection curve that reflects the average torsional stiffness of the iAFO in that loading configuration. Figure 16d and Figure 17d represent the average angular rate of the iAFO joint across the average stride—the time-derivative of the waveforms in Figure 16a and Figure 17a. Figure 16e and Figure 17e show the mechanical power delivered by the iAFO to the user (positive values) and power absorbed by the iAFO (negative values), in W. Note that power is absorbed during phases of gait that involve combatting spring tension (e.g., loading response and push-off in the PFR mode, Figure 16e), and power is returned to the user in phases of gait in which the spring return assists motion. Lastly, Figure 16f and Figure 17f represent the net work or elastic energy (in J) stored (positive) and returned (negative) by the springs in the iAFO across the gait cycle—the time-integral of Figure 16e and Figure 17e. Note that energy is stored

in phases of gait in which the springs are stretched, and energy is released during phases when the springs contract.

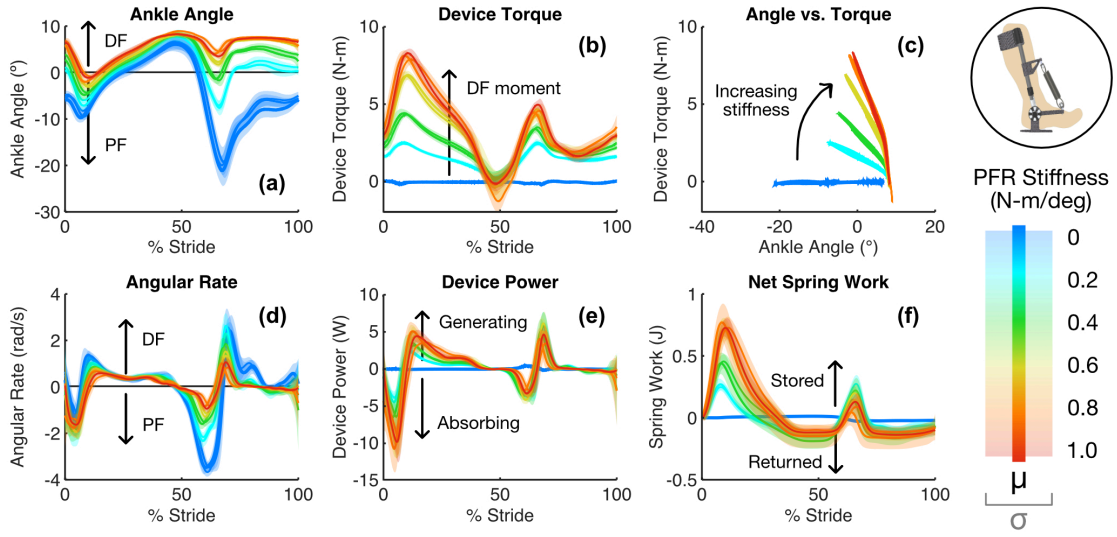

Figure 16. Various ankle joint measures across an average stride for a representative subject walking under graded PFR load. Each waveform represents the average (+/- 1 st. dev.) of ~ 60 strides collected during a treadmill walking task at a distinct PFR stiffness, with the waveform color representing the stiffness condition as explained by the color scale to the right. PFR stiffness increases as color "temperature" increases, from 0 to ~ 1.0 Nm/°.

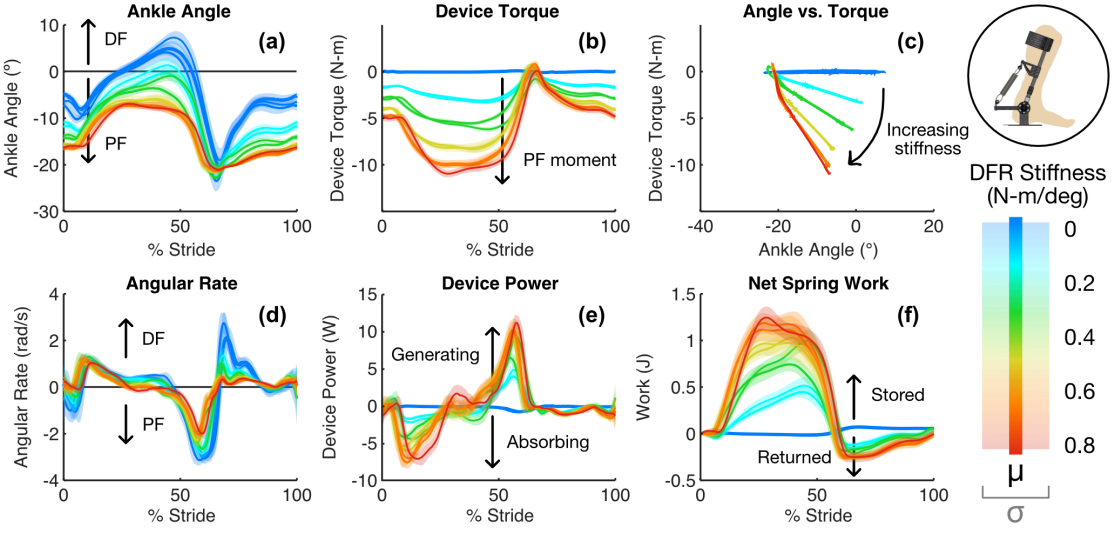

Figure 17. Various ankle joint measures across an average stride for a representative subject walking under graded DFR load. Each waveform represents the average (+/-

1 st. dev.) of ~ 60 strides collected during a treadmill walking task at a distinct DFR stiffness, with the waveform color representing the stiffness condition as explained by the color scale to the right. DFR stiffness increases as color "temperature" increases, from 0 to ~ 1.0 Nm/°.

3.3.2.1 Average Ankle Joint Behavior Under Various PFR Loads

Figure 16a shows how, as PFR stiffness increases, total joint range of motion (ROM)—the peak-to-peak amplitude of each waveform across the gait cycle—decreases. Each curve also shifts progressively towards the DF regime. These observations are intuitive: as the iAFO's springs pull the foot up and make it more difficult to plantarflex, the ankle will bias toward DF, and the subject will find it more difficult to achieve the normal, full ROM. This is especially evident during the "push-off" phase (50-65% stride), where the subject must actively plantarflex to redirect the center of mass upward and forward. This suggests that push-off, the propulsive phase of gait, is particularly disrupted by changes in PFR stiffness. Note that, though a reduction in PF motion did occur during loading response (0-10% stride), the change was not nearly as stark as during push-off. This is likely because PF during loading response is driven passively, primarily by momentum created by trailing limb power, whereas PF during push-off requires activation of the calf muscles on the ipsilateral limb (on which the iAFO is worn).

All subjects demonstrated an unwillingness (or a diminished ability) to engage with the springs during active push-off past a certain threshold of effort. Evidence for this claim can be found at ~ 60% stride in Figure 16{b,e,f}. As PFR stiffness was increased from 0.6 Nm/° (yellow) to 1.0 Nm/° (red), the amount of torque applied by the device, power absorbed by the device, and energy stored in the springs all remained relatively unchanged. In fact, in the latter two cases, these two parameters—joint power expended and work

performed at the ankle to fight against the spring load—appeared to remain constant across all stiffness conditions. This finding suggests that each subject may have adopted a different walking strategy to control for the amount of ankle effort (in terms of calf muscle activation, perhaps) required to walk under these different ankle loads. We suspect that the subjects compensated by generating more power at upstream joints (knee, hip) or on the contralateral limb to stabilize more global gait parameters such as gait symmetry, metabolic cost, etc. However, further testing will need to be conducted to fully capture the extent of this motor adaptation.

Some other interesting and consistent trends in the data include a marked reduction in PF angular velocity (Figure 16d) during push-off (50-60% stride), followed by an almost complete immobilization of the joint during the swing phase (70-100% stride) in the higher stiffness conditions. This suggests that the iAFO acted almost like a rigid ankle brace during the swing phase of gait, keeping the foot at or above neutral (0°), which is important to mitigate the risk of tripping. Finally, since the device relies entirely on passive mechanical components, one would expect both net power and work to sum to zero across each gait cycle. Indeed, both appear to do so, though the work/energy waveforms suggest that the springs do not completely return all the energy that was stored (Figure 16{e,f}). We attribute this to mechanical losses in the iAFO system, perhaps caused by hysteresis in the coil springs or interactions with the leg's soft tissues that may dissipate energy.

3.3.2.2 Average Ankle Joint Behavior Under Various DFR Loads

Figure 17 demonstrates a similar set of ensemble-averaged results as above (from the same representative subject as before) but this time for the DFR experiment set. Figure

17a illustrates that, as DFR stiffness increases, overall ankle ROM decreases, and the waveforms bias progressively more toward PF ($\theta < 0°$). This result is intuitive, as the posterior-mounted springs have the effect of pulling the foot down. Figure 17b shows how the PF moment produced by the exoskeleton scales with increasing DFR stiffness. Comparing Figure 17c to Figure 16c demonstrates that the device applies torsional stiffness symmetrically (i.e., in both the PF and DF directions) across all stiffness conditions in both resistance modes. In Figure 17d, as in Figure 16d, the joint angular rate decreases with increasing DFR stiffness, though the reduction is far more severe in phases of gait in which active DF (i.e., contraction of the dorsiflexor muscles) is required, such as initial swing (65-75% stride), when the user must actively lift the foot up to avoid dragging the toe after push-off.

Figure 17{e,f} demonstrate how, when the springs are loaded during early and mid-stance (10-50% stride), the exoskeleton absorbs power and stores elastic energy in the springs. This is then released and returned to the user to assist with push-off (50-65% stride). Interestingly, while the amount of power *absorbed* by the anterior-mounted springs during push-off remained constant as *PFR* stiffness increased (Figure 16e, 50-65% stride), the amount of power *returned* by the posterior-mounted springs during this same phase actually increased as *DFR* stiffness rose, up to the 0.6 Nm/°condition (Figure 17e, 50-65% stride). This suggests that a device with a sufficiently high torsional stiffness in DF, if loaded properly by the user during stance, can provide more push-off assistance to the user than an exoskeleton that is less stiff in DF. This is the concept behind many AFOs, such as the posterior leaf-spring variety, that boast an energy return during the propulsion phase of gait. However, our results show that, at least for healthy subjects who were not explicitly

trained to load the device properly, there exists a limit on the amount of power / assistance that a device of a given stiffness can return to a user. This information is potentially valuable for the design and optimization of passive-elastic exoskeletons whose goal is to improve walking efficiency.

3.3.2.3 Feature Extraction and Relationship to AFO Stiffness

Figure 18 illustrates how a subset of extracted features change in response to either PFR stiffness (top) or DFR stiffness (bottom). Each feature value is plotted against the calculated torsional stiffness on the x-axis. In an ideal case, this calculated stiffness value would be the same across all strides at each loading condition, since the configuration of the device does not change during the walking trial. However, due to certain losses and idiosyncrasies (e.g., in exo-limb contact), the slope of the measured torque-angle curve varies slightly step-to-step. This is why the points are not all stacked perfectly vertically at each distinct location on the x-axis but rather are grouped around a centroid stiffness value. Every circular marker represents a feature extracted from an individual stride. For continuity's sake, these results are drawn from the same representative subject as reported in Figure 16 and Figure 17, though the general trends in these features were highly consistent across subjects.

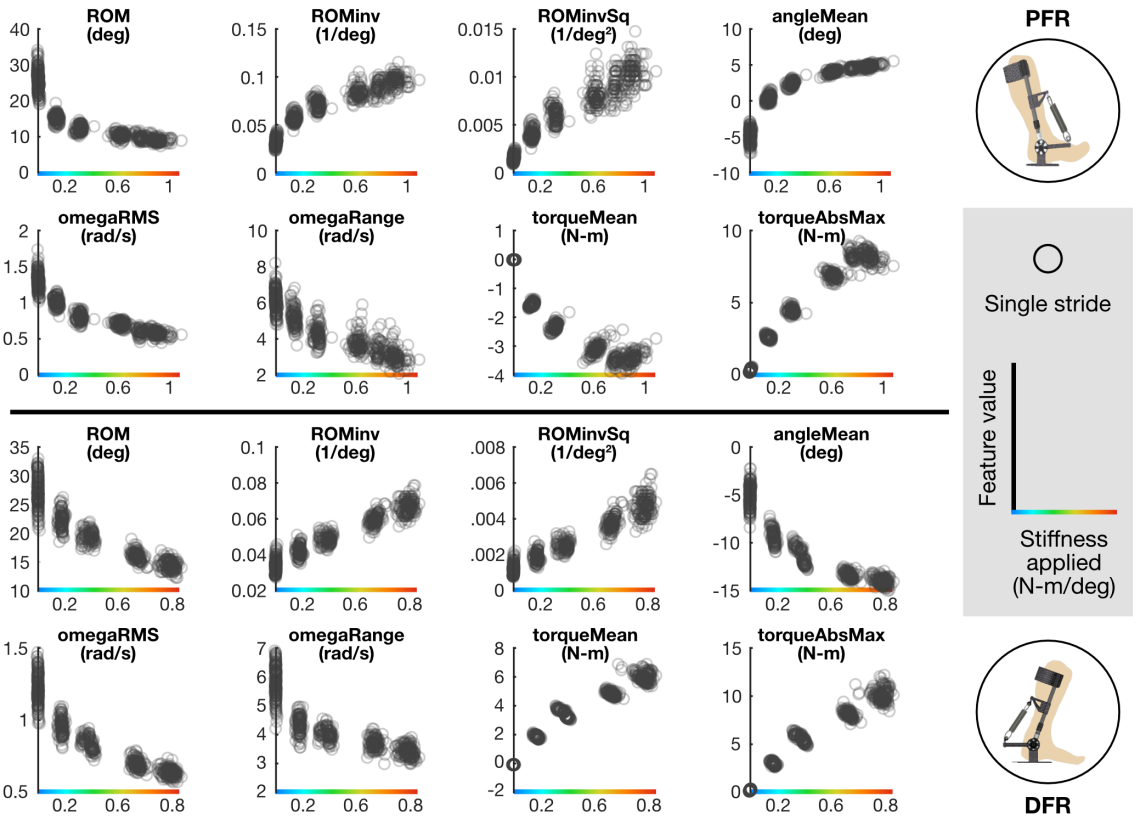

Figure 18. A collection of stride-specific gait mechanic features extracted from the data of a representative subject walking under both graded PFR (top) and graded DFR (bottom) load. Each circular marker represents the feature extracted from an individual stride, and the value of that feature (on the y-axis) is plotted against the stiffness value at that given stride (on the x-axis).

Most of the features, including all depicted in Figure 18, followed a monotonically increasing or decreasing relationship to stiffness. However, an interesting point of comparison between the effect of PFR versus DFR load can be seen in the *ROM* results specifically. In normal gait, ankle *ROM* is captured in the terminal stance/pre-swing phase (50-65% stride), in which active PF is performed. It stands to reason, therefore, that *ROM* would be more affected by incremental changes in PFR load than by changes in DFR load. In fact, this appears to be true, as *ROM* decreases more rapidly in response to PFR load than DFR load, until it reaches an asymptote. This asymptotic behavior suggests that there

exists a threshold PFR stiffness beyond which users will no longer try to combat a parallel elasticity. The shape of the PFR-*ROM* relationship looks somewhat like an inverse function. Indeed, *ROMinv* (ROM^{-1}) and *ROMinvSq* (ROM^{-2}) demonstrate an approximately linear relationship with PFR stiffness. In DFR, however, *ROM* itself appears to follow a strongly linear trend with no such discernable asymptote.

Under both PFR and DFR loading, *ROM* and *omegaRange* (the range of joint velocity achieved across each stride) exhibit higher variance at lower stiffness conditions, suggesting that step-to-step variability is higher when a lower elastic load is applied to the ankle joint. This may suggest that, for a higher elastic load at the joint, a user might lose some capacity for fine motor adjustment that could otherwise be useful in adapting to a walking surface, changing speed, etc.

3.3.2.4 Regression Modeling to Estimate Device Stiffness

The results of our machine learning model-based approach to estimating exoskeletal ankle stiffness are reported in Figure 19, where the value of stiffness predicted by the XGBoost model trained on a subset of kinematic features is compared to the true exoskeletal stiffness applied. Figure 20 demonstrates the individual contribution of the top 10 overall features to the model. Both kinetic and kinematic features are ranked, though only kinematic features were used in the model illustrated in Figure 19. These results demonstrate the value of a diverse feature set and can give insight into which features have the greatest bearing on the output variable.

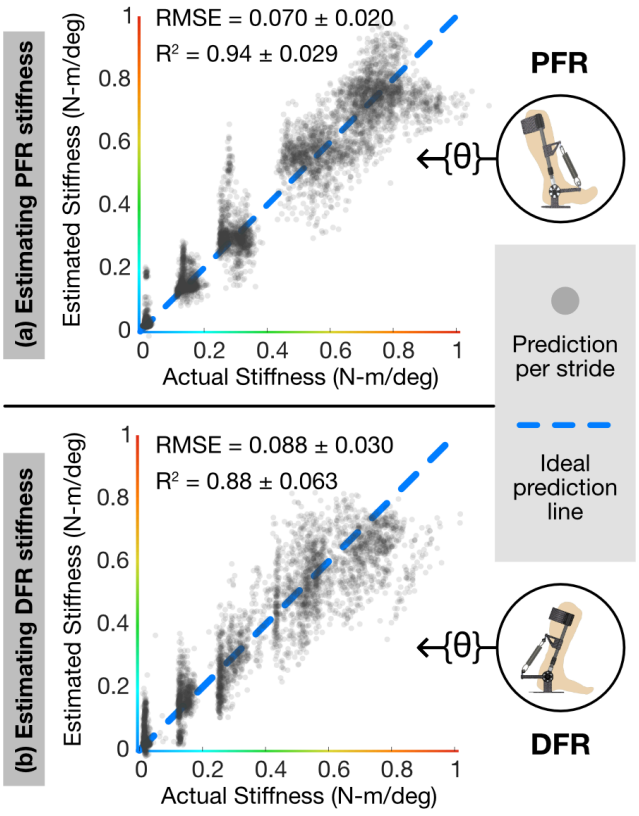

Figure 19. Output of boosted regression tree (XGBoost) method for estimating either (a) PFR or (b) DFR stiffness from ten kinematic features exclusively derived from the optical encoder signal. These results demonstrate that, for healthy individuals walking under similar conditions, information gathered by a single sensor that measures the shank-foot angle can be used to extrapolate information about the external load applied to the ankle joint.

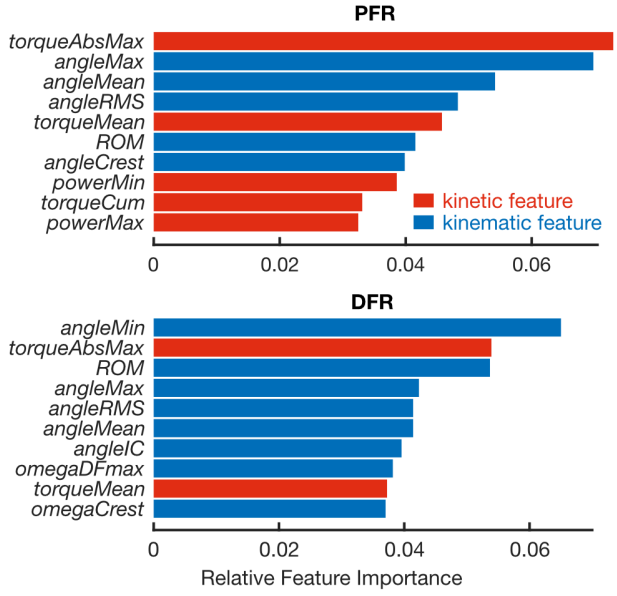

Figure 20. Relative contribution of the top 10 individual features used by the XGBoost regression model. Feature weighting, or importance, is based on how often the variable is split upon across all decision trees generated by the algorithm. A higher value suggests a more informative feature.

3.3.2.4.1 Under PFR Load

Figure 19a illustrates the central result of a boosted regression tree analysis (XGBoost) on the PFR loading dataset. In it, we plot PFR stiffness as estimated by the subset of kinematic features (i.e., those solely derived from the joint angle sensor) against the true exoskeletal stiffness of our test set. When we included both kinematic and kinetic features in the model, we were able to achieve superior performance (RMSE = 0.05 ± 0.02 Nm/°, R^2 = 0.96 ± 0.03) as compared to our model that used kinematic features alone as inputs. This result was expected, however, since stiffness can be not only estimated but indeed directly *calculated* when both torque and angle are known. Nevertheless, though performance suffered slightly when kinetic features like *torqueAbsMax* are removed, the

overall capability of kinematic features alone to estimate stiffness is still strong (RMSE = 0.07 ± 0.02 Nm/°, R^2 = 0.94 ± 0.03) (Figure 19a). It seems that the set of kinematic-only features less reliably estimates stiffness in the lower range of stiffness values—the ~0.3 Nm/° regime in particular.

3.3.2.4.2 Under DFR Load

Similarly, Figure 19b illustrates the model performance of the XGBoost algorithm when subjects walked under DFR load. Similar to the PFR regression results, model accuracy was superior when kinematic *and* kinetic features were both incorporated (RMSE = 0.06 ± 0.03 Nm/°, R^2 = 0.93 ± 0.05), while the model limited to merely kinematic features produced marginally worse—though still admirable—estimations of DFR stiffness (RMSE = 0.09 ± 0.03 Nm/°, R^2 = 0.88 ± 0.06) (Figure 19b). As with the PFR stiffness model results, when kinetic features were removed from consideration, prediction error in LOSO CV increased, particularly in the lower DFR stiffness regime. Test errors were comparable between PFR and DFR models, with DFR stiffness estimated slightly worse (RMSE = 0.09) than PFR stiffness (RMSE = 0.07).

3.3.3 Discussion

3.3.3.1 Limitations

Our ankle exoskeleton design demonstrated some mechanical limitations, one of which is that we were only able to resist the two directions of sagittal-plane ankle motion independently, not simultaneously. In future studies, we hope to determine the effect of fully bilateral ankle stiffness. Furthermore, because we used one-way extension springs as

the loading mechanism, we were unable to set the zero-torque point of the iAFO at the anatomical neutral position ($\theta = 0°$) without producing a nonlinear torque profile near the end-range of ankle motion. This limitation and the balancing act associated with it was discussed in more detail in Section 3.2.8.2. Because the goal of this work was generally to examine the effect of elastic load on ankle mechanics, these were seen as minor peculiarities; however, if, in the future, we were to compare the function of the iAFO to more conventional devices like ankle-foot orthoses, these limitations would need to be addressed more intently.

Finally, it should be noted that both the joint angle and torque measurements reported were measured on the chassis of the iAFO itself, not on the wearer's limbs. Therefore, if there had been any relative motion between the frame of the device and the user's shank and foot, the optical encoder would not have captured the actual anatomical ankle joint angle. Furthermore, since we only used sensors localized to the user's right ankle, we were unable to assess possible compensations at other joints or the contralateral limb, effects on gait symmetry, etc. To address these limitations, further experiments could be conducted with the iAFO worn in parallel with full-body motion capture. This would also expand the set of relevant gait features that could be correlated with ankle stiffness.

3.3.3.2 Impact and Potential Applications

We believe that the results of Figure 19 represent an especially exciting outcome of this work. We demonstrated that, by using only a subset of gait features extracted from a single sensor (the optical encoder), our model can reliably estimate the loading conditions (i.e., stiffness in either DF or PF) imposed by the exoskeleton at a joint (i.e., the ankle).

This suggests that, if one assumes the load applied by an exoskeleton is elastic in a certain direction of joint motion, given only a single sensor to capture joint angle across a stride, one can *estimate* the stiffness applied at that joint, within some confidence interval. Armed with this information about the device mechanics, one can then infer, or map to, useful kinetic information such as exoskeletal torque (the product of measured joint angle and estimated joint stiffness), power flow through the device (the dot product of measured joint rate and calculated device torque), and device energy/work flow (the time-integral of calculated device power) across the gait cycle.

Of course, in a trivial case, the stiffness of a system could simply be measured with a load sensor such as the torque sensor used here. Indeed, in our study, we measured torque directly so that we would have a ground truth (a calculated stiffness) to which to compare our stiffness estimate. However, sensors such as these tend to be bulky, expensive, power-inefficient, and/or require extensive interface circuitry. Moreover, this class of sensors might be difficult to integrate into certain types of devices such as soft exo-suits (e.g. [119], [120]) or else be unsuitable for use in austere or ambulatory settings. Therefore, any means of obtaining kinetic information without the need for such a sensor would be of considerable benefit.

A more conventional solution might be simply to characterize the device offline—by measuring its stiffness on the benchtop—and then deploy it without a load sensor. However, there are contexts in which the stiffness of a system might be difficult to assess even on the benchtop, such as a soft robotic system mentioned above, one that uses a flexible material, textile, etc., as its means of applying an external torque, or one without a defined axis of rotation around which to measure torque. Furthermore, if the system whose

stiffness is measured once offline is then deployed for extended periods of time, it is possible that its elasticity will change over time due to fatigue, rendering the initial calibration inadequate.

A model for estimating stiffness using only kinematic data would enable a device with only an angle sensor—which can be low-profile, lightweight, low-power, and inexpensive, such as inertial sensors (accelerometers, gyroscopes)—to deduce kinetic attributes of gait without the need for a load sensor. We believe this could be of real value in the domain of wearable devices, where size, weight, and power consumption are key constraints. Wearable devices such as ankle braces/orthoses could be instrumented with motion sensors like accelerometers, collect joint motion data over a series of strides, use a similar machine learning approach to estimate brace stiffness, and then report on how much power or energy a person is expending per stride, how much assistance versus hindrance it offers during loading response and push-off, etc.

Most importantly, we view this work as a framework for future studies that would use the same methodology of coupling wearable sensing with sensor fusion and machine learning to assess human-exoskeleton interaction. This approach could be especially useful when trying to estimate noisier or more difficult-to-measure signals (e.g., underlying physiological states like muscle dynamics, tendon elasticity, or metabolics) using more easily obtained data (e.g., exoskeleton kinematics).

3.4 Conclusion

Studying how humans interface with exoskeletal devices can provide valuable insight into natural adaptation mechanisms and can help develop methods to make these

devices best serve an individual's need. The results and methodologies reported in this work represent a novel approach of in-depth, joint-specific analysis to study the effect of externally applied joint torques on gait. In particular, we have demonstrated that, under a defined set of conditions/assumptions (healthy subjects, level walking, gait velocity = 1 m/s, elastic loading at the ankle), given information gathered by a single sensor that can measure shank-foot angle, one can use feature extraction and machine learning techniques to extrapolate kinetic information about an exoskeleton's effect on the joint, without the need for a load sensor or offline characterization of the device. And assuming the human neurophysiological response to elastic loading at the joint is consistent regardless of how that stiffness is rendered (i.e., whether via a rigid frame-type device such as ours, a deformable piece of material, or an impedance produced by a motor)—an interesting question unto itself—this approach could be generalized to a wider variety of exoskeletal devices. Moreover, portions of this work detailing joint sensing, feature extraction, and model-based estimation of exoskeletal stiffness could be applied to other joints under different loading conditions. Further, this approach could be implemented in wearable systems for everyday use, as the demands of sensing and feature extraction are well within the capabilities of modern wearable sensors and microcontrollers. For example, a subject could wear an exoskeleton embedded with inertial sensors and a microcontroller to extract stride-specific kinematic features. These features could then be used to construct a model to predict the exoskeleton stiffness that would achieve the desired set of gait parameters that are most critical to that user. These insights and the general experimental framework can be used to characterize wearable systems whose mechanical properties may otherwise be difficult to assess, to predict how a user might adapt to similar joint perturbations, and

to complement the mechanical tuning of exoskeletal devices that affect joint motion. We believe that an integrated, wearable system that uses human-in-the-loop design in everyday tasks in this way could have a deep and abiding impact, helping pave the way for smarter wearable devices that adapt to the needs of a user.

From a clinical standpoint, the prevalence of lower-limb motor impairments and the relative lack of quantitative outcome measures for therapeutic solutions presents both a gulf in the clinical approach to treatment as well as a compelling opportunity for the development and implementation of devices designed to (1) diagnose and quantify specific deficits, (2) assess the efficacy of treatment and the pace of recovery, and (3) ultimately inform patient-specific approaches to treatment optimization. We believe that our device, the iAFO, represents a significant advancement towards objective assessment and optimization of ankle-foot orthoses for the treatment of foot drop and potentially other motor deficits impacting the lower limb. With its extensive sensor suite, robust construction, and capacity for user-defined stiffness modulation, we believe it is a clinical tool well-suited to the diagnosis and study of foot drop in particular, as well as a scientific tool for studying how manipulating ankle joint stiffness affects locomotor function. Our validation tests demonstrate that the iAFO is capable of both applying orthotic resistance and monitoring an extensive set of relevant physiological parameters in a repeatable and reliable manner. The results of a pilot study using the iAFO, though preliminary, are striking and suggest a noteworthy change in a healthy person's ankle joint kinematics in response to perturbations of the ankle joint, though a more thorough analysis of other signals (e.g., EMG, interface pressures) and a larger and more anatomically diverse subject population is required to make any definitive claims. Nonetheless, the quality and

comprehensiveness of the data collected present a rich opportunity for further, robust data analysis and algorithmic development, particularly in potential studies on populations with gait abnormalities such as foot drop. Furthermore, the results of these validation experiments serve as a proof-of-concept for our device and highlight its capabilities in gait studies of this sort, making us optimistic for future investigations, applications, and developments of the iAFO or other "smart" orthoses of its ilk.

3.5 Evolution of (and Beyond) the iAFO

All of the above experiments were performed using a version of the iAFO that required the user to wear a backpack (housing all the peripheral devices) and be tethered both to wall power and to a computer via USB. As a device of this nature could not be considered "wearable" by reasonable standards, we devoted additional effort to developing a fully untethered—and, therefore, truly wearable—version of the iAFO (which used an onboard microcontroller, SD card, and power source) to capture a rich set of biomechanical parameters in a form factor that could be taken away from the benchtop and outside the lab or clinic (Figure 21).

Using the iAFO as a scientific tool allowed us to arrive at a novel result: that, under elastic ankle loading, device kinetics (i.e., stiffness) can be estimated purely from kinematics (i.e., joint angle) during walking. In a sense, we demonstrated that, using ML techniques, information from an accessible (i.e., low-footprint, easy-to-integrate, inexpensive) wearable sensor could be used to extract information from an inaccessible (i.e., bulky, expensive, power-consumptive, difficult-to-integrate) wearable sensor. Though this is a potentially useful result for the development of economical, "smart"

orthoses, a more compelling task might be to use information from a wearable sensor to elucidate a more difficult-to-assess, biologically intrinsic variable (e.g., internal joint load). To meet this task would require a noninvasive sensing technique capable of providing a "window" through the skin—one that could reveal an underlying biomechanical loading state. In the following chapters, we address this challenge by leveraging a novel sensing modality based on the local acoustic response of the joint.

Figure 21. Fully wearable, untethered iAFO system. This version of the device, which is battery-powered and uses a small microcontroller to record joint angle (magnetic encoder), torque (reaction torque sensor), limb orientation (IMUs), and heel / forefoot contact (FSR), is self-contained and designed for use outside the lab / clinic.

CHAPTER 4. PHALANX: MANUAL SENSING OF JOINT ACOUSTICS—A WINDOW BENEATH THE SKIN

4.1 Introduction

Injuries and chronic disorders affecting joints are pervasive and degrade quality of life for millions of individuals [2], [3]. The knee joint, due to its anatomical complexity, role in weight bearing, and high, cyclical exposure to mechanical stress, is particularly susceptible to injury [6]. The current diagnostic standard for acute joint injury and chronic conditions such as osteoarthritis involves a combination of medical imaging, which can be costly and time-intensive, and physical examination, which often relies on subjective evaluations made on the part of either the clinician or the patient. Moreover, these methods are not ideally suited to longitudinal, comprehensive monitoring of joint health, which may benefit recovery.

Accordingly, recent work has demonstrated the viability of using the acoustic emissions produced by joints in motion—in particular, the knee—as an indicator of underlying joint health. McCoy *et al* referred to the concept of sensing skin vibrations (i.e., their local accelerations) caused by joint articulation as "vibroarthrography" [56]. These vibrations produce an acoustic response in the surrounding media, which is why the signal is often termed a "joint sound" or "acoustic emission." Arthro-acoustic techniques have been explored in both clinical [68], [121], [122] and ambulatory settings [123], using both benchtop and wearable equipment [124]. Results from these studies have demonstrated an ability to discriminate reliably between the acoustic signatures of healthy and impaired

joints [59], [68], and those of joints under varying mechanical load [65]. The latter study validated the use of a vertical leg press as a reliable paradigm for modifying the acoustic output of a healthy knee, demonstrating a change in the heterogeneity of the joint sound as a function of percent body weight applied.

More recently, our group has begun to explore the use of alternative form factors for collecting joint sounds that would improve the quality and reliability of the measurements and eliminate the need for consumables like tape and adhesive microphone pads, which are the conventional means of mounting acoustic sensors on the skin. Drawing inspiration from manual auscultation, we designed a system in which contact microphones are embedded in a glove and placed at locations of interest around a joint to collect arthro-acoustic data. This approach offers several advantages, including the ability to finely regulate contact pressure at the sensor-to-skin interface (by leveraging the user's inherent motor control and tactile feedback mechanisms) while removing interface noise caused by adhesive, fabric, or other material interacting with the skin. Additionally, an adhesive-based solution is not ideally suited to applications involving repeated use, such as longitudinal tracking in a home setting. Conversely, a hand-worn system such as the one proposed in this work could be easily and repeatedly administered, and, furthermore, would provide an opportunity for an individual to actively engage in the management of one's own or a dependent's care—for example, a parent might use the glove to collect joint acoustic data on a child suffering from juvenile idiopathic arthritis.

In this study, we employed the healthy subjects vertical leg press paradigm (Figure 22) as a means to validate the glove-based approach, alongside two more conventional mounting techniques: fabric tape and adhesive foam mic pads. Achieving a similar result

in terms of a quantity that reflects the internal state of the knee joint—i.e., the loudness of grinding—across these techniques would suggest that a glove-based system can provide clinical value comparable to more established techniques without the need for consumables. Multi-day repeatability testing was also conducted to assess the reliability of results derived from the glove-based system, as well as their agreement with results derived from conventional techniques.

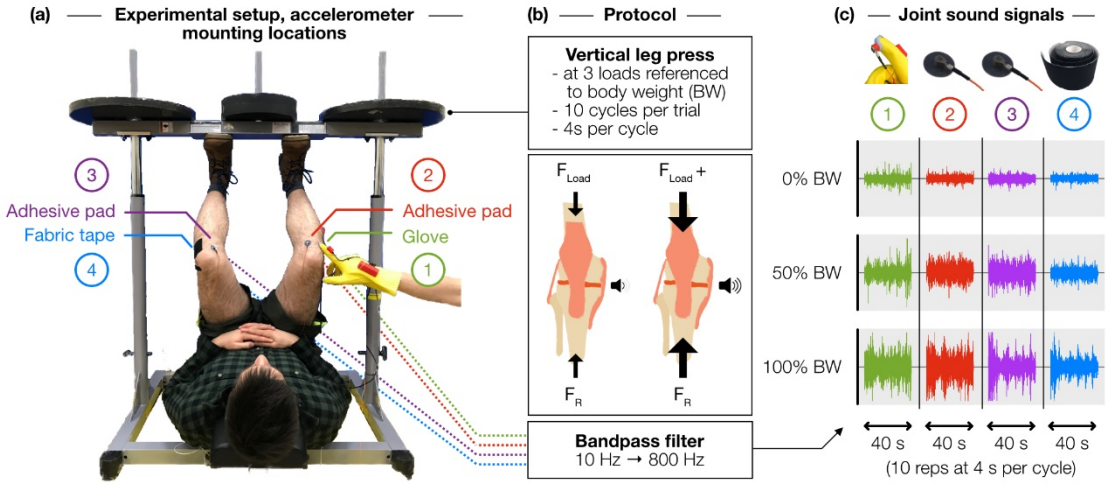

Figure 22. Experiment overview. (a) Four accelerometers were placed at regions of interest around the knee joint using different mounting techniques, and, in parallel, recorded vibrations produced by the joint during a vertical leg press exercise. (b) Increasing normal forces within the joint, we hypothesized, would increase the loudness of low-frequency grinding sounds within the knee. (c) Representative joint sound waveforms demonstrate how the amplitude of low-frequency vibrations increased as a function of percent body weight applied.

4.2 Methods

4.2.1 Design of a Glove-Based Form Factor

Our glove-based arthro-acoustic sensing system consists of (1) a glove to which various sensing and data acquisition components are mounted, (2) one or more fingertip modules in which the contact accelerometer and force sensor are integrated, and (3) a

microcontroller for collecting data and driving feedback mechanisms for fingertip force regulation (Figure 23).

We used a latex/neoprene cleaning glove (Playtex, Dover, DE, USA), because it is easy to disinfect and because its elasticity enables a solid, contoured fit to the user's digits. Good coupling between the glove/sensors and the hand is critical for maintaining stable contact at the user–subject interface to minimize motion artifacts.

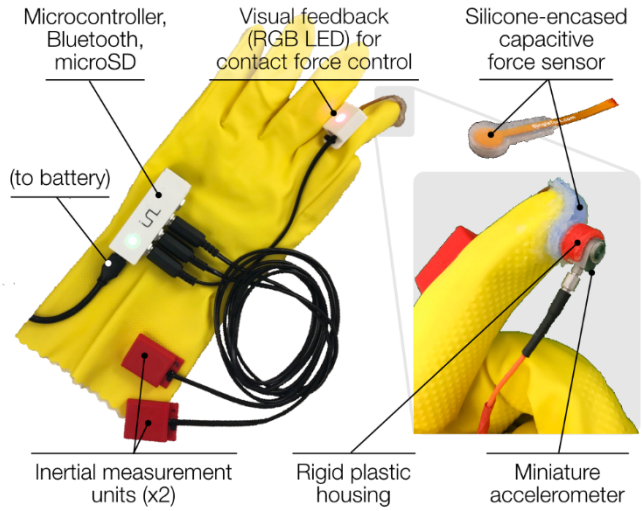

Figure 23. Design of a glove with embedded sensors for capturing joint sounds (accelerometer) and other contextual signals (inertial measurement units for limb motion, capacitive force sensor for sensor–skin contact pressure).

Sensing of the joint sound signal occurs at the fingertip, where a miniature, high-bandwidth, uniaxial accelerometer (sensitivity = 100 mV/g, frequency response ±10% = 2 to 10,000 Hz) (series 3225, Dytran Instruments, Inc., Chatsworth, CA, USA) is placed in a rigid plastic housing. The accelerometer is sensitive enough to resolve small vibrations caused by the articulation of the internal components of the knee joint that travel to the skin surface [62].

Sandwiched between the accelerometer and the fingertip is a capacitive force sensor (CS8-10N, SingleTact, Los Angeles, CA, USA) encased in silicone rubber (OOMOO 30, Smooth-On, Lower Macungie, PA, USA). The force sensor (full-scale range = 0–10 N) measures contact pressure between the accelerometer and the subject's skin. The utility of this measurement is twofold. First, it complements the acoustic signal captured by the accelerometer, providing context such as whether inconsistent contact is made, potentially a source of signal artifact; such context clues can help the researcher gauge the quality of the joint sound recording. Second, the contact force measurement, in conjunction with real-time sensory (e.g., visual, haptic) feedback, can be used as a mechanism for training users to apply consistent pressure at the sensor-to-skin interface, reducing inter-trial and inter-user variability of recordings. In our system, a multi-color LED on the dorsal surface of the index finger provides visual feedback of sensor contact force via an LED color scheme. A green light indicates that the user is pressing within a desired range of contact force for consistent signal acquisition, with light color changing from blue to red as force exits this range (Figure 24b). This feedback mechanism helped ensure that consistent contact pressure was maintained across trials and across subjects. Intermediate values of contact force (roughly between 4 and 7 N) were found to produce repeatable results in terms of root-mean-squared (RMS) amplitude in the frequency band of interest, while pressing too hard (between 8 and 10 N) led to discomfort in some subjects. The current study did not directly assess the effects of contact force on signal properties, which is a limitation of the current approach that will be discussed further. The capacitive force sensor itself, though accurate and reliable, is delicate and prone to delamination, so the custom silicone rubber mold protects the sensor from damage while still allowing it to deflect and measure force.

Besides sensor–skin interface force, another potentially important variable to account for is the motion of the joint being assessed. To ensure consistent knee joint displacement and velocity—which can affect the acoustic output of the joint [124], [125]—across repetitions of the leg press, we integrated two inertial measurement units (IMUs) (BNO055, Bosch Sensortec, Reutlingen, Germany)—one for the shank segment and one for the thigh—into the glove design. These particular sensors are able to perform onboard sensor fusion and thus output a quaternion estimate. These quaternions are used to estimate the knee joint angle across the leg press maneuver.

Data from the capacitive force sensor and both IMUs (Figure 24{a,b}) were collected by a Teensy 3.6 microcontroller (PJRC, Sherwood, OR, USA) at a sampling rate of 100 Hz and logged on a microSD card. The microcontroller was housed in a custom enclosure, along with a Bluetooth module (SPBT3.0DP1, STMicroelectronics, Geneva, Switzerland) for streaming data to a laptop and sending/receiving a start/stop signal from MATLAB (MathWorks, Natick, MA, USA). A National Instruments data acquisition unit (USB-4432, Austin, TX, USA) was used to collect the acoustic signals from the four accelerometers at 50 kHz per channel.

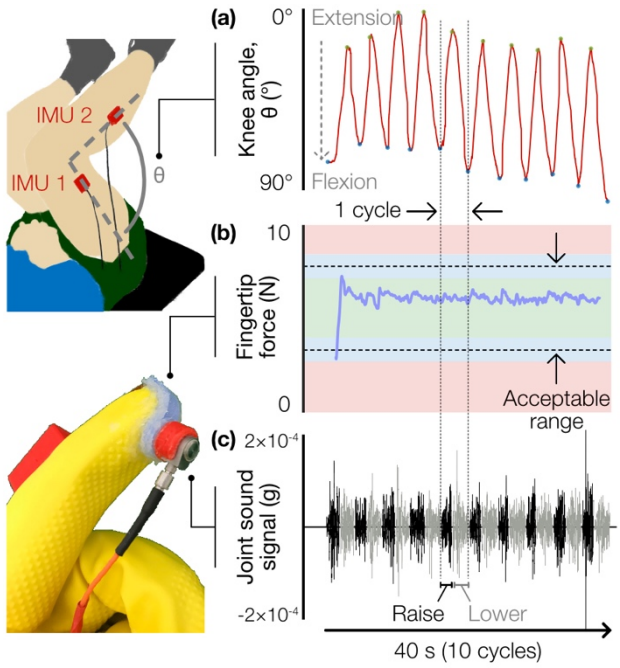

Figure 24. Sample time-series waveforms of signals collected by the glove system during a single experiment trial, consisting of 10 vertical leg press cycles. (a) IMUs were used to confirm that consistent knee range of motion (in degrees, °) was achieved at a constant cadence and to segment the joint sound signal into individual cycles. (b) Contact force (in N) at the fingertip was measured to confirm a consistent amount of pressure was applied. (c) The joint sound signal (local acceleration, in g) was captured by a fingertip-mounted vibration sensor and segmented into cycles consisting of extension ("raise") and flexion ("lower") phases.

4.2.2 Loading Experiment Protocol

All human subjects research was conducted under approval from the Georgia Institute of Technology Institutional Review Board. Eleven healthy subjects (seven male/four female, 25.1 ± 2.5 years, 71.4 ± 16.5 kg, 177.5 ± 11.4 cm) with no history of major knee injury were asked to perform a vertical leg press exercise at three loading conditions referenced to body weight (BW)—0% BW, 50% BW, and 100% BW—while the joint sound signals from both knees were recorded simultaneously by four accelerometers—two on each knee. The accelerometer placement scheme is shown in

Figure 22a. These locations have been shown to be effective for capturing the vibrations internal to the knee, and, importantly, they are anatomical landmarks that are easy to locate and provide relatively unimpeded (i.e., by muscle and fat) access to the internal joint space [61]. One accelerometer was affixed lateral to the patellar tendon of the left knee using fabric tape (Kinesio Tex, Kinesio, Albuquerque, NM, USA). Two accelerometers were affixed medial to the patellar tendon of both knees using double-sided adhesive foam microphone pads commonly used for skin-mounting lavalier microphones (23 mm Stickie, Rycote, Gloucestershire, UK). These sensors, attached to the corresponding locations on either knee using the same mounting technique, served as a matched comparison to indicate whether a subject's left and right knee produced disparate results; in this case, a comparison across all four accelerometers would be invalid. Both the fabric tape and microphone pads have been used previously [61], [62], [65]. Finally, an accelerometer on the index fingertip of the glove was placed against the right knee lateral to the patellar tendon. For consistency, the glove-based acquisition was performed by the same individual for all subjects.

At each loading condition, the subject performed 10 repetitions of the leg press maneuver at a rate of one repetition every 4 seconds (i.e., raise for 2 s, lower for 2 s, repeat). Subjects were asked to traverse the same joint displacement each repetition, which was confirmed visually by marking off upper and lower positions on the leg press machine pylons. Consistent cadence was confirmed by ensuring that the time elapsed between each successive flexion-extension (FE) cycle—i.e., time between local minima of the joint angle estimation—deviated no more than 0.2 s from the ideal 4-s period. Loading conditions were randomized to minimize fatigue and learning effects. Two trials were conducted for each condition to confirm a consistent result.

4.2.3 Signal Processing and Data Analysis

We hypothesized that increasing vertical loading in healthy individuals would cause the articular surfaces in the knee to grind together more forcefully, thus increasing the loudness of the sounds associated with grinding (Figure 22b). By both visual and auditory assessment, we concluded that these grinding sounds were consistent with the lower-amplitude, lower-frequency component of the accelerometer signal. This hypothesis is supported by the fact that other joint sound sensing methods tend to focus on the low-frequency spectrum (<1 kHz) [57]. To that end, we posited that low-pass filtering the signal and then computing its RMS amplitude would give us a reasonable metric for grinding loudness.

The signals were digitally filtered using a Kaiser-window finite impulse response bandpass filter with bandwidth from 10 to 800 Hz. Frequency content below 10 Hz was removed to account for baseline wander of the accelerometer signal caused by coarse movement of the limb during the leg press task. This filtering approach is distinct from that of other work such as Reference [60], in which the primary goal was to capture large-amplitude, high-bandwidth peaks (“clicks” of the joint) in the acoustic signal. In those studies, air microphones offset from the skin surface were used to record the joint sounds instead of contact microphones placed against tissue; in such a scenario, the low-frequency, low-energy acoustic waves would be greatly attenuated at the skin–air interface, so their contribution was not considered.

IMU data were used to segment the filtered data into cycles (10 cycles per recording) (Figure 24c), and the signal RMS was computed on a cycle-to-cycle basis.

Outlier RMS values (those that were more than three mean absolute deviations from the median) were rejected, and after confirming that the fingertip force and joint range of motion across each cycle were within acceptable ranges (Figure 24{a,b}), the remaining RMS values were averaged, yielding a single mean RMS value per loading condition for each subject. Each RMS value was normalized to that subject's baseline RMS (i.e., the RMS value at 0% BW). This allowed for comparison of grinding loudness across subjects while minimizing inter-subject baseline RMS variability.

4.2.4 Repeatability Testing: Protocol and Analysis

4.2.4.1 Comparison of Repeatability between Mounting Techniques

To determine whether the glove-based joint sound sensing system can produce consistent, repeatable, and reliable measurements from cycle to cycle and from trial to trial, we analyzed the joint sounds from a single subject over three days using intraclass correlation coefficient (ICC). ICC is a widely used technique for assessing the degree of correlation and agreement between measurements [126], [127].

The glove-based system and the two conventional mounting techniques (fabric tape and foam microphone pads) were used for comparison. Using each of these techniques, the accelerometer was placed on the medial side of the patella, and the subject was asked to perform five cycles of FE per trial, with three such trials conducted for each mounting technique. The signals were digitally bandpass-filtered (10–800 Hz, same as described above), and several key features commonly used in acoustic analysis were extracted for each FE cycle: acoustic energy, energy entropy, and median normalized frequency of the power spectrum. The data were organized into a matrix in which each row represented a

single trial and each column represented a single FE cycle. A total of four datasets were used, three of which exclusively included trials of each of the three mounting techniques, with the fourth dataset containing all trials across all three mounting techniques. The three individual datasets were used to evaluate the internal consistency of each of the mounting techniques, while the combined dataset was used to assess the level of agreement among the three mounting techniques. Using the two-way random effects model [126], ICC values were calculated for each dataset to show the reliability of acoustic features calculated both across FE cycles and across trials.

4.2.4.2 Effect of Fingertip Contact Force Consistency on Repeatability

As mentioned previously, a capacitive force sensor embedded in the fingertip of the glove system provides information about sensor-to-skin contact—inconsistent or inadequate contact could produce artifacts in the joint sound signal, and, therefore, unreliable results. To assess the value of the force sensor experimentally, a single subject was asked to perform a seated, unloaded knee FE task while joint sound signals were acquired by a glove-mounted contact microphone at the same mounting position used in the loading experiment described above (i.e., lateral to the patellar tendon of the right knee), along with contact force and IMU data. Testing was performed on a single-subject basis to reduce the contribution of inter-subject variability on results. The subject performed eight trials of unloaded FE at the same cadence as the loading experiment (one repetition every 4 s), with each trial lasting 30 s in total. Across all eight trials, four were conducted under conditions of consistent contact in which the experimenter relied on visual feedback from the RGB LED to modulate fingertip force; the other four trials were conducted under conditions of inconsistent contact, in which the sensor occasionally lost contact with the

skin due to imprecise fingertip force control. Repeatability of results was analyzed on a within-trial (i.e., between each FE cycle) and across-trial (i.e., average of all FE cycles from all four trials) basis. Specifically, consistency of the feature of interest, low-frequency RMS amplitude, was quantified using standard deviation (SD) and coefficient of variation (CV)—the ratio of sample standard deviation to sample mean—as metrics of reliability and repeatability.

4.3 Results and Discussion

4.3.1 Effect of Leg Press Load on Knee Grinding Loudness

The key result of this study is illustrated in Figure 25, which shows that relative grinding loudness (RMS of the low-pass-filtered joint sound signal, referenced to the no-load, or 0% BW, condition) within the knee increased significantly ($p < 0.01$, using paired sample t-test with Holm–Bonferroni correction) and monotonically with vertical loading for all three mounting techniques across subjects. Furthermore, comparison across techniques at each loading condition showed no significant ($p < 0.01$) differences in grinding loudness between the glove, mic pads, and tape. This finding—in particular, that the glove achieved a comparable result (both in terms of the actual RMS quantity and its relationship to the test condition) to that of the other two conventional techniques—supports the idea that a glove-based form factor is an effective approach for capturing and extracting information from joint sounds.

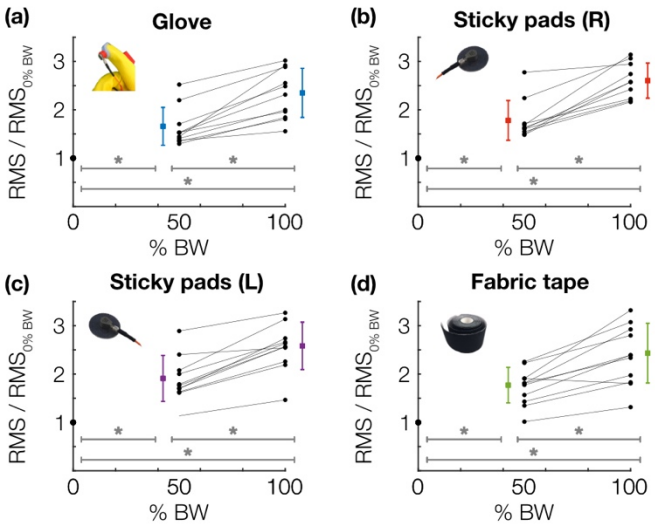

Figure 25. Relative grinding loudness vs. % body weight applied for each mounting technique, including (a) the instrumented glove, (b) adhesive microphone pads mounted on the right leg, (c) adhesive microphone pads mounted on the left leg (for determining comparability between left and right knees), and (d) fabric kinesiology tape. Across 11 subjects, each mounting technique demonstrates the same trend: a monotonic, significant increase in baseline-normalized RMS with increasing vertical load. (*) indicates significance ($p < 0.01$) as determined by paired Student's t-test with Holm–Bonferroni correction.

4.3.2 Repeatability of Glove Versus Conventional Techniques

The central result of repeatability testing is shown in Table 6, which reports the ICC values calculated for each dataset described in Section 4.2.4.1. While there is no standard value for acceptable reliability using ICC, a general rule suggests that values between 0.5 and 0.75 indicate moderate reliability, values between 0.75 and 0.9 indicate good reliability, and values greater than 0.90 indicate excellent reliability [126]. For the glove-only dataset, repeatability analysis yielded ICC values of 0.984 (95% CI of 0.972–0.992) for the acoustic energy feature, 0.947 (95% CI of 0.905–0.975) for acoustic entropy, and 0.954 (95% CI of 0.916–0.977) for median-normalized frequency of the power spectrum (MDF). These results suggest that, in terms of three features commonly used to

describe distinct characteristics of acoustic signals, a glove-based system can acquire consistent and repeatable joint sounds information between FE cycles and across trials. For the tape-only dataset, repeatability analysis yielded ICC values of 0.928 (95% CI of 0.877–0.962) for acoustic energy, 0.735 (95% CI of 0.608–859) for acoustic entropy, and 0.922 (95% CI of 0.867–0.958) for MDF. For the pads-only dataset, repeatability analysis yielded ICC values of 0.937 (95% CI of 0.893–0.967) for acoustic energy, 0.776 (95% CI of 0.608–0.859) for acoustic entropy, and 0.922 (95% CI of 0.867–0.958) for MDF. The results indicate that the level of reliability for pads and tape can be regarded as "good" to "excellent" for acoustic energy and MDF and "moderate" to "good" for acoustic entropy. For the dataset in which all three mounting techniques were included, repeatability analysis yielded ICC values of 0.982 (95% CI of 0.972–0.989) for acoustic energy, 0.836 (95% CI of 0.742–0.903) for acoustic entropy, and 0.976 (95% CI of 0.962–0.986) for MDF. These results demonstrate a high degree of agreement between features derived from each mounting technique, which further suggests that the glove-based system is a reliable alternative to the conventional methods of mounting the acoustic/vibration sensors to skin.

Table 6. Results of repeatability testing using intraclass correlation coefficient (ICC) as an indicator of measurement repeatability and agreement among mounting techniques (*CI = Confidence Interval).

	Glove		Tape		Sticky Pads		Glove, Tape, and Sticky Pads	
	ICC	95% CI*	ICC	95% CI	ICC	95% CI	ICC	95% CI
Acoustic Energy	0.984	0.972 – 0.992	0.928	0.877 – 0.962	0.937	0.893 – 0.967	0.982	0.972 – 0.989
Acoustic Entropy	0.947	0.905 – 0.975	0.735	0.648 – 0.859	0.776	0.672 – 0.871	0.836	0.742 – 0.903
Median Frequency Power	0.954	0.916 – 0.977	0.922	0.867 – 0.958	0.921	0.865 – 0.959	0.976	0.962 – 0.986

4.3.3 Consistent Contact Force Improves Consistency of Results

Figure 26 shows a snippet of two representative trials comparing the effects of consistent versus inconsistent contact force on the joint sound signal captured by a fingertip-mounted accelerometer. Figure 26b depicts how loss of sensor contact (characterized by a rapid decrease in the contact force signal) coincides with regions of the joint sound signal corrupted by signal artifact. Importantly, these signals serve as an example of how the capacitive force sensor can be used to identify unreliable or low-SNR portions of a joint sound recording. Table 7 demonstrates the benefit of consistent contact on the acquired joint sound signal more quantitatively. In this table, values of mean, standard deviation, and coefficient of variation of "grinding loudness" (low-frequency RMS amplitude) are reported for each FE trial and across trials for both test conditions (i.e., consistent and inconsistent force applied at the fingertip). The key takeaway can be found in the last column of the table, in which the variation in grinding loudness across all FE cycles collected with consistent contact (CV = 0.131) can be seen to be, on average, less than 25% that of the trials with inconsistent contact (CV = 0.550). This finding highlights the fact that consistent contact is critical for obtaining reliable results.

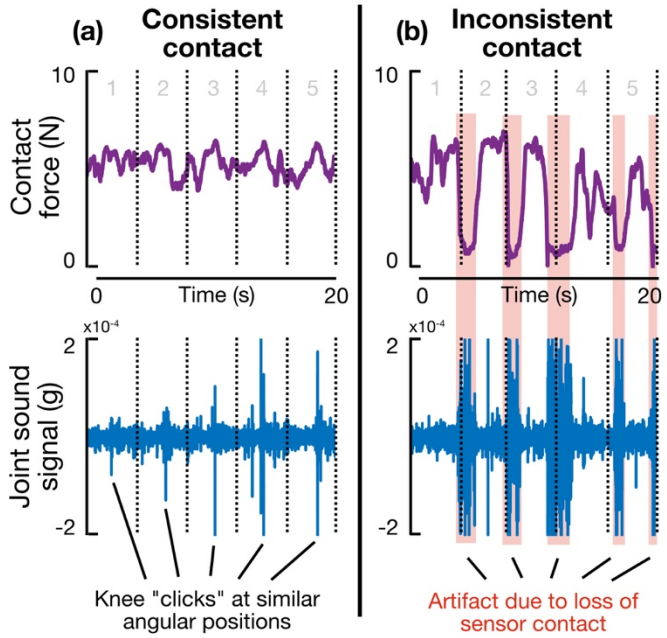

Figure 26. Fingertip contact force and joint sound signal waveforms for representative trials with (a) consistent and (b) inconsistent sensor–skin contact. Time duration of each waveform is 20 s, in which five seated knee flexion–extension cycles were completed at a rate of 4 s per cycle. Highlighted portions illustrate how a rapid decrease in contact force coincides with regions of the joint sound signal dominated by artifact. These data demonstrate that sensor-to-skin contact force can be used as a context clue for rejection of noisy, low-quality joint sound signals.

Table 7. Effects of contact force consistency on repeatability statistics of "grinding loudness" (low-frequency RMS amplitude) feature.

		Within trial (cycle-to-cycle)			Across trials		
		Mean	SD*	CV**	Mean	SD*	CV**
Consistent contact	trial 1	8.98×10^{-3}	7.10×10^{-4}	0.079	1.02×10^{-2}	1.34×10^{-3}	0.131
	trial 2	9.63×10^{-3}	1.56×10^{-3}	0.162			
	trial 3	1.09×10^{-2}	7.64×10^{-4}	0.070			
	trial 4	1.14×10^{-2}	4.13×10^{-4}	0.036			
Inconsistent contact	trial 1	1.93×10^{-2}	5.22×10^{-3}	0.270	3.24×10^{-2}	1.78×10^{-2}	0.550
	trial 2	2.32×10^{-2}	7.07×10^{-3}	0.305			
	trial 3	4.58×10^{-2}	2.15×10^{-2}	0.469			
	trial 4	4.11×10^{-2}	1.73×10^{-2}	0.422			

*SD = Standard Deviation, **CV = Coefficient of Variation

4.3.4 Considerations for a Hand-Worn Acoustic Sensing System

Using a glove-based system to measure joint sounds presents both benefits and challenges. This technique offers better sensor-to-skin contact, given the nervous system's capacity for precise endpoint control, but introduces the possibility of user error. The mechanical sensitivity required to resolve vibrations on the surface of the skin caused by internal motion/friction of the joint makes the job of the glove wearer that much more difficult, for a slight change in fingertip contact with the subject's skin can corrupt the underlying joint sound signal. Thus, contact force feedback and training are important to minimize human error. Other techniques such as tape do not suffer the same limitation, but they have their own. Namely, any approach that uses adhesive has the potential to couple interface sounds—e.g., tape lifting on / off of the skin—into the recording. Furthermore, these artifacts can be difficult to distinguish from the joint sound signal or can bury it entirely. In this way, a glove-based system, coupled with some feedback mechanism and adequate training, presents a major advantage over other, more established techniques. Additionally, a glove-based system eliminates the need for disposables like sticky pads or tape, the use of which may cause discomfort and of which the adhesive may degrade during use, leading to inconsistency in sensor-to-skin contact. Furthermore, the benefit of a glove form factor over a wearable brace with embedded sensors is its versatility of use across joints and across subjects of different sizes / shapes; a brace would require custom fitting—a potentially painstaking task to ensure optimal, consistent contact.

4.4 Conclusion and Future Work

The work reported here—in which we used an experimental framework known to reliably alter healthy knee joint sounds, coupled with a simple metric (low-frequency RMS amplitude) that manifests some changing physical properties of the joint—serves chiefly

as a proof-of-concept validation of our glove-based method of joint sound sensing. Validation was further conducted through repeatability testing, which indicated that our glove-based system was able to produce consistent results, particularly under conditions of consistent fingertip contact force, and a high level of agreement with conventional techniques used to couple vibration sensors to skin. Future efforts should focus on identifying additional metrics for comparing the utility / performance of various form factors and, more importantly, deploying the glove in affected populations (e.g., acute knee injury, arthritis). Inter-user variability should be studied to establish the repeatability of results when different users administer the glove. As mentioned previously, this variability may arise from a host of factors, including accuracy of sensor placement near the targeted anatomical landmark and amount of contact pressure applied. While these are limitations of the current approach, future efforts will focus on evaluating the effects of these variables experimentally. We believe that training (i.e., by a medical professional, user manual, or on-device sensory feedback) and experience will be critical for obtaining reliable results, as is the case with any self-administered medical exam or intervention. We envision that a wearable, hand-worn system, when used in a home setting, could serve not only as an effective tool for capturing arthro-acoustic information but also as an opportunity for an individual to directly partake in the healthcare of a dependent, such as the parent of a child with juvenile idiopathic arthritis. Whatever the technique or application, as the value of a joint-sounds-based approach to joint health assessment is better developed, exploration of different techniques and improvements on existing ones will be critical for obtaining the best possible information and achieving the best possible clinical outcome.

CHAPTER 5. PATROCLUS: NONINVASIVE ASSESSMENT OF ACHILLES TENDON LOAD

5.1 Introduction

Tendons play a key role in the way we move about the world—serving not merely to transmit forces between muscle and bone, but also to amplify the power output of muscle [128], improve the efficiency of the muscle-tendon unit [129], [130], passively stabilize limbs [131], and buffer muscle from damage due to rapid lengthening [132], [133]. The AT experiences the highest mechanical stress of any tendon in the human body [29], [134]–[136] and is one of the most commonly injured tendons [28], [137]–[139]. Rupture of the AT, caused by excessive stress in the tissue, is a debilitating injury that can take months or even years to rehabilitate [140]–[143], with only a slim possibility of a full return to pre-injury performance levels [144]–[146]. Research suggests that proper conditioning of the AT and a better understanding of its loading conditions during normal activities could reduce injury risk and/or accelerate recovery [24], [26], [27]. However, though *in vivo* assessment of tendon loading has been explored using invasive techniques [15], [16], [147]–[149], this task remains difficult to achieve noninvasively, with some proposing the use of elastography [150], laser Doppler vibrometry [151], and shear wave dispersion analysis [152].

More recent work has demonstrated that excitation of the AT by a skin-mounted piezoelectric tapping mechanism can provide insight into the tension state of the tendon by modeling the tendon as a Timoshenko beam and measuring shear wave velocity along it

using a contact accelerometer [153]. In this prior study, the researchers demonstrated that micron-scale taps on the skin superficial to a tendon can propagate into the underlying tendinous tissue, suggesting that excitation of the tendon as a structure can be achieved noninvasively. High correlation between ankle torque—used as a proxy measure of AT force—and the square of shear wave velocity was reported for simple isometric calf exercises in a cohort of six healthy subjects. Representative results presented for walking and running gait also showed favorable trends between wave speed and ankle torque. In particular, the authors observed good temporal alignment between wave speed and torque waveforms and similar increases in peak torque with increasing walking speed. A subsequent study involving 12 healthy subjects walking at various speeds reported group coefficients of determination (R^2) ranging from 0.80 to 0.84 between measured shear wave speed and AT stress estimated by inverse dynamics during the stance phase of gait [154]. While these results are promising and the methodology sound, some limitations do exist, particularly regarding translatability to an affordable, wearable system; in specific, challenges include the need for two accelerometers with a strict placement scheme, a voltage amplifier capable of delivering 150V excitation to a relatively expensive piezoelectric actuator, and subject-specific calibration exercise(s).

We envisioned that these limitations could be addressed by a novel system design, based on a single contact accelerometer to detect propagated vibrations produced by a small, cheap linear resonance actuator (LRA) on the skin superficial to the AT (Figure 27a). The LRA produces burst vibrations—intermittent sinusoidal excitations—which interact with the underlying tissue in a characteristic way based on the mechanical state of the tendon (i.e., its tension, stiffness, and damping) (Figure 27b). Thus, our system, like

that of [153] and [154], measures local accelerations at the skin surface, though our approach differs in terms of how the tissue is mechanically excited and how the measured accelerations are interpreted. As detailed in [153], the authors "tap" the AT and measure the time delay between when the induced shear wave reaches two contact accelerometers in series; the AT is then assumed to behave like a Timoshenko beam, and the shear wave velocity is correlated to the axial force in the tissue, much as conventional elastography techniques relate wave velocity to mechanical properties like shear modulus. By contrast, our approach takes into account the entire transient response of the AT to a burst excitation, with the assumption that the AT responds to this input (i.e., absorbs and dissipates energy) differently based on the loading state of the tissue due to putative changes in the tissue's mechanical properties. By describing the response of the tendon to these excitations at a variety of known loading states, we built a model to assess tendon load noninvasively and potentially in real-time (Figure 27c). Access to such a tool could precipitate novel methods for injury prevention and rehabilitation, athletic training, patient-in-the-loop exoskeleton control, and the study of myriad neuromuscular and musculoskeletal disorders.

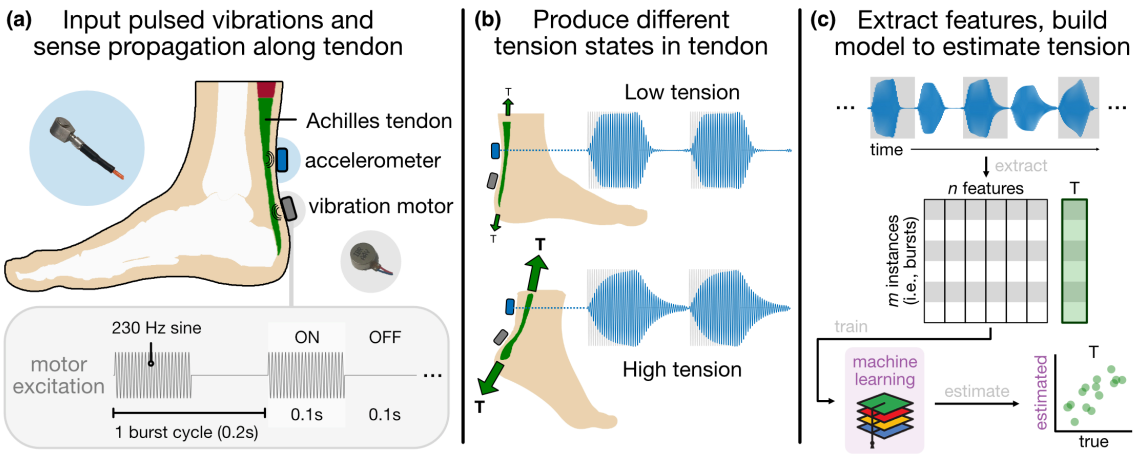

Figure 27. System architecture and approach. (a) A vibration motor and contact accelerometer are placed ~2 cm apart on the skin superficial to the AT. (b) Burst vibrations, the input waveform of which is depicted in the lower left, propagate along the tendon, which responds differently to the excitation based on its tension state. (c) Shape-based features are extracted from each burst response window and used to train a machine learning model for estimating tension in the tendon noninvasively.

In this work, we present results that demonstrate characteristic changes in tendon response as a function of AT tension across a battery of static and dynamic tasks performed by healthy subjects (N = 12). These changes are quantified as shape-based features extracted from accelerometer data, and a collection of these features are used to train a model for estimating a target variable closely related to AT tension (net ankle moment); this estimation model is evaluated on subject walking data to assess its performance. Simulation results from a 2-degree-of-freedom (DOF) mechanical systems analogy of the LRA-tendon unit are used to explain, in approximation, the tendon response observed *in vivo*. Finally, results of a proof-of-concept study (N = 1) using a fully wearable version of the tendon vibration hardware are presented.

5.2 Methods

5.2.1 Study Participants

Twelve able-bodied subjects (8 male / 4 female, age: 25.3 ± 3.4 years, height: 172 ± 8.5 cm, mass: 70 ± 13 kg) participated in this study, which was conducted under approval from the Georgia Institute of Technology Institutional Review Board. Inclusion criteria included no history of major ankle injury.

5.2.2 Hardware and Data Acquisition

5.2.2.1 Tendon Vibration

Tendon loading was assessed by way of a vibration motor-accelerometer pair placed ~2 cm apart from each other on the skin superficial to the AT, midway along the length of the free tendon and on the tendon's midline in the mediolateral dimension (Figure 27a). The motor (i.e., the LRA) was placed distal to the accelerometer and thus proximal to the tendon's insertion at the calcaneus. Both the motor and accelerometer were affixed to the skin using a double-sided adhesive foam pad (23-mm Stickie, Rycote, Gloucestershire, UK) and fabric tape (Kinesio Tex, Kinesio, Albuquerque, NM, USA).

The LRA (G0832012, Jinlong Manufacturing, China), which measures 8 mm in diameter and weighs 2 g, was driven by an AC voltage (amplitude: 3 V, max current: 90 mA) at its resonance frequency of 230 Hz. This 230-Hz sine wave was multiplied with a 5-Hz square wave (duty factor = 50%) to generate a continuous train of burst vibrations, the excitation signal of which was delivered to the motor by a benchtop function generator (33500 Series, Agilent Technologies, Santa Clara, CA, USA) (Figure 28a,b). Intermittence of excitation ("on-off" behavior) was important, as it was observed that rise and fall times changed characteristically with tendon tension (Figure 28c,d). The pulse rate (here, 5 Hz) was the effective data rate, as the loading state of the tendon was assessed once per burst period. The motor's vibration amplitude was on the order of 1.5 g acceleration, and its axis of vibration was oriented orthogonal to the skin. Subjects reported only a mild "buzzing" sensation at the heel upon first application and, after only a few minutes, remarked on having forgotten that the motor was there.

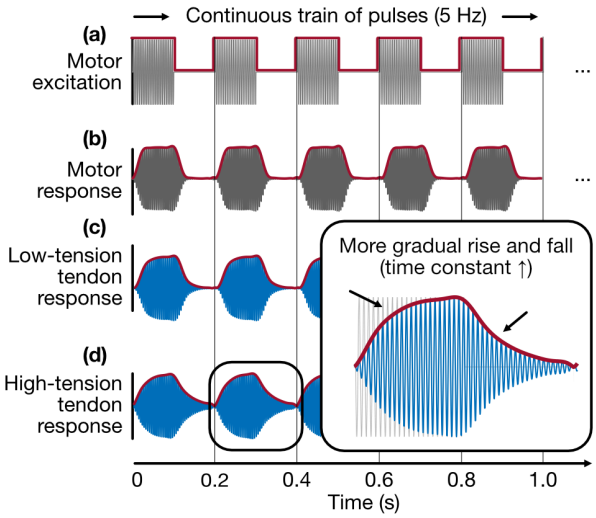

Figure 28. Vibration input and response. (a) A vibration motor is excited by a continuous train of bursts (230-Hz sine multiplied with 5-Hz square). (b) The motor exhibits its own (constant) rise and fall time due to internal stiffness and damping. (c) A tendon under low tension responds to burst vibration with a steeper rising and falling edge (faster energy absorption and dissipation). (d) A tendon under high tension responds to burst vibration with a more gradual rising and falling edge (slower energy absorption and dissipation).

The propagated vibrations were sensed on the skin by a miniature, high-bandwidth, uniaxial accelerometer (series 3225, Dytran Instruments, Inc., Chatsworth, CA, USA) (sensitivity = 100 mV/g, frequency response ± 10% = 2 to 10,000 Hz). The accelerometer was oriented such that it was sensitive to vibrations orthogonal to the skin surface. The accelerometer was connected to a data acquisition unit (USB-4432, National Instruments, Austin, TX, USA)—itself connected to a laptop acquiring the data via MATLAB (MathWorks, Natick, MA, USA)—and was sampled at 25 kHz.

5.2.2.2 Conventional Gait Analysis Instruments

All experiments were conducted in a fully equipped gait analysis lab (Figure 29a). Subjects' lower bodies were instrumented with 16 retroreflective markers whose positions

in space were tracked by a motion capture system (Vicon Motion Systems, Denver, CO, USA) comprised of 34 video cameras (sampling rate = 200 Hz). Arranged according to Vicon's Plug-in-Gait lower body model [51], [155], these markers provided full 3D kinematics of subjects' thigh, shank, and foot segments, and their trajectories were smoothed using a Woltring low-pass filter to remove noise [156]. All trials were performed on a split-belt treadmill instrumented with bilateral force plates (Bertec, Columbus, OH, USA) so as to capture ground reaction forces (GRF) and center of pressure underfoot (sampling rate = 1000 Hz). Using kinematic and kinetic information from the motion capture and force plate systems, joint angles (Figure 29c) and net moments (Figure 29d) at each joint were calculated by way of inverse dynamics [157] using the Plug-in-Gait solver within Vicon's Nexus software package. This tool, which is an implementation of the Conventional Gait Model based on the Newington-Helen Hayes model [158], has been used extensively in gait studies and has been shown to provide reliable and clinically acceptable outputs of joint kinematics and kinetics, particularly in the sagittal plane, on which our analysis is focused [51], [155], [159], [160]. Ankle plantarflexor and dorsiflexor muscle activity—that of the medial and lateral gastrocnemius (MG, LG) and tibialis anterior (TA)—was acquired by three surface electromyography (EMG) sensors (SX230, Biometrics Ltd, Newport, UK) (sampling rate = 1000 Hz) (Figure 29e). These signals were rectified and digitally filtered using a Butterworth filter with a cutoff frequency of 6 Hz.

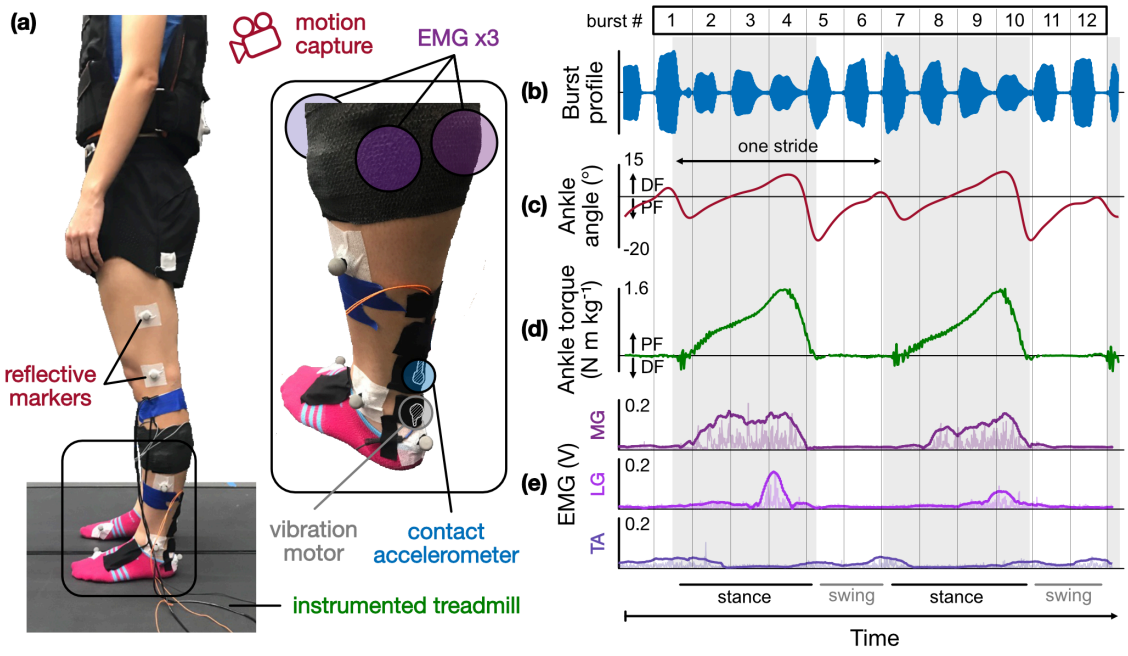

Figure 29. Subject instrumentation and sample biomechanics time series. (a) Each subject is instrumented with the tendon vibration hardware (motor and accelerometer) as well as a suite of sensors used in conventional gait analysis (motion capture, EMG, load cell-instrumented treadmill). (b) During each experiment, burst vibrations are delivered to the AT during any given task; (c) ankle angle (from inverse kinematics), (d) ankle torque (from inverse dynamics), and (e) EMG from the medial and lateral gastrocnemius (MG, LG) and tibialis anterior (TA) are acquired simultaneously.

5.2.3 Experimental Procedure

After being instrumented, subjects were asked to perform a variety of tasks designed to impose a range of loading conditions upon the AT. These tasks included quiet standing (as a baseline), tiptoe standing (both two-legged and one-legged), calf raises at 2 s per cycle (both two-legged and one-legged), level treadmill walking at four speeds (1.0, 1.3, 1.6, and 1.8 m/s), and level treadmill running at three speeds (2.0, 2.3, and 2.6 m/s). To ensure that the burst response phenomena were not simply the result of a change in ankle angle, which might alter the distance between the motor and the accelerometer, or merely skin stretch, a subset of subjects performed a simple isometric calf contraction task

in which the subject placed the foot on the floor in a slightly plantarflexed pose and isometrically contracted the calf muscle periodically, taking care not to change the joint angle or alter GRF. All tasks were performed for 60 s each, during which time data were collected continuously. Subjects were allowed to touch off on a support bar adjacent to the instrumented treadmill to aid in balance, though they were instructed not to bear any significant weight on the bar.

5.2.4 Data Analysis

5.2.4.1 General Analytical Framework

The AT was mechanically stimulated using continuous trains of burst vibrations that propagate along the length of the tendon between a vibration motor (transmitter) and accelerometer (receiver). The accelerometer captured local accelerations of the underlying tissue, though its raw output contains information in frequency bands not relevant to our analyses (e.g., baseline wander caused by coarse limb motion, motion artifact, and interface noise) (Figure 30a). A digital bandpass filter (Kaiser-window finite impulse response filter, bandwidth: 215 to 245 Hz) was applied to mask frequency content outside of a narrow band around the stimulation (carrier) frequency of 230 Hz (Figure 30b).

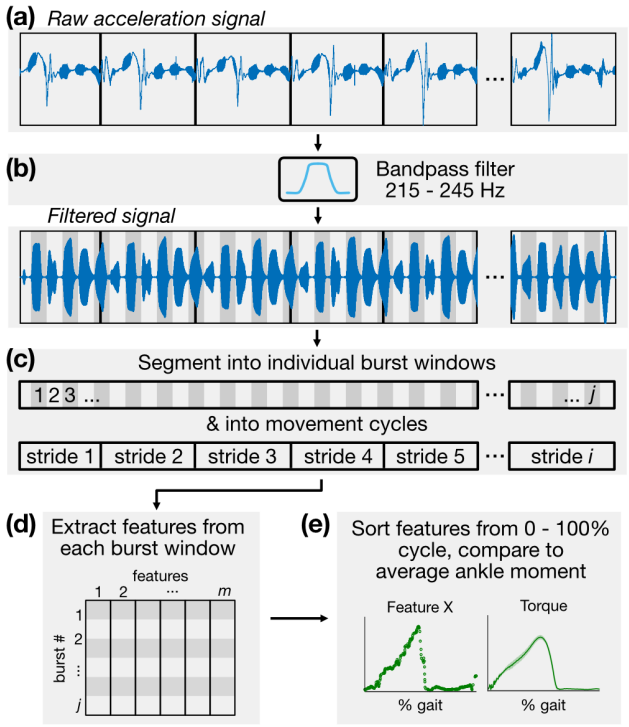

Figure 30. Signal processing and analytical framework. (a) The skin-mounted accelerometer captures not only local vibrations of the skin due to motor excitation but also coarse movement of the limb and other artifact. (b) The raw acceleration signal is bandpass filtered selectively around the motor excitation frequency of 230 Hz. (c) The signal is then segmented into individual burst windows and movement cycles. (d) Features are extracted from each burst window and stored in a feature matrix. (e) Features are plotted against their location in time within each movement cycle so that average behaviors across each cycle can be observed.

The filtered signal was then segmented into individual burst windows, each with a 200-ms period beginning at excitation onset (Figure 30c). For cyclical tasks such as calf raises and walking, the signal was also segmented into individual cycles of motion using GRF from the force plates as a timing reference. The beginning of each gait cycle (heel-strike) was defined as when GRF reached a nominal force threshold (25 N), and the transition to swing phase was signaled by GRF falling below this threshold. With both the onset time of each burst window and each motion cycle period known, the location (% cycle, defined simply as the fraction of the time between successive heel-strikes) of each

burst within, for instance, the gait cycle was established; this was important for plotting variables of interest against % cycle, from which average behaviors can be observed. Individual burst windows were then treated as distinct data instances from which a set of features describing the shape of the response were extracted. The same segmentation process was performed for the time series of ankle torque, EMG, and other biomechanical variables that relate to tendon tension. Information extracted from each burst window—including that of the burst excitation response, torque, and others—was then arrayed in a table in which columns represented features and rows represented data instances (Figure 30d). This table of features was then used to train a machine learning model for estimating tendon loading states, the specifics of which are discussed below (Figure 30e).

5.2.4.2 Predictors: Characterizing Propagated Vibrations

During pilot tests, it was observed that the shape of the tendon response—that is, the envelope of the burst vibration sensed at the accelerometer—changed distinctively in association with tendon tension. Characteristic shape changes included, mostly conspicuously, a more gradual rising and falling edge (increased rise and fall time constants in the analogy to a step response) of the burst envelope as AT tension increased (Figure 28 inset). A collection of 70 features that describe both temporal and amplitude-based attributes of the burst profile (e.g., rise/fall time, peak/median amplitude, other conventional statistics) was constructed (Table 8) and used as predictors (inputs) for estimating a target variable related to AT tension. Candidate features were plotted against target variables to discern which might be suitable predictors.

Table 8. Features extracted from burst envelope.

#	Feature	Description
1-3	*max* (& *_on, _off*)	Maximum amplitude
4-11	*mean* (& *_n, _on*, *_on_n*, *_off, _off_n, _off_on, _off_n_max*)	Mean amplitude
12-19	*med* (& *_n, _on*, *_on_n*, *_off, _off_n, _off_on, _off_n_max*)	Median amplitude
20-27	*auc* (& *_n, _on*, *_on_n*, *_off, _off_n, _off_on, _off_n_max*)	Area under the curve
28-35	*std* (& *_n, _on*, *_on_n*, *_off, _off_n, _off_on, _off_n_max*)	Standard deviation
36-41	*meandiff* (& *_n, _on*, *_on_n*, *_off, _off_n*)	Average slope
42-45	*maxROC* (*_on*, *_on_n*, *_off, _off_n*)	Maximum (absolute) slope
46-51	*sr* (& *_n, _on*, *_on_n*, *_off, _off_n*)	Slew rate (from reference levels 25% to 75% max amplitude)
52-54	*C* (&*_on*, *_off*)	Time index @ 50% total *auc*
55	*tc*	Time constant of exponential decay (slope of logarithmic fit line)
56	*intercept*	y-intercept of logarithmic fit line
57	*i_min_log*	Time index of minimum of logarithmic fit line
58	*log_gof*	Goodness of logarithmic fit line
59	*symm_diff*	Symmetry of burst envelope (folded in half, subtracted)
60	*symm_diff_abs*	Absolute value of residuals of the above
61	*symm_ratio*	Symmetry of burst envelope (folded in half, divided)
62	*symm_pctdiff*	Percent differences of the above
63-68	*MX* (& *_n, _on*, *_on_n*, *_off, _off_n*)	Mobility parameter: ratio of *std(X)* to *std(dX/dt)*
69	*MXX*	2nd mobility parameter: ratio of *std(dX/dt)* to *std(d^2X/dt^2)*
70	*FF*	Form factor: ratio of *MX* to *MXX*

'*_on*' = specific to the "on" burst region; '*_off*' = specific to the "off" burst region; '*_offon*' = ratio of *_off* feature to *_on* feature; '*_n*' = normalized to envelope max; '*_n_max*' = normalized to envelope max^2

5.2.4.3 Output: Inverse Dynamics

Since the purpose of this study is to estimate AT tension noninvasively, the ideal target (output) variable would be a direct measurement of tendon force / stress. However, ground-truth measurements—though theoretically possible through the use of implantable strain gauges, tendon buckles, or optical fibers [16]—are unfeasible for this study as they would require a sensor to be implanted in the body and affixed directly to the tendon. Therefore, we relied on proxy measures that are closely related to AT tension: net ankle joint moment and sum of calf EMG magnitude. The former can be calculated using inverse dynamics, given that limb kinematics (from motion capture) and endpoint kinetics (GRF from force plates) are known. Assuming minimal co-contraction of the ankle dorsiflexors, which is cromulent in the case of simple isometric exercises [161], [162] and during much of the stance phase of walking [163], [164], net ankle torque can be attributed predominantly to forces developed in the triceps surae, which are borne by the AT [165]. Therefore, ankle moment and AT tension are related by the moment arm distance between the tendon line-of-action and the joint center, which for our purposes is assumed constant, though this distance has been shown to change up by ~10% between heel-strike and push-off [166]. Thus, ankle torque derived from inverse dynamics was used as a target variable (ground truth) to estimate in the case of tasks with minimal co-contraction, including the stance phase of walking and running. During the swing phase of these tasks, joint torques are small due to the absence of GRF, and the assumption that net ankle torque is primarily attributable to forces in the calf is invalid, as activation of the ankle dorsiflexors is necessary to support the weight of the foot. For these reasons, net ankle torque was treated as the target variable only during stance. Non-negligible co-contraction was observed for

certain tasks such as calf raises, likely because subjects required higher joint impedance to stabilize the limb and keep from falling. In these scenarios, sum of calf EMG (i.e., that of MG and LG) was treated as the target variable.

5.2.4.4 Estimator: Regression Model

While a single feature extracted from the burst profile may bear a resemblance to the target variable, it was assumed that a fusion of multiple features would improve estimation performance by better accounting for complex relationships between variables and variation between subjects. To that end, we used sensor fusion paired with machine learning (ML) techniques to estimate AT loading during walking. The input to these ML models was the collection of 70 features (see above) extracted from 6770 burst windows during the stance phase of walking across all 12 subjects. Features were normalized to zero mean and unity variance to account for incongruous scaling between them. The output (label) was an 6770x1 vector containing the corresponding ankle torque at each burst instance. No bursts from swing phase (60 – 100 % gait) were used due to the presence of TA activity violating the assumption that net ankle moment was primarily associated with calf forces, as described above.

We trained regression models using a set of ML algorithms—including simple linear regression, regression trees, support vector machines with various kernel functions—on the feature table(s) described above and selected the candidate model that minimized root-mean-squared-error (RMSE) of a 10-fold cross-validation. By this selection criterion, an ensemble technique known as a bootstrap-aggregation (“bagging”) of regression trees [167] was chosen as the model type. Being an ensemble learner, this technique is inherently

robust to overfitting [73]. Hyperparameters were similarly tuned by minimizing RMSE of a 10-fold cross-validation, whereby the final model was structured as a bag of 50 weak learners (trees), each with a minimum leaf size of 6 (no pruning nor early stopping was used). This eventual model was then evaluated on the 12-subject walking dataset using leave-one-subject-out cross-validation (LOSO-CV), in which 11 subjects' data were used to train the model, while one subject's data were left out as a test set; in this way, the model is presented with unseen data recurrently, simulating the inclusion of new subjects. This train-test split was performed in a round-robin manner such that all subjects' data were tested upon once, and the estimation performance on each subject was averaged and expressed in terms of group R^2 and RMSE.

5.2.4.5 Mechanical System Analogy

To supplement the more black-box, ML-based approach and develop a more mechanistic, intuitive understanding of why the AT's response to burst excitation is modulated as we observed, we sought to model the motor-tendon structure as a mechanical system. As such, this simplified model was used as a framework to examine the effects of putative physiological changes in the tissue on a simulated burst excitation response. The system was approximated as a 2-degree of freedom (DOF), lumped parameter model with two mass-spring-dampers in series: one representing the vibration motor and the other representing the tendon to which it is attached. A schematic of the equivalent 2-DOF system is shown in Figure 31. The equation of motion (EOM) for such a system can be written as

$$m_T\ddot{x_T} + c_T\dot{x_T} - c_M(\dot{x_M} + \dot{x_T}) + k_T x_T - k_M(x_M - x_T) = 0 \quad (6)$$

$$m_M\ddot{x_M} + c_M(\dot{x_M} + \dot{x_T}) + k_M(x_M - x_T) = F(t) \quad (7)$$

where, m is mass, c is damping coefficient, k is stiffness, $F(t)$ is the external force applied by the motor, and subscripts T and M represent the tendon and motor, respectively.

Approximating the AT as a Euler-Bernoulli beam, the transverse vibration EOM is given as

$$\frac{\partial^2}{\partial x^2}\left(EI\frac{\partial^2 w}{\partial x^2}\right) - \frac{\partial}{\partial x}\left(T\frac{\partial w}{\partial x}\right) + \rho A\frac{\partial^2 w}{\partial t^2} = f(x,t) \quad (8)$$

where, E is the modulus of elasticity, I is the second moment of area, w is the transverse displacement of the beam at location x, T is the external axial load, ρ is the density, A is the cross-sectional area, and $f(x,t)$ is the external transverse force. Comparing Equation 8 to a single DOF system EOM ($m\frac{\partial^2 w}{\partial t^2} + c\frac{\partial w}{\partial t} + kw = f(x,t)$), the stiffness term, k_T, can be assumed to be proportional to the tendon tension (i.e., axial load). On the other hand, the tendon is a damping tissue that prevents damage to the muscles by dissipating a portion of the exerted forces [168]. It is shown that, as axial load increases, the damping ratio in a tendon unit decreases [169]. This can be due to the progressive extrusion of water from the tendon that potentially decreases the tissue's viscoelastic damping [170], [171]. Thus, it can be assumed that the damping coefficient, c_T, is inversely proportional to the tendon tension, T. The equivalent stiffness and damping of the motor are determined experimentally by using a square excitation signal and measuring the transient free

oscillation of the motor. The equivalent mass, stiffness, and damping of the tendon are then estimated heuristically to match the envelopes obtained from experimental tests.

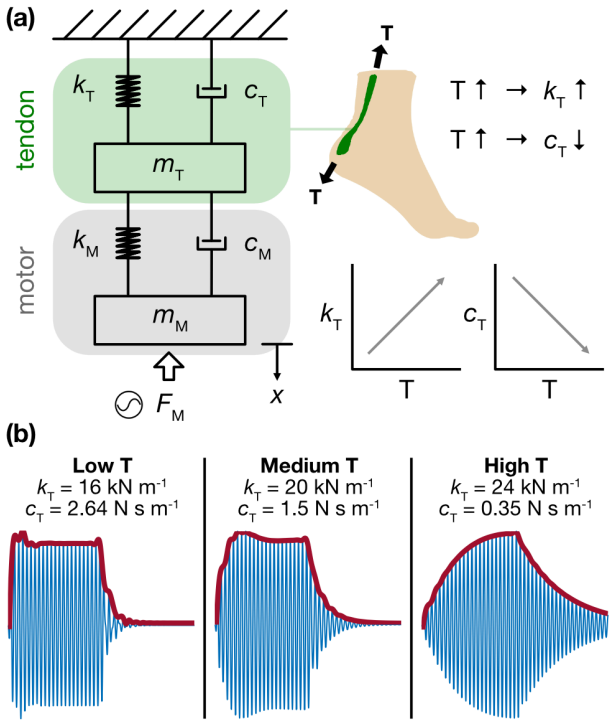

Figure 31. Simplified mechanical model of the LRA-tendon system. (a) The system is modeled as two mass-spring-dampers in series (2-DOF, lumped parameter) with motor excitation modeled as a sinusoidal input force. Based on observation and physiology, we assume that the tendon stiffness, *k*, is directly related to AT tension, *T*, and that tendon damping, *c*, is inversely related to *T*. (b) When the model simulates a low *T* (thus, low *k* and high *c*) state, the burst envelope exhibits a steep rise and fall; under midrange *T* (medium *k* and *c*), the rising and falling edges begin to take on a more gradual progression, as energy is stored and released more slowly; under high *T* (high *k* and low *c*), this behavior is even more pronounced. These results closely resemble the burst responses observed *in vivo*.

5.2.5 A Fully Wearable System: Proof-of-Concept

All data previously reported in this manuscript were produced using a system that could not be considered truly wearable, as the accelerometer was tethered to a USB DAQ and laptop, and the motor was driven by a benchtop function generator. To maximize the

utility of our approach, translation to an untethered system for use in activities of daily life is necessary. Thus, as a proof of concept, we developed a wearable, miniaturized system that replicated our experimental setup, giving us the ability to deliver excitation, capture the tendon response, and log data locally and independently of benchtop equipment (Figure 32).

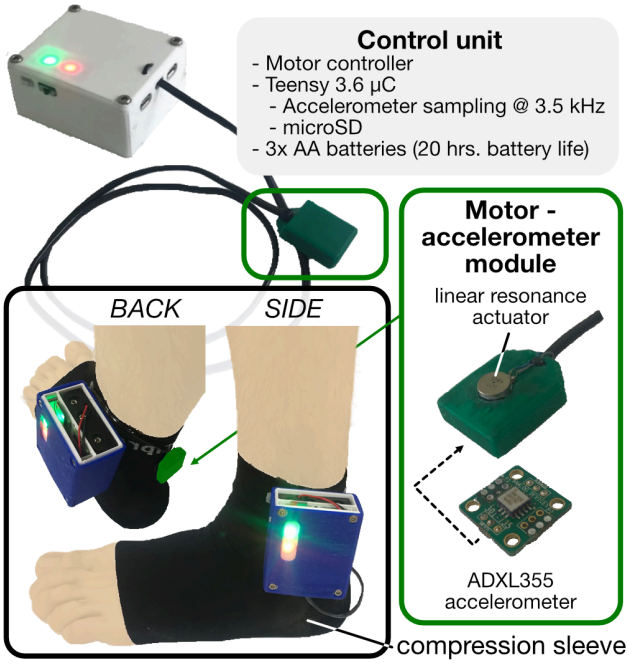

Figure 32. Fully wearable tendon vibration system. A battery-powered unit containing two microcontrollers—one for driving the LRA, the other for sampling and saving the accelerometer—is mounted on a compression sock. A single module housing the LRA and accelerometer is wired to the control unit, positioned on the skin above the AT, and held in place by the compression sock (pictured here outside the sock for better visualization).

The architecture of the wearable can be divided into actuation and sensing modalities. A microcontroller (Teensy 3.6, PRJC, Sherwood, OR, USA) generates the same excitation pattern used in the experimental setup (i.e., 230-Hz sine wave multiplied with a 5-Hz square wave). This waveform is then multiplied by a 7-kHz carrier wave, ultimately

producing a pulse width-modulated (PWM) waveform. The PWM output then directly drives the same LRA as used above, which acts as an analog filter, effectively removing the 7-kHz PWM base frequency and vibrating at the same 230-Hz carrier, 5-Hz pulse train as above. A separate microcontroller interfaces with a digital MEMS accelerometer (full scale range = ±2 g, bandwidth = 1 to 1000 Hz) (ADXL355, Analog Devices, Norwood, MA, USA), sampling local skin acceleration over SPI at 20-bit resolution and at a sampling rate of 3.5 kHz. A custom control unit contains the batteries and the microcontrollers and is affixed to the lateral side of a compression sock. The LRA and accelerometer are packaged in a single, custom-designed module that is wired to the control unit and placed at a desired location along the Achilles tendon underneath the compression sock, creating a non-invasive and minimally obtrusive wearable system. Depressing a pushbutton on the control unit initiates excitation of the motor and sampling of the accelerometer, the output of which is written to an onboard SD card. Currently, 3 AA batteries power the device, which draws approximately 300mA during operation, yielding a battery life of roughly 20 hours, assuming continuous use.

The performance of the wearable was characterized in a proof-of-concept study (N=1) by conducting several of the same static and dynamic tasks: neutral standing, double- and single-limb tiptoe standing, and treadmill walking at 1.0 m/s.

5.3 Results and Discussion

5.3.1 Representative Subject: Static and Isometric Tasks

Static tasks (baseline standing, 2-legged tiptoe, and 1-legged tiptoe) were performed to determine how burst responses changed at different levels of AT tension in

the absence of joint motion. AT tension was nominal in the case of a neutral posture with no calf activation, with passive stretch of the tendon and small muscle activations to counteract sway making it non-negligible. By contrast, tiptoe standing produced high tension states in the tendon due to the contraction of the triceps surae pulling on the AT—with the 1-legged case demanding substantially more calf activity than the 2-legged case to support full body weight on a single limb.

Results from a representative subject, in which a candidate feature describing a burst profile attribute is plotted against the net ankle torque, demonstrate how each task stratifies AT force and produces a distinct change in the burst response (Figure 33a). The candidate feature, *med_off_n*, is defined as the median value of the "off" portion of the burst envelope (i.e., the free vibration stage when excitation is removed) normalized to the burst window's maximum amplitude, whose units are immaterial. This feature reflects changes in the falling edge of the envelope and manifests physical changes in the tendon (i.e., the fact that the tendon is tauter and less damped) that allow the LRA-tendon system to "ring" for longer after forced excitation has ceased. This same candidate feature is used in Figure 33, Figure 34, and Figure 41, as, for the majority of subjects, it demonstrated strong correlation with target variables (e.g., group $R^2 = 0.77$ when comparing with ankle torque during walking). The relationship between *med_off_n* and net ankle moment appears more logarithmic than linear, suggesting that changes in the burst's falling edge begin to saturate once the tendon is sufficiently taut. Regardless, good separation is achieved between the three tension states. On average, net ankle torque increased from 0.28 to 0.45 N m kg^{-1} (62.8% increase) between neutral standing and two-legged tiptoe, and from 0.45 to 1.03 N m kg^{-1} (128% increase) between two-legged tiptoe and 1-legged

tiptoe; for these same transitions, the value of *med_off_n* increased from 0.1 to 0.25 (150% increase) and 0.25 to 0.34 (35% increase), respectively.

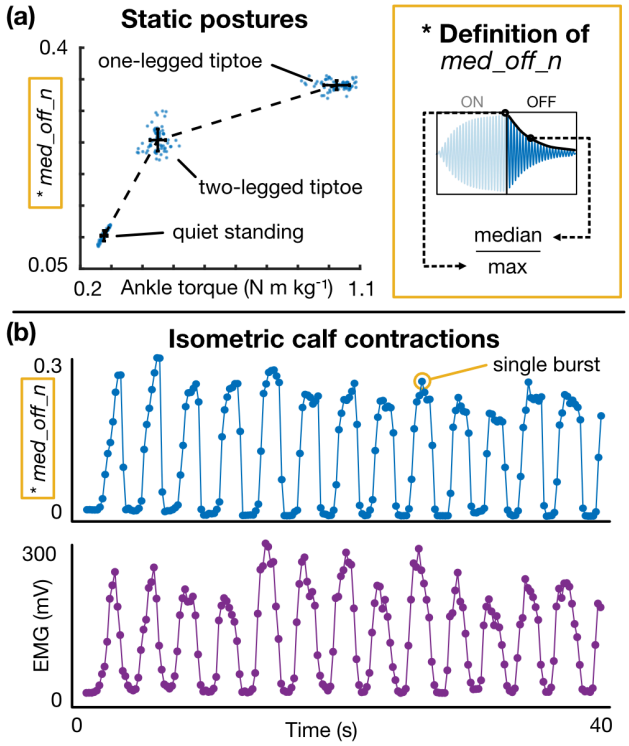

Figure 33. Static calf exercises: representative results. (a) A candidate feature (*med_off_n*) demonstrates how the burst response changes in response to a change in AT tension. Both *med_off_n* (y-axis) and net ankle torque (x-axis) increase as the subject switches from neutral standing (left cluster) to 2-legged tiptoe (middle cluster) to 1-legged tiptoe (right cluster). Each dot represents a single burst, and the error bars represent the standard deviation of each set of points. (b) *med_off_n* (top) and calf EMG (bottom) plotted against time for an isometric calf contraction task. These plots demonstrate that the tendon response changes regardless of joint angle or skin stretch.

Results from the same representative subject performing the cyclic isometric calf contraction exercise over a 40-s interval are shown in Figure 33b, in which the value of *med_off_n* and calf muscle activation levels for each burst are plotted in parallel. EMG was chosen as the target variable here because, in asking subjects to maintain a constant ankle angle, significant co-contraction was observed, and thus inverse dynamics-derived joint

torque did not provide a valid estimate AT loading. These results indicate that, even at a constant joint angle, the burst profile evolves in response to changing AT tension. Further, this task demonstrates that our technique can still provide an estimate of AT load even in the presence of co-contraction, which is a limitation of the conventional inverse dynamics approach.

5.3.2 Representative Subject: Dynamic Tasks

Though static postures and isometric tasks demonstrated encouraging results, we wanted to judge the true merit of our approach in the context of everyday tasks that involved motion. These tasks included calf raises under both double- and single-limb support, walking, and running. Variation in walking and running speeds was introduced to determine if trends in peak ankle moment, which increases with increasing speed, were able to be observed using the tendon vibration approach. Similar to Figure 33, results from a single, representative subject are illustrated in Figure 34, though similar behaviors were observed across subjects. Likewise, the feature *med_off_n*, extracted from each burst window, is plotted in parallel with the ensemble average of ankle torque (in the case of walking and running) and calf EMG (in the case of calf raises). As before, units for the y-axis values in the top row of plots are irrelevant as they merely describe an aspect of the shape of the burst envelope. Data were taken from 60-s trials for each exercise, so in the case of walking, the average torque waveforms represent the mean behavior across ~60 strides each, and the candidate feature plot superimposes the feature value of every burst in the minute-long trial (represented by each circular marker) against the percent of the gait cycle, which begins at heel-strike. The plots for running can be interpreted much the same,

as can those for calf raise, though in the latter case, the movement cycle begins when the subject is at the apex of the calf raise cycle (i.e., on the tiptoes).

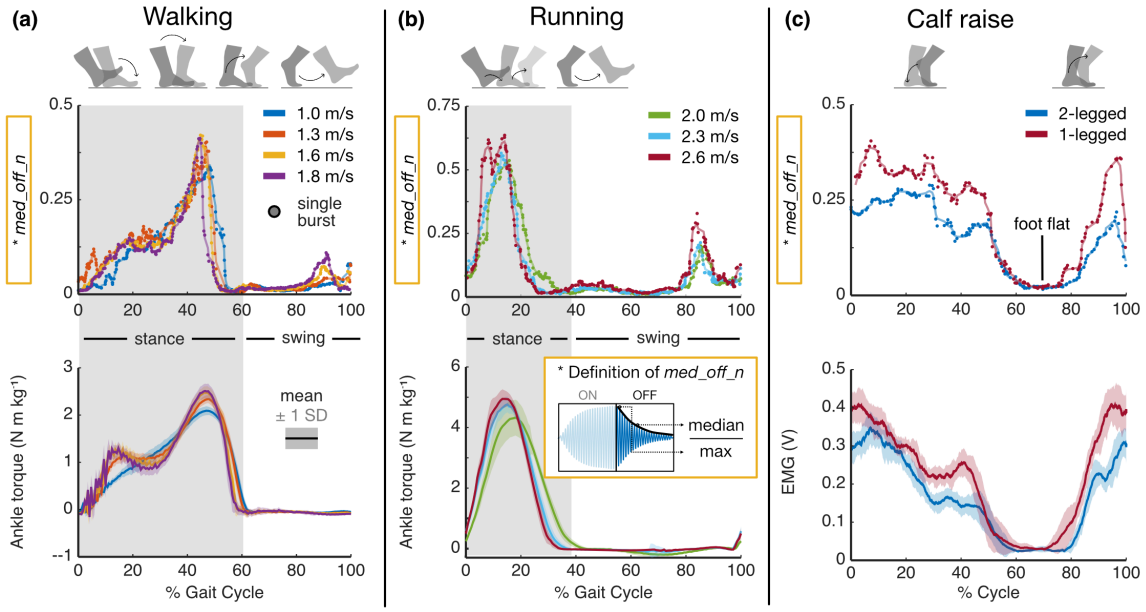

Figure 34. Dynamic exercises: representative results. (a) Burst response feature (top) and average ankle torque (bottom) against % cycle for a range of walking speeds. Each dot represents a single burst's extracted feature. Note the strong temporal alignment, similar shape, and shared trend in peak values with increasing speed, suggesting that the burst response reflects changes in AT tension. (b) Same analysis and interpretation as before, though for running at a range of speeds. (c) Burst response feature (top) and average calf muscle activity (bottom) against % cycle for both 2-legged and 1-legged calf raises.

Figure 34a illustrates how even a single descriptor of the burst response (again, *med_off_n*) can closely track the shape of the ankle torque waveform during walking. Namely, the curves are squarely aligned in time, and even the modest increases in peak torque with increasing speed are evident in the burst feature (40 – 50 % gait). Furthermore, even finer details are reflected in the extracted feature plot: e.g., for the slowest walking speed (1.0 m/s), the torque curve increases monotonically during stance (0 – 60 % gait), while for higher speeds, the curve inflects during midstance (~15 – 30 % gait). Because the

foot is no longer in contact with the force plate during swing (60 – 100 % gait), GRF is zero, and thus, inverse dynamics estimates low values of net ankle moment. The tendon vibration system continues to acquire information about the state of the AT throughout swing, which presents an advantage over the current standard of gait analysis techniques. Since our assumptions about AT tension's relationship to net ankle torque break down during swing, it is difficult to judge the validity of our measurements during this phase of gait; however, experiments in which fiber optic cables are inserted into the AT [148] demonstrate similar trends to what we report here, as does the work done using the piezo-tapper / wave speed approach [153], [154]. The sudden rise in the burst feature waveform toward the end of swing (~ 90 % gait) is noteworthy, as it suggests that the AT is stretched either passively by momentum carrying the foot upward like a pendulum or actively by contraction of the calf muscle, perhaps to return the ankle to a suitable position and stabilize the joint prior to heel-strike to minimize energy loss due to collision [110].

Figure 34b further demonstrates that the tendon vibration approach is capable of tracking AT tension states during an even more dynamic and high-energy task: running. Again, the shape of each candidate feature curve maps remarkably closely onto that of the net ankle torque curve, and both the peak feature values and the peak torques increase with running speed. For this particular subject, a "divot" is present in the peak of the burst feature waveform (~10 – 15 % gait) at the fastest running speed (2.6 m/s), which we attribute to motion artifact becoming more prevalent at faster speeds, or degradation in the adhesive holding the motor / accelerometer on the skin due to sweat, thus making the accelerometer more susceptible to motion artifact under high impact events such as during fast running. Temporal alignment remains precise, evidenced by the fact that the curves'

peaks occur in sequence, and the falling edges during stance (20 – 40 % gait) persist longer for slower running speeds. Again, a slight prominence in the feature value curve is evident in late swing, which we attribute to the same phenomenon as in walking.

Figure 34b compares the same candidate feature for the same representative subject to the ensemble average of calf EMG, which was used as a proxy for AT tension instead of net torque due to non-negligible co-contraction of the antagonist muscle (TA) during the exercise. Notably, the shapes of both sets of curves correspond favorably, as do the amplitude ratios between the 2-legged and 1-legged task.

Group correlations (i.e., across-subjects calculations of R^2) between individual features and corresponding target variables for each movement task are demonstrated in Figure 35, Figure 36, and Figure 37.

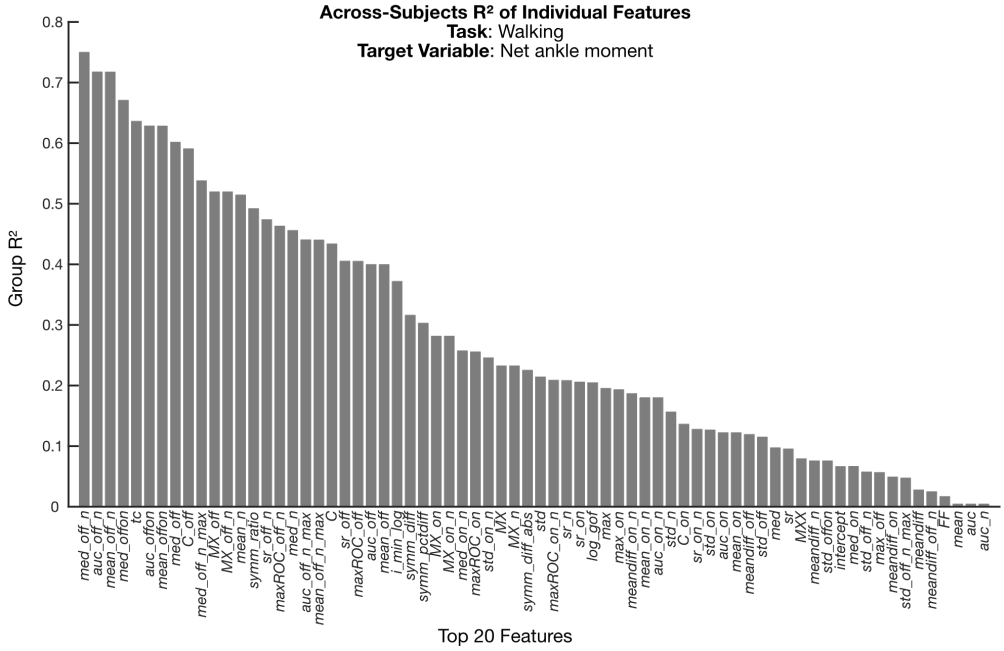

Figure 35. Across-subjects correlations between individual features and target variable (net ankle moment during stance phase) for the treadmill walking task.

Features from all subjects are concatenated into a single matrix, R^2 values for each feature are calculated from simple linear regression, and the top 20 features are reported in order of descending R^2.

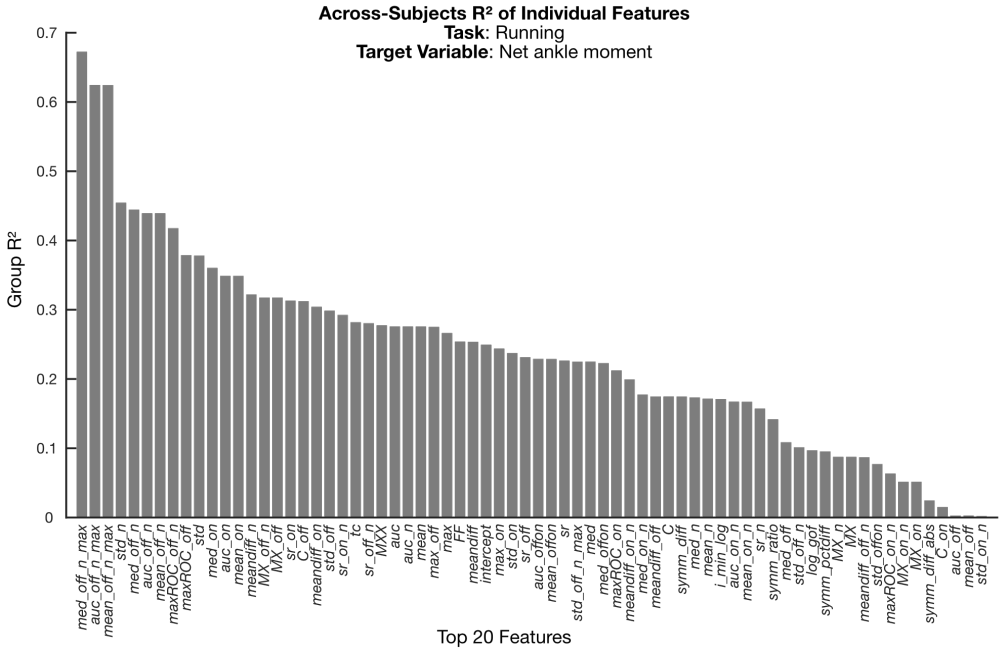

Figure 36. Across-subjects correlations between individual features and target variable (net ankle moment during stance phase) for the treadmill running task. Correlations are calculated and reported as in Figure 35.

Figure 37. Across-subjects correlations between individual features and target variable (sum of calf EMG) for the calf raise task. Correlations are calculated and reported as in Figure 35. Correlations appear low particularly in the calf raise task, as the target variable (EMG) is often noisy and exhibits high subject-to-subject variability. Linear correlation also potentially discounts strong nonlinear relationships between certain features and the target variable.

5.3.3 Estimation of Net Ankle Moment During Walking and Running

The results of Figure 33 and Figure 34 demonstrate that even a single feature extracted from the burst envelope of a vibrated AT can closely track a proxy variable for AT tension—in the case of walking, net ankle moment—both in time and in amplitude. However, while this candidate feature appeared to be strongly linearly related to ankle torque for a number of subjects, its relationship was more complex for others. Therefore, by fusing a number of different features together, we hypothesized that we could build a more effective, robust model that could generalize across subjects, requiring the use of machine learning techniques.

Figure 38a illustrates the result of this regression model-based estimation of ankle torque, with an across-subjects R^2 of 0.85 ± 0.05 and RMSE of 0.34 ± 0.11 N m kg^{-1}. R^2 values for individual subjects are shown in Figure 38b, from which it is evident that the model performed consistently well across subjects. The group RMSE reported here is less than 25% of the typical ankle torque range at these walking speeds and is comparable to the estimation errors reported using the shear wave velocity technique, as is the across-subjects R^2 reported [154]. When body-weight-added walking trials (e.g., those in which subjects wore a 40-lb weighted vest) were included, features were averaged over three steps to reduce noise, and poor trials were rejected (e.g., due to motion artifact or noisy force plate measurements), group R^2 increased to 0.90 ± 0.05, and RMSE decreased to 0.32 ±

0.08 N m kg^{-1} (Figure 39). (Note that, for this set of data, Subject #9 was removed from the model due to high measurement noise in the body-weight-added trials.) Similar model-based estimates of net ankle moment during running ($R^2 = 0.82$) can be found in Figure 40.

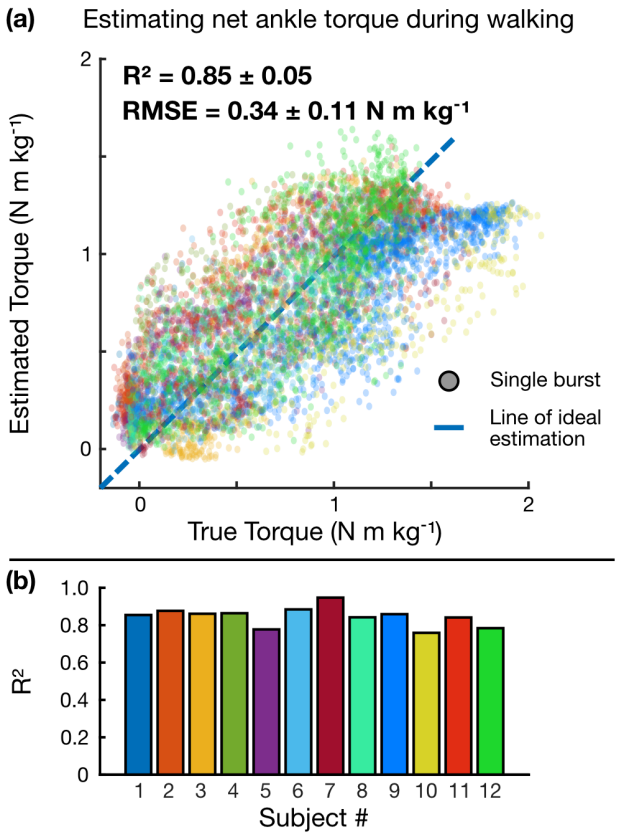

Figure 38. ML-based regression model for estimating ankle torque during walking. (a) Bagged regression tree model estimate of ankle torque vs. ankle torque calculated by inverse dynamics. Each dot represents a single burst, and each color represents a different subject. (b) Individual R^2 values for each subject, demonstrating consistent estimation performance across subjects.

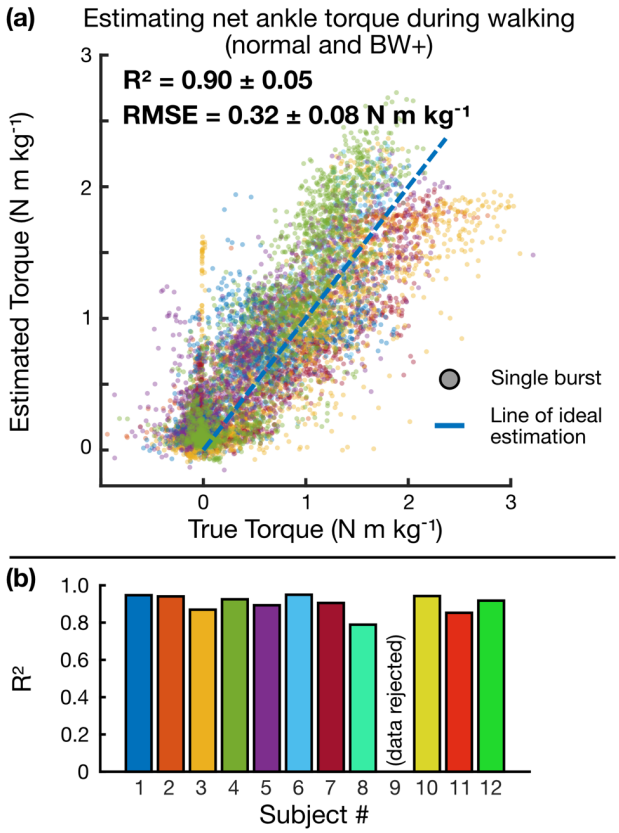

Figure 39. ML-based regression model for estimating ankle torque during walking, including normal body weight and body-weight-added trials. Inputs used in this model, as opposed to that of Figure 38, were averaged over three steps to remove noise, and trials with poor signal quality were rejected. (a) Bagged regression tree model estimate of ankle torque vs. ankle torque calculated by inverse dynamics. Each dot represents a single burst, and each color represents a different subject. (b) Individual R^2 values for each subject, demonstrating consistent estimation performance across subjects, with the exception of Subject #9, whose added-weight walking trials exhibited unusually high motion artifact.

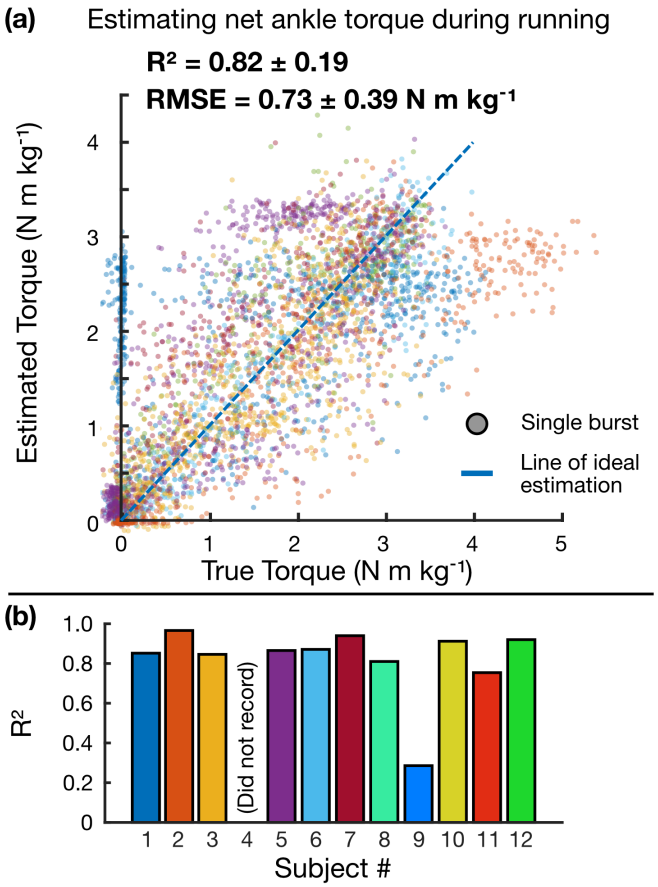

Figure 40. ML-based regression model for estimating ankle torque during running. (a) Bagged regression tree model estimate of ankle torque vs. ankle torque calculated by inverse dynamics. Each dot represents a single burst, and each color represents a different subject. (b) Individual R^2 values for each subject, demonstrating consistent estimation performance across subjects, with the exception of Subject #9 (whose accelerometer signals demonstrated unusually large motion artifacts) and Subject #4 (who lost a pelvis marker for motion capture during the first running trial, rendering inverse dynamics-based calculations of ankle moment challenging due to incomplete kinematic information).

These results serve as a compelling corollary to the major findings of CHAPTER 3, which are illustrated in Figure 19. The result depicted in Figure 19—in which we demonstrated that information from one on-device sensor (the accessible and easy-to-integrate optical encoder) can be used to estimate that of another on-device sensor (the expensive, bulky, and difficult-to-integrate reaction torque sensor)—was viewed as having

potentially limited scientific value, since it did not *explicitly* reveal an intrinsic biological state. The findings shown in the figures above represent an acknowledgment of and concerted effort to address this limitation, as we have demonstrated that we can use information from an accessible, wearable sensor (the accelerometer) to reveal a more difficult-to-measure, underlying biological state (biological ankle moment, and, by association, Achilles tendon tension)—and that we can do so with comparable estimation performance to the more "straightforward" problem of Section 3.3.

5.3.4 2-DOF Mechanical Model Simulation

Estimated mechanical properties of the tendon and motor are substituted into Equations (6) and (7) to qualitatively investigate the overall response of tendon-motor unit to a burst excitation for various quantities of tendon tension. By increasing the tendon axial load, the stiffness coefficient, k_T, increases, while the damping coefficient, c_T, decreases (Figure 31a). For reference, three arbitrary selected cases are shown in Figure 31b, in which the change in the calculated acceleration envelope is illustrated for three different tension levels. The obtained envelopes from the analytical model can be compared to those collected experimentally (e.g., Figure 28c,d) for low- to high-tension states. It is necessary to note that the 2-DOF model is utilized to show the potential of quantitative assessment of the tendon tension using analytical models and to gain an understanding of the physics of the tendon-motor system. Future research including measures of tendon dimensional and material properties can lead to a more realistic model capable of predicting the exact quantities of tendon tension at different states.

5.3.5 Proof-of-Concept Wearable Results

Data acquired by the fully wearable system (Figure 32) are reported in Figure 41. For the sake of continuity, the same candidate feature reported above (*med_off_n*) is used to express these results. Importantly, similar changes in burst response observed in the above experiments (in particular, changes in rise and fall time constant) were preserved in the wearable setup, as shown in the sample waveforms in Figure 41a. In general, the signals appeared less "clean" than those obtained by the benchtop equipment, which we attribute to the microcontroller-derived excitation signal being sampled at a lower rate than was achieved with the benchtop function generator, as well as the digital accelerometer being more susceptible to artifact such as cable motion than its higher-sensitivity and -bandwidth counterpart used above. For the static trials, features of interest (particularly *med_off_n*, as shown) repeatably showed distinct separation between low (standing neutral), medium (2-legged tiptoe), and high (1-legged tiptoe) tension states, consistent with previous experimental results (Figure 41b). Notably, the trend observed during walking was also maintained in the wearable system, with the shape of the *med_off_n* curve resembling that of a classical ankle torque curve across gait both in time and amplitude (Figure 41c). While these results with the wearable system are only preliminary, they evince a similar ability to capture tension states of the AT during both static and dynamic tasks, which holds promise for future experiments outside the laboratory or clinic.

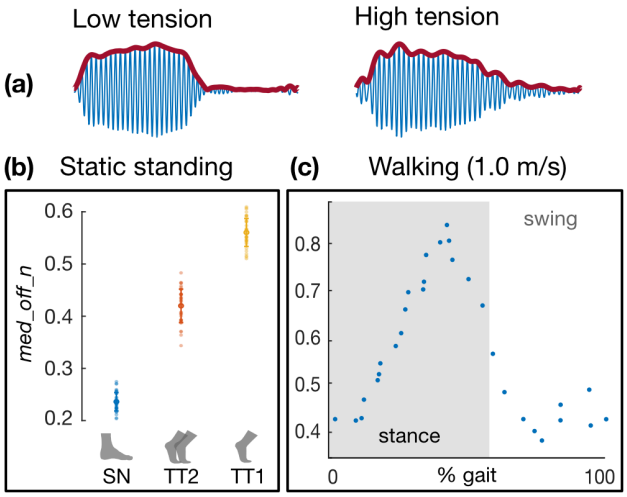

Figure 41. Wearable system: proof-of-concept results. (a) Sample acceleration data from the wearable system demonstrate similar trends in burst response as captured by benchtop equipment. (b) The candidate feature *med_off_n* again shows separation between low ("SN" = standing neutral), medium ("TT2" = 2-legged tiptoe), and high ("TT1" = 1-legged tiptoe) tension states during static exercises, much as in Figure 33a. (c) The candidate feature also resembles the classical ankle torque waveform during walking, much as in Figure 34a.

5.4 Limitations and Future Work

Though these preliminary findings are promising, room for improvement remains in the development of the device hardware, analysis techniques, and model system. In developing a more sophisticated mechanical model, we will gain a greater intuition and understanding of the phenomena observed in the burst response profile and how they relate to mechanical parameters of interest (tendon tension, stiffness, damping, etc.). In turn, these insights will enable us to extract more meaningful, accurate information from the data and perhaps extrapolate to new loading states.

Because our system uses a sensitive accelerometer coupled imperfectly to the skin, it was often susceptible to motion artifact, particularly during high-velocity, high-impact events such as heel-strike. Efforts to address this challenge include improvements in signal

processing (e.g., rejection of signal portions heavily corrupted by artifact, development of a signal quality index for establishing data fidelity) and in hardware (e.g., ensuring better, more consistent sensor-to-skin contact).

In its present form, the effective data rate of our system is 5 Hz, which may suffice for certain applications, but to generate a faithful representation of AT tension across, say, the running cycle, a higher sampling rate will be required. Currently, this limitation is a consequence of the LRA; being a mass-spring-damper system itself, the motor exhibits a characteristic (constant) rise and fall time. Preliminary tests suggested that, when the motor was driven at a pulse rate greater than 10 Hz (at 50% duty), the oscillating mass was unable to return to a neutral position before the onset of the following excitation. This behavior caused the shape of the burst profile to saturate, at which point no additional information contained in the rising and falling edges of the envelope—which normally would evidence a change in tendon tension–was gained. Different excitation patterns—for instance, one with a lower duty factor, such that the free vibration stage (the "off" portion of the burst window) is maintained even at higher pulse rates—and other mechanical stimuli (e.g., an LRA with higher resonance / lower rise time, an actuator with higher bandwidth) may be explored.

Though general trends were observed, burst response did not vary with AT tension precisely the same across subjects. For example, changes in fall time constant might reach an asymptote at a lower tension state for one subject than for another. We attribute such inconsistencies to variation in subject anatomy and physiology (e.g., the tendon's basal tension, modulus, length, and cross-sectional area, thickness of skin / fat / other

surrounding soft tissues, body mass, pre-experiment activity level). Subject-specific calibration may help account for these variations and improve estimation performance.

In this study we use net ankle moment, which is accessible through conventional gait analysis techniques and has previously been treated as a reasonable analog for AT force under certain conditions, as a bridge to relate our directly measured state (surface accelerometry) to our desired state (AT load). Indeed, the use of net ankle moment as a proxy for AT tension is a limitation in itself; more sophisticated approaches could be taken—for instance, a full musculoskeletal model (in which muscle activity and tendon-joint center moment arm distances are considered) could be described in simulation to provide a more faithful estimate of AT load. Furthermore, inclusion of B-mode ultrasound could be used to track changes in AT cross-sectional area and moment arm distance, which can account for significant differences between ankle moment and AT force [166], and even tendon or muscle fiber length change, which can be correlated to the true stress in the tissue.

Further development of the fully wearable system will focus on the addition of other useful signals such as joint angle (via inertial measurement unit) and EMG, miniaturization (at present, the AA batteries account for ~70% of the mass and volume and could be replaced by a lower-profile lithium-polymer battery), improved feature extraction techniques, and real-time feedback of tendon tension state to the user.

5.5 Conclusion

In this work, we developed and evaluated a novel method of assessing AT loading noninvasively by analyzing the tendon's response to burst vibrations on the skin surface.

Results demonstrate strong spatiotemporal agreement between our system's estimate of tendon load and proxy measures of the same (i.e., net ankle moment and calf EMG). Using machine learning, we were able to accurately estimate ankle moment during walking across a range of speeds from features of the tendon's burst response. Further, we developed a custom-designed, fully wearable system whose proof-of-concept results demonstrate similar trends to that of benchtop equipment experiments. These findings suggest that our approach can be an effective means of tracking tendon loading over time across a variety of everyday tasks, which may provide invaluable information for injury risk mitigation, rehabilitation strategies, and the study of movement impairments. Our approach could potentially be applied to other tendons, such as the patellar or biceps tendon, both of which also exhibit a high incidence of injury, or even perhaps other tissues like the plantar fascia and muscle, to similarly assess loading conditions and mechanical properties such as stiffness. Armed with this knowledge, an orthopedist could provide better injury diagnoses and prognoses; a physical therapist could precisely track the course of an athlete's recovery; an athlete could monitor the cumulative load on a particular muscle group; a physiatrist could peer deeper into movement disorders at the muscle-tendon unit level; and biomechanists could design better control strategies for robotic exoskeletons based on the mechanics of the underlying biology. As such, assessing tendon loading noninvasively could improve quality of life for countless individuals and put a spring back in their step.

CHAPTER 6. CONCLUSIONS AND FUTURE WORK

Through the course of this work, we have presented several approaches to assessing biomechanical loading in the lower limbs using noninvasive sensing techniques that have the potential to be made fully wearable. Looking forward, we can see many immediate and long-term strategies for carrying this work on and maximizing its potential. A few possible directions are considered below.

6.1 Pairing Orthoses with Joint Sounds for Differential Diagnosis

In the clinical world, the presence and extent of a pathology or deficit is often revealed through the use of a "stress test" or some similar examination. By challenging a physiological system of interest, physicians or clinicians can reveal deficiencies that might otherwise be nonobvious or latent. For example, a cardiologist might order an exercise stress test to reveal irregularities in cardiac mechanics (e.g., blood flow) to inform a differential diagnosis of heart disease [172], [173]. More pertinently, an orthopedist might assess the structural integrity of a joint using a combination of manual palpation maneuvers intended to load the joint in ways that will selectively stress certain tissues (e.g., the Lachman and anterior drawer tests of knee laxity in ACL tears [174]).

By the same logic, pairing customizable orthotic resistance with wearable sensing may reveal more information about a subject's underlying joint health or at least increase the richness of the dataset used for diagnostic or longitudinal health monitoring purposes. For example, applying differential mechanical load to an arthritic knee might reveal, via changes in wearable measurements of joint sounds or simple joint kinematics, clues as to

the progression of the disease or the patient's response to treatment beyond what the conventional maneuvers that a patient might be asked to perform (e.g., seated flexion-extension) might elicit. One possible approach to accomplishing this task in an out-of-clinic setting is to send patients home with a "smart" knee brace with adjustable stiffness capabilities, such as the one we developed and validated in an effort to bridge the work of CHAPTER 3 and CHAPTER 4 [175]. This knee brace was designed to be fully 3D-printable using flexible thermoplastic polyurethane, and it enabled the wearer to apply graded, direction-specific elastic resistance to the knee joint through the simple installation of elastic bands on either side of a central deflector frame (Figure 42{a,b}). A low-power, highly accurate, non-contact magnetic angle sensor was also embedded in the device to measure joint kinematics (Figure 42c). In a proof-of-concept study, we demonstrated that this brace was capable of effectively manipulating the load applied to the knee, which affected knee kinematics and muscle activity during ADLs (Figure 42d).

Pairing a device like this knee brace or the iAFO with a powerful wearable sensing modality like joint sounds or active acoustics could enhance the ability of those sensing techniques to extract clinically relevant information about joint health.

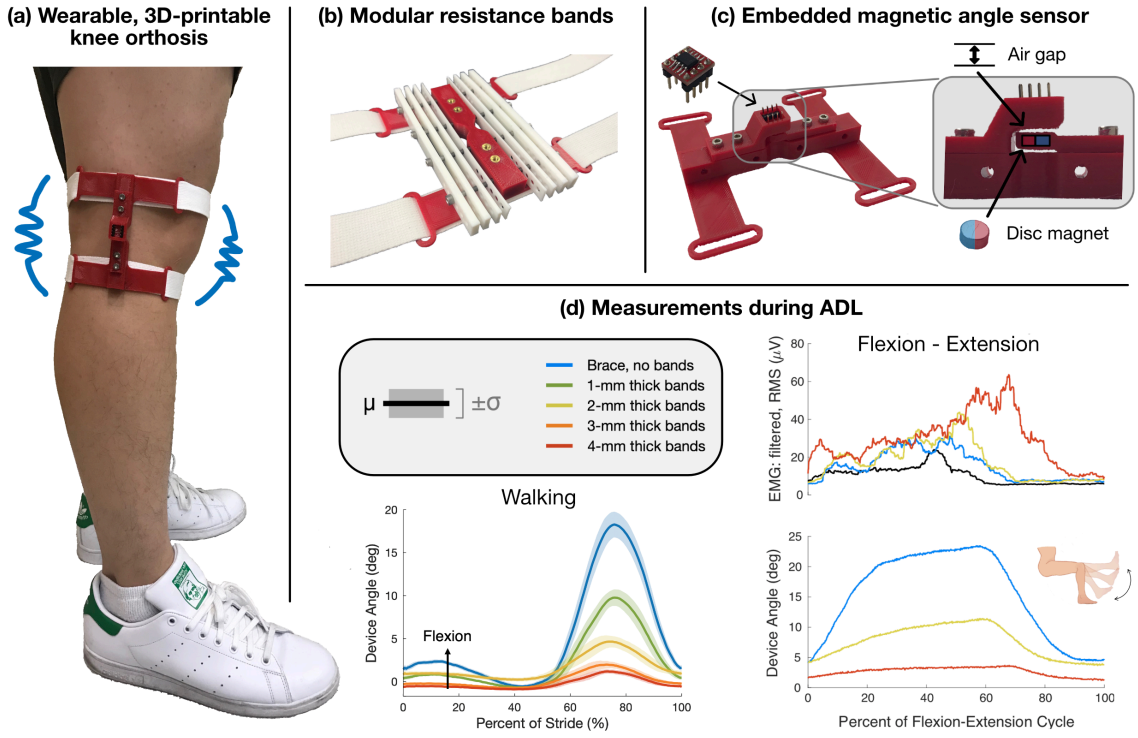

Figure 42. A fully 3-D printable, "smart" knee brace. (a) The knee brace acts as a torsional spring in parallel with the user's knee joint. (b) 3-D printed, flexible bands of different thicknesses can be mounted either side of the central frame, enabling customized and direction-specific reaction torque. (c) A non-contact magnetic angle sensor is embedded in the device to monitor knee kinematics. (d) Proof-of-concept results demonstrating the device's ability to modify knee biomechanical load during ADL.

6.2 Estimating Knee JRF During Gait Using Passive Acoustics (Joint Sounds)

Ongoing collaborative efforts between the Inan Research Lab and the biomechanics community at GT (in particular, the EPIC Lab under the leadership of Dr. Aaron Young) have attempted to integrate the modality of joint sounds into more sophisticated biomechanics applications, such as the estimation of knee JRF during locomotion (Figure 43). JRF is an important (albeit difficult) biomechanical parameter to monitor, as it dictates the progression of certain diseases like OA and can be used as an input parameter or target variable in the control scheme of an active exoskeleton. The current approach has been to

attach contact microphones at and around the knee and instruct subjects to walk on an instrumented treadmill in a gait analysis lab (Figure 43a). Using measurements of limb kinematics, kinetics, and EMG, a neuromuscular model of the lower body is elaborated, which outputs an informed estimate of knee JRF (Figure 43b). Acoustic features extracted from the filtered joint sound are then trained to estimate JRF on a step-by-step basis using sophisticated ML regression techniques (Figure 43c). Using a subject-dependent (and trial-dependent) model, estimation accuracy of $R^2 = 0.83$ has been achieved in a cohort of six healthy subjects. These data also demonstrate that characteristics of the joint sound are highly correlated with joint velocity (perhaps more so than JRF), so further development of the technique will be necessary to determine whether these sounds truly are dependent on how hard the bones are pressing together.

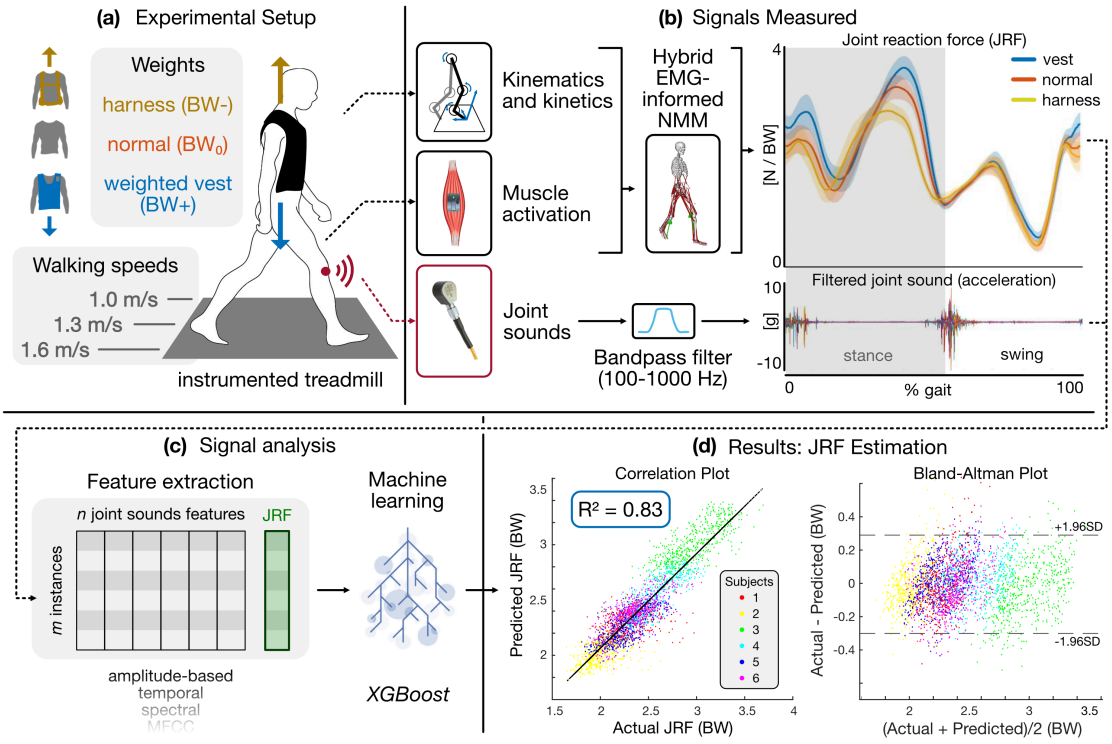

Figure 43. Conceptual overview of joint sounds-based knee JRF estimation approach. (a) In a gait analysis lab environment, a subject is instrumented with contact

accelerometers on the knee and performs a variety of locomotor tasks designed to expose the knee to differential load. (b) Measurements of limb kinematics, kinetics, and EMG are used to elaborate a neuromuscular model which produces informed estimates of JRF. (c) A landscape of features is extracted from the joint acoustic signal and used as the input for an ML model trained to estimate JRF as an output variable. (d) Preliminary, subject-depended model results demonstrate the potential of an ML-based estimation of knee JRF based purely on information from the joint sound.

6.3 ATLAS: Acoustic Tissue Loading Assessment System

In parallel with the passive acoustics approach detailed above, we have also conducted pilot experiments which leverage active acoustics, or vibrational analysis, to assess knee JRF during gait. This technique assumes that the forces experienced within the joint space are felt as equal and opposite forces on the tibia. The tibia is chosen as the "host structure" for vibrational analysis because it is an easily accessible tissue (i.e., not much muscle, fat, or other soft tissue lies superficial to it) and represents a simpler (and, therefore, potentially easier-to-model) structure than the knee joint itself. Much as in CHAPTER 5, this approach uses a paired vibration source and vibration sensor to measure the response of the underlying tissue to a particular excitation pattern. In this scenario, excitation of the tibia is provided by a high-bandwidth bone conduction transducer placed on the skin surface mid-tibia, vibrating the bone with a series of 100-ms chirps (bandwidth = 1000-2500 Hz) (Figure 44a). The vibration response of the tibia is then sensed some distance away on the tibia by a skin-mounted contact accelerometer (same as used in CHAPTER 4 and CHAPTER 5). A feature of this acoustic response (RMS amplitude of the chirp) is extracted for each 100-ms window, providing an effective sampling rate of 10 Hz. In a single-subject, proof-of-concept experiment, this feature demonstrates good spatiotemporal alignment with inverse dynamics-based estimates of knee JRF (i.e., similar waveform shape and timing) and even follows consistent trends in peak JRF as a function

of walking speed and carriage load (Figure 44b). A simple linear regression fit demonstrates that the acoustic response of the tibia (i.e., chirp RMS, which can be interpreted as how effectively a broadband vibration propagates through the beam) is highly correlated to estimates of knee JRF ($R^2 = 0.73$) (Figure 44c)—particularly the force in the antero-posterior direction, which would translate to a tensile / compressive bending stress on the anterior surface of the tibia (the measurement site), which may dominate local vibration response more than axial stresses. While this work is still very nascent, it demonstrates the potential for an active acoustics-based method to noninvasively acquire an otherwise very difficult-to-assess biomechanical loading state in the lower limb, even during ADLs.

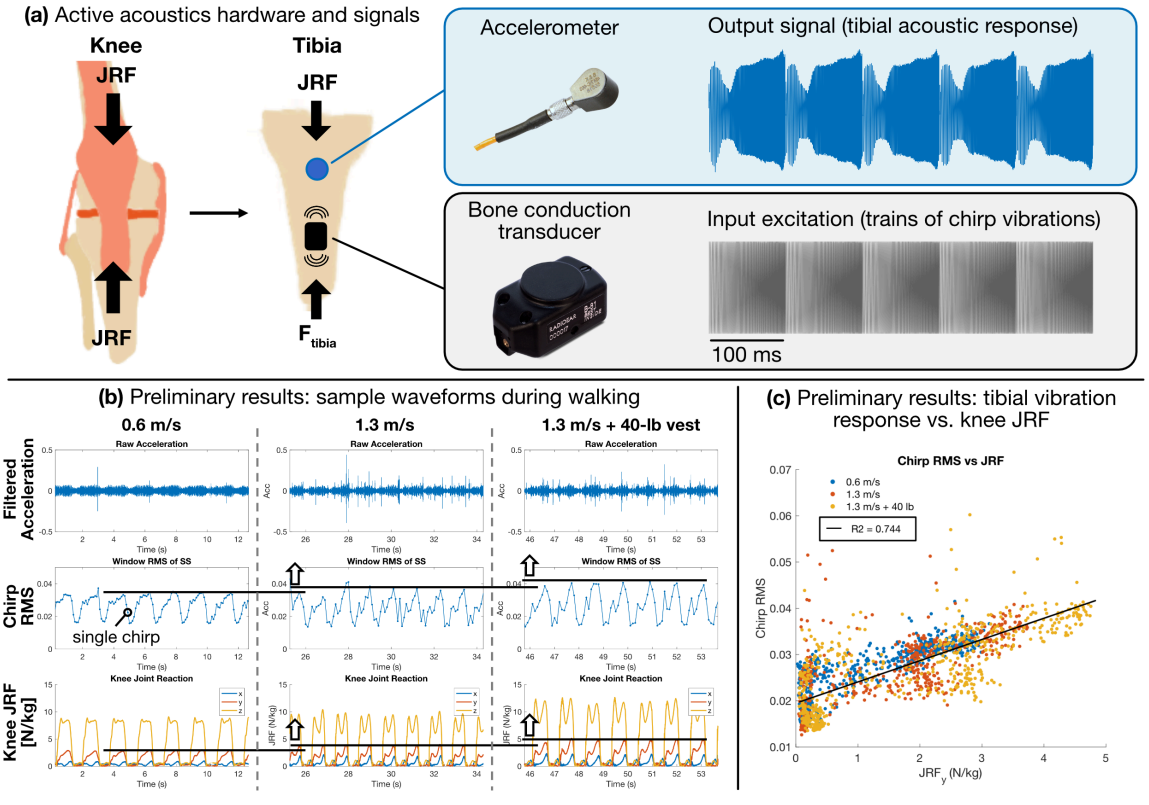

Figure 44. Conceptual overview of active acoustics-based knee JRF estimation approach. (a) It is assumed that knee JRF is experienced as an equal-and-opposite

force on the tibia. A contact accelerometer and bone conduction transducer are placed some distance apart on the skin superficial to the tibia. The transducer excites the bone with a train of chirp vibrations, and the tibia's response is measured. Preliminary results demonstrate (b) favorable spatiotemporal trends between estimates of knee JRF and tibial vibration response characteristics and (c) the potential for real-time estimation of JRF during walking.

This technology could be readily integrated into other "smart" braces, such as the one being developed and deployed by the Inan Research Lab for the measurement of joint sounds. We envision that this brace could operate in "passive" ("listening") mode when the priority is to assess structural changes in the knee related to joint health and, with the flip of a switch, operate in "active" ("interrogation") mode to estimate biomechanical loading states of interest, which could provide context for the joint's health status or inform clinical decisions related to activity level or the effectiveness of orthotic intervention.

6.4 Aspirations and Potential Impact of This Work

As the global population continues to grow and age, the healthcare system will inevitably bear a heavier burden. As such, it will become increasingly important to develop novel tools to monitor health status outside the physician's office or emergency room—a challenge for which wearable technology offers a clear and effective solution. This solution would involve systems that are capable of tracking patient status at home and over time, potentially offering predictive information for preventive care, accelerating recovery times, reducing the need for costly doctor visits, and paving the way for truly personalized medicine. The ambition of our work is to advance one small part of that frontier. And since the adverse effects of joint loading are so common and represent such a large component of healthcare costs, we hope that our efforts will eventually reach and benefit the greatest number of people possible, which is, and always will be, our guiding motivation.

REFERENCES

[1] G. Andersson and S. Watkins-Castillo, "The Burden of Musculoskeletal Diseases in the United States (BMUS)," *United States Bone Jt. Initiat. Rosemont,* 2014.

[2] M. Majewski, H. Susanne, and S. Klaus, "Epidemiology of athletic knee injuries: a 10-year study," *knee*, vol. 13, no. 3, pp. 184–188, 2006.

[3] J. M. Hootman, C. G. Helmick, K. E. Barbour, K. A. Theis, and M. A. Boring, "Updated projected prevalence of self-reported doctor-diagnosed arthritis and arthritis-attributable activity limitation among US adults, 2015–2040," *Arthritis Rheumatol.*, vol. 68, no. 7, pp. 1582–1587, 2016.

[4] A. J. Baliunas *et al.*, "Increased knee joint loads during walking are present in subjects with knee osteoarthritis," *Osteoarthr. Cartil.*, vol. 10, no. 7, pp. 573–579, 2002.

[5] J. P. A. Arokoski, J. S. Jurvelin, U. Väätäinen, and H. J. Helminen, "Normal and pathological adaptations of articular cartilage to joint loading," *Scand. J. Med. Sci. Sport. Rev. Artic.*, vol. 10, no. 4, pp. 186–198, 2000.

[6] A. D. Woolf and K. Åkesson, "Understanding the burden of musculoskeletal conditions: the burden is huge and not reflected in national health priorities," *BMJ Br. Med. J.*, vol. 322, no. 7294, p. 1079, 2001.

[7] M. M. Herzog, Z. Y. Kerr, S. W. Marshall, and E. A. Wikstrom, "Epidemiology of ankle sprains and chronic ankle instability," *J. Athl. Train.*, vol. 54, no. 6, pp. 603–610, 2019.

[8] A. G. Shamrock and M. Varacallo, "Achilles Tendon Ruptures," 2019. [Online]. Available: https://www.ncbi.nlm.nih.gov/books/NBK430844/.

[9] F. Sepúlveda, L. Sánchez, E. Amy, and W. Micheo, "Anterior cruciate ligament injury: return to play, function and long-term considerations," *Curr. Sports Med. Rep.*, vol. 16, no. 3, pp. 172–178, 2017.

[10] D. L. Riddle and S. M. Schappert, "Volume of ambulatory care visits and patterns of care for patients diagnosed with plantar fasciitis: a national study of medical

doctors," *Foot ankle Int.*, vol. 25, no. 5, pp. 303–310, 2004.

[11] G. M. Lyons, T. Sinkjær, J. H. Burridge, and D. J. Wilcox, "A review of portable FES-based neural orthoses for the correction of drop foot," *IEEE Trans. neural Syst. Rehabil. Eng.*, vol. 10, no. 4, pp. 260–279, 2002.

[12] F. E. Zajac, R. R. Neptune, and S. A. Kautz, "Biomechanics and muscle coordination of human walking: Part I: Introduction to concepts, power transfer, dynamics and simulations," *Gait Posture*, vol. 16, no. 3, pp. 215–232, 2002.

[13] R. Riemer, E. T. Hsiao-Wecksler, and X. Zhang, "Uncertainties in inverse dynamics solutions: a comprehensive analysis and an application to gait," *Gait Posture*, vol. 27, no. 4, pp. 578–588, 2008.

[14] F. C. Anderson and M. G. Pandy, "Static and dynamic optimization solutions for gait are practically equivalent," *J. Biomech.*, vol. 34, no. 2, pp. 153–161, 2001.

[15] P. V. Komi, "Relevance of in vivo force measurements to human biomechanics," *J. Biomech.*, vol. 23, pp. 23–34, Jan. 1990.

[16] P. Roriz, L. Carvalho, O. Frazão, J. L. Santos, and J. A. Simões, "From conventional sensors to fibre optic sensors for strain and force measurements in biomechanics applications: A review," *J. Biomech.*, vol. 47, no. 6, pp. 1251–1261, Apr. 2014.

[17] N. B. Bolus, C. N. Teague, O. T. Inan, and G. F. Kogler, "Instrumented Ankle–Foot Orthosis: Toward a Clinical Assessment Tool for Patient-Specific Optimization of Orthotic Ankle Stiffness," *IEEE/ASME Trans. Mechatronics*, vol. 22, no. 6, pp. 2492–2501, 2017.

[18] N. B. Bolus, H. K. Jeong, D. C. Whittingslow, and O. T. Inan, "A Glove-Based Form Factor for Collecting Joint Acoustic Emissions: Design and Validation," *Sensors*, vol. 19, no. 12, p. 2683, 2019.

[19] D. J. Farris and G. S. Sawicki, "The mechanics and energetics of human walking and running: a joint level perspective," *J. R. Soc. Interface*, p. rsif20110182, 2011.

[20] J. Perry, J. M. Burnfield, and L. M. Cabico, "Gait analysis: normal and pathological function," 1992.

[21] R. S. Snell, *Clinical anatomy by regions*. Lippincott Williams & Wilkins, 2011.

[22] J. D. Stewart, "Foot drop: where, why and what to do?," *Pract. Neurol.*, vol. 8, no. 3, pp. 158–169, 2008.

[23] F. D. Westhout, L. S. Paré, and M. E. Linskey, "Central causes of foot drop: rare and underappreciated differential diagnoses," *J. Spinal Cord Med.*, vol. 30, no. 1, pp. 62–66, 2007.

[24] J. Becker, S. James, R. Wayner, L. Osternig, and L.-S. Chou, "Biomechanical Factors Associated With Achilles Tendinopathy and Medial Tibial Stress Syndrome in Runners," *Am. J. Sports Med.*, vol. 45, no. 11, pp. 2614–2621, Sep. 2017.

[25] A. V. Lorimer and P. A. Hume, "Achilles Tendon Injury Risk Factors Associated with Running," *Sport. Med.*, vol. 44, no. 10, pp. 1459–1472, Oct. 2014.

[26] A. V. Lorimer, J. W. L. Keogh, and P. A. Hume, "Using stiffness to assess injury risk: comparison of methods for quantifying stiffness and their reliability in triathletes," *PeerJ*, vol. 6, p. e5845, Oct. 2018.

[27] A. V. Lorimer and P. A. Hume, "Stiffness as a Risk Factor for Achilles Tendon Injury in Running Athletes," *Sport. Med.*, vol. 46, no. 12, pp. 1921–1938, Dec. 2016.

[28] N. J. Lemme, N. Y. Li, S. F. DeFroda, J. Kleiner, and B. D. Owens, "Epidemiology of Achilles Tendon Ruptures in the United States: Athletic and Nonathletic Injuries From 2012 to 2016," *Orthop. J. Sport. Med.*, vol. 6, no. 11, p. 232596711880823, Nov. 2018.

[29] P. V. Komi, S. Fukashiro, and M. Järvinen, "Biomechanical loading of Achilles tendon during normal locomotion," *Clin. Sports Med.*, vol. 11, no. 3, pp. 521–31, Jul. 1992.

[30] R. D. Altman, "Overview of osteoarthritis," *Am. J. Med.*, vol. 83, no. 4, pp. 65–69, 1987.

[31] D. J. Hunter, J. J. McDougall, and F. J. Keefe, "The symptoms of osteoarthritis and the genesis of pain," *Rheum. Dis. Clin. North Am.*, vol. 34, no. 3, pp. 623–643, 2008.

[32] J. D. Hsu, J. W. Michael, J. R. Fisk, and A. A. of O. Surgeons, *AAOS Atlas of Orthoses and Assistive Devices*. Mosby/Elsevier, 2008.

[33] S. Hoppenfeld and V. L. Murthy, *Treatment and Rehabilitation of Fractures*. Lippincott Williams & Wilkins, 2000.

[34] R.-Y. Wang, P.-Y. Lin, C.-C. Lee, and Y.-R. Yang, "Gait and balance performance improvements attributable to ankle–foot orthosis in subjects with hemiparesis," *Am. J. Phys. Med. Rehabil.*, vol. 86, no. 7, pp. 556–562, 2007.

[35] J. Leung and A. Moseley, "Impact of ankle-foot orthoses on gait and leg muscle activity in adults with hemiplegia: systematic literature review," *Physiotherapy*, vol. 89, no. 1, pp. 39–55, 2003.

[36] L. A. B. Ferreira *et al.*, "Effect of ankle-foot orthosis on gait velocity and cadence of stroke patients: a systematic review," *J. Phys. Ther. Sci.*, vol. 25, no. 11, pp. 1503–1508, 2013.

[37] H. Abe, A. Michimata, K. Sugawara, N. Sugaya, and S.-I. Izumi, "Improving gait stability in stroke hemiplegic patients with a plastic ankle-foot orthosis," *Tohoku J. Exp. Med.*, vol. 218, no. 3, pp. 193–199, 2009.

[38] H. Gök, A. Küçükdeveci, H. Altinkaynak, G. Yavuzer, and S. Ergin, "Effects of ankle-foot orthoses on hemiparetic gait," *Clin. Rehabil.*, vol. 17, no. 2, pp. 137–139, 2003.

[39] C. A. Crabtree and J. S. Higginson, "Modeling neuromuscular effects of ankle foot orthoses (AFOs) in computer simulations of gait," *Gait Posture*, vol. 29, no. 1, pp. 65–70, 2009.

[40] T. Sumiya, Y. Suzuki, and T. Kasahara, "Stiffness control in posterior-type plastic ankle-foot orthoses: effect of ankle trimline Part 2: orthosis characteristics and orthosis/patient matching," *Prosthet. Orthot. Int.*, vol. 20, no. 2, pp. 132–137, 1996.

[41] S. Yamamoto, S. Miyazaki, and T. Kubota, "Quantification of the effect of the mechanical property of ankle-foot orthoses on hemiplegic gait," *Gait Posture*, vol. 1, no. 1, pp. 27–34, 1993.

[42] N. Eddison, N. Chockalingam, and S. Osborne, "Ankle foot orthosis–footwear

combination tuning: An investigation into common clinical practice in the United Kingdom," *Prosthet. Orthot. Int.*, p. 0309364613516486, 2014.

[43] N. Eddison and N. Chockalingam, "The effect of tuning ankle foot orthoses–footwear combination on the gait parameters of children with cerebral palsy," *Prosthet. Orthot. Int.*, vol. 37, no. 2, pp. 95–107, 2013.

[44] B. Meadows, "Tuning of rigid ankle-foot orthoses is essential," *Prosthet. Orthot. Int.*, vol. 38, no. 1, p. 83, 2014.

[45] A. J. Ries, T. F. Novacheck, and M. H. Schwartz, "A data driven model for optimal orthosis selection in children with cerebral palsy," *Gait Posture*, vol. 40, no. 4, pp. 539–544, 2014.

[46] T. Seel, J. Raisch, and T. Schauer, "IMU-based joint angle measurement for gait analysis," *Sensors*, vol. 14, no. 4, pp. 6891–6909, 2014.

[47] N. B. Bolus, G. F. Kogler, and O. T. Inan, "A novel method to assess angle sensor performance for wearable exoskeletal joint kinematics," in *Engineering in Medicine and Biology Society (EMBC), 2016 IEEE 38th Annual International Conference of the*, 2016, pp. 3109–3112.

[48] S. Crea, M. Donati, S. M. M. De Rossi, C. M. Oddo, and N. Vitiello, "A wireless flexible sensorized insole for gait analysis," *Sensors*, vol. 14, no. 1, pp. 1073–1093, 2014.

[49] E. S. Chumanov, C. D. Remy, and D. G. Thelen, "Computational techniques for using insole pressure sensors to analyse three-dimensional joint kinetics," *Comput. Methods Biomech. Biomed. Engin.*, vol. 13, no. 5, pp. 505–514, 2010.

[50] D. A. Winter, "Biomechanical Motor Patterns in Normal Walking," *J. Mot. Behav.*, vol. 15, no. 4, pp. 302–330, 1983.

[51] H. Kainz *et al.*, "Reliability of four models for clinical gait analysis," *Gait Posture*, vol. 54, pp. 325–331, May 2017.

[52] B. Koopman, H. J. Grootenboer, and H. J. De Jongh, "An inverse dynamics model for the analysis, reconstruction and prediction of bipedal walking," *J. Biomech.*, vol. 28, no. 11, pp. 1369–1376, 1995.

[53] W. E. Blodgett, “Auscultation of the knee joint,” *Bost. Med. Surg. J.*, vol. 146, no. 3, pp. 63–66, 1902.

[54] A. Steindler, “Auscultation of joints,” *JBJS*, vol. 19, no. 1, pp. 121–136, 1937.

[55] W. G. Kernohan, D. E. Beverland, G. F. McCoy, A. Hamilton, P. Watson, and R. A. B. Mollan, “Vibration arthrometry,” *Acta Orthop. Scand.*, vol. 61, no. 1, pp. 70–79, 1990.

[56] G. F. McCoy, J. D. McCrea, D. E. Beverland, W. G. Kernohan, and R. A. Mollan, “Vibration arthrography as a diagnostic aid in diseases of the knee. A preliminary report,” *J. Bone Joint Surg. Br.*, vol. 69, no. 2, pp. 288–293, 1987.

[57] S. Tavathia, R. M. Rangayyan, C. B. Frank, G. D. Bell, K. O. Ladly, and Y.-T. Zhang, “Analysis of knee vibration signals using linear prediction,” *IEEE Trans. Biomed. Eng.*, vol. 39, no. 9, pp. 959–970, 1992.

[58] O. T. Inan *et al.*, “Wearable knee health system employing novel physiological biomarkers,” *J. Appl. Physiol.*, vol. 124, no. 3, pp. 537–547, 2017.

[59] S. Hersek *et al.*, “Acoustical emission analysis by unsupervised graph mining: a novel biomarker of knee health status,” *IEEE Trans. Biomed. Eng.*, vol. 65, no. 6, pp. 1291–1300, 2018.

[60] H. K. Jeong, D. Whittingslow, and O. T. Inan, “b-Value: A Potential Biomarker for Assessing Knee-Joint Health Using Acoustical Emission Sensing,” *IEEE Sensors Lett.*, vol. 2, no. 4, pp. 1–4, 2018.

[61] D. Whittingslow, B. Semiz, L. Ponder, P. Vega-Fernandez, O. Inan, and S. Prahalad, “Knee Joint Sounds: A Non-Invasive Modality for Classifying Knee Joint Health in Juvenile Idiopathic Arthritis,” in *2017 ACR/ARHP Annual Meeting*, 2017, vol. 69.

[62] B. Semiz, S. Hersek, D. C. Whittingslow, L. A. Ponder, S. Prahalad, and O. T. Inan, “Using Knee Acoustical Emissions for Sensing Joint Health in Patients With Juvenile Idiopathic Arthritis: A Pilot Study,” *IEEE Sens. J.*, vol. 18, no. 22, pp. 9128–9136, 2018.

[63] D. Whittingslow, B. Semiz, L. Ponders, A. Wiens, O. Inan, and S. Prahalad, “Analysis and Implications of Non-Invasive Knee Acoustical Emissions in Juvenile

Idiopathic Arthritis," in *Arthritis & rheumatology*, 2017, vol. 69, pp. 90–91.

[64] D. C. Whittingslow, H.-K. Jeong, V. G. Ganti, N. J. Kirkpatrick, G. F. Kogler, and O. T. Inan, "Acoustic Emissions as a Non-invasive Biomarker of the Structural Health of the Knee," *Ann. Biomed. Eng.*, vol. 48, no. 1, pp. 225–235, 2020.

[65] H.-K. Jeong, M. B. Pouyan, D. C. Whittingslow, V. Ganti, and O. T. Inan, "Quantifying the Effects of Increasing Mechanical Stress on Knee Acoustical Emissions Using Unsupervised Graph Mining," *IEEE Trans. neural Syst. Rehabil. Eng.*, vol. 26, no. 3, pp. 594–601, 2018.

[66] S. Krishnan, R. M. Rangayyan, G. D. Bell, C. B. Frank, and K. O. Ladly, "Adaptive filtering, modelling and classification of knee joint vibroarthrographic signals for non-invasive diagnosis of articular cartilage pathology," *Med. Biol. Eng. Comput.*, vol. 35, no. 6, pp. 677–684, 1997.

[67] S. Krishnan, R. M. Rangayyan, G. D. Bell, and C. B. Frank, "Adaptive time-frequency analysis of knee joint vibroarthrographic signals for noninvasive screening of articular cartilage pathology," *IEEE Trans. Biomed. Eng.*, vol. 47, no. 6, pp. 773–783, 2000.

[68] L.-K. Shark, H. Chen, and J. Goodacre, "Discovering differences in acoustic emission between healthy and osteoarthritic knees using a four-phase model of sit-stand-sit movements," *Open Med. Inform. J.*, vol. 4, p. 116, 2010.

[69] Y. Athavale and S. Krishnan, "A telehealth system framework for assessing knee-joint conditions using vibroarthrographic signals," *Biomed. Signal Process. Control*, vol. 55, p. 101580, 2020.

[70] J. H. Friedman, "On bias, variance, 0/1—loss, and the curse-of-dimensionality," *Data Min. Knowl. Discov.*, vol. 1, no. 1, pp. 55–77, 1997.

[71] J. Friedman, T. Hastie, and R. Tibshirani, *The elements of statistical learning*, vol. 1, no. 10. Springer series in statistics New York, NY, USA:, 2001.

[72] T. Chen and C. Guestrin, "Xgboost: A scalable tree boosting system," in *Proceedings of the 22nd acm sigkdd international conference on knowledge discovery and data mining*, 2016, pp. 785–794.

[73] J. Elith, J. R. Leathwick, and T. Hastie, “A working guide to boosted regression trees,” *J. Anim. Ecol.*, vol. 77, no. 4, pp. 802–813, Jul. 2008.

[74] S. Whiteside, M. Allen, W. Barringer, W. D. Beiswenger, M. D. Brncick, and T. D. Bulgarelli, “Practice analysis of certified practitioners in the disciplines of orthotics and prosthetics,” *Alexandria, VA Am. Board Certif. Orthotics, Prosthetics Pedorth.*, 2007.

[75] E. Cakar, O. Durmus, L. Tekin, U. Dincer, and M. Z. Kiralp, “The ankle-foot orthosis improves balance and reduces fall risk of chronic spastic hemiparetic patients,” *Eur J Phys Rehabil Med*, vol. 46, no. 3, pp. 363–368, 2010.

[76] B. M. Rogozinski, J. R. Davids, R. B. Davis, G. G. Jameson, and D. W. Blackhurst, “The efficacy of the floor-reaction ankle-foot orthosis in children with cerebral palsy,” *J Bone Jt. Surg Am*, vol. 91, no. 10, pp. 2440–2447, 2009.

[77] C. Sackley, P. B. Disler, L. Turner-Stokes, D. T. Wade, N. Brittle, and T. Hoppitt, “Rehabilitation interventions for foot drop in neuromuscular disease,” *Cochrane Libr.*, 2009.

[78] J. L. O’Loughlin, Y. Robitaille, J.-F. Boivin, and S. Suissa, “Incidence of and risk factors for falls and injurious falls among the community-dwelling elderly,” *Am. J. Epidemiol.*, vol. 137, no. 3, pp. 342–354, 1993.

[79] B. H. Alexander, F. P. Rivara, and M. E. Wolf, “The cost and frequency of hospitalization for fall-related injuries in older adults,” *Am. J. Public Health*, vol. 82, no. 7, pp. 1020–1023, 1992.

[80] M. E. Daubney and E. G. Culham, “Lower-extremity muscle force and balance performance in adults aged 65 years and older,” *Phys. Ther.*, vol. 79, no. 12, p. 1177, 1999.

[81] V. L. Roger *et al.*, “Heart disease and stroke statistics—2011 update a report from the American Heart Association,” *Circulation*, vol. 123, no. 4, pp. e18–e209, 2011.

[82] D. J. J. Bregman, J. Harlaar, C. G. M. Meskers, and V. De Groot, “Spring-like Ankle Foot Orthoses reduce the energy cost of walking by taking over ankle work,” *Gait Posture*, vol. 35, no. 1, pp. 148–153, 2012.

[83] N. G. Harper, E. R. Esposito, J. M. Wilken, and R. R. Neptune, “The influence of ankle-foot orthosis stiffness on walking performance in individuals with lower-limb impairments,” *Clin. Biomech.*, vol. 29, no. 8, pp. 877–884, 2014.

[84] J. De Vries, “Evaluation of lower leg orthosis use following cerebro-vascular accident,” *Int. J. Rehabil. Res.*, vol. 14, no. 3, pp. 239–243, 1991.

[85] J. F. Geboers, M. R. Drost, F. Spaans, H. Kuipers, and H. A. Seelen, “Immediate and long-term effects of ankle-foot orthosis on muscle activity during walking: a randomized study of patients with unilateral foot drop,” *Arch. Phys. Med. Rehabil.*, vol. 83, no. 2, pp. 240–245, 2002.

[86] A. Young and D. Ferris, “State-of-the-art and Future Directions for Robotic Lower Limb Exoskeletons,” *IEEE Trans Neural Syst Rehabil Eng.*, 2016.

[87] T. Yan, M. Cempini, C. M. Oddo, and N. Vitiello, “Review of assistive strategies in powered lower-limb orthoses and exoskeletons,” *Rob. Auton. Syst.*, vol. 64, pp. 120–136, 2015.

[88] K. A. Shorter, J. Xia, E. T. Hsiao-Wecksler, W. K. Durfee, and G. F. Kogler, “Technologies for powered ankle-foot orthotic systems: Possibilities and challenges,” *IEEE/ASME Trans. Mechatronics*, vol. 18, no. 1, pp. 337–347, 2013.

[89] A. Pennycott, D. Wyss, H. Vallery, V. Klamroth-Marganska, and R. Riener, “Towards more effective robotic gait training for stroke rehabilitation: a review,” *J. Neuroeng. Rehabil.*, vol. 9, no. 1, p. 1, 2012.

[90] M. Goldfarb and W. K. Durfee, “Design of a controlled-brake orthosis for FES-aided gait,” *IEEE Trans. Rehabil. Eng.*, vol. 4, no. 1, pp. 13–24, 1996.

[91] D. P. Ferris, K. E. Gordon, G. S. Sawicki, and A. Peethambaran, “An improved powered ankle–foot orthosis using proportional myoelectric control,” *Gait Posture*, vol. 23, no. 4, pp. 425–428, 2006.

[92] K. A. Shorter, G. F. Kogler, E. Loth, W. K. Durfee, and E. T. Hsiao-Wecksler, “A portable powered ankle-foot orthosis for rehabilitation,” *J. Rehabil. Res. Dev*, vol. 48, no. 4, pp. 459–472, 2011.

[93] A. Roy *et al.*, “Robot-aided neurorehabilitation: a novel robot for ankle

rehabilitation," *Robot. IEEE Trans.*, vol. 25, no. 3, pp. 569–582, 2009.

[94] M. Moltedo, T. Bacek, K. Junius, B. Vanderborght, and D. Lefeber, "Mechanical design of a lightweight compliant and adaptable active ankle foot orthosis," in *Biomedical Robotics and Biomechatronics (BioRob), 2016 6th IEEE International Conference on*, 2016, pp. 1224–1229.

[95] N. Vitiello *et al.*, "Functional Design of a Powered Elbow Orthosis towards its Clinical Employment," *IEEE/ASME Trans. Mechatronics*, vol. 21, no. 4, 2016.

[96] D. P. Ferris, J. M. Czerniecki, B. Hannaford, and U. of Washington, "An ankle-foot orthosis powered by artificial pneumatic muscles," *J. Appl. Biomech.*, vol. 21, no. 2, p. 189, 2005.

[97] J. A. Blaya and H. Herr, "Adaptive control of a variable-impedance ankle-foot orthosis to assist drop-foot gait," *IEEE Trans. neural Syst. Rehabil. Eng.*, vol. 12, no. 1, pp. 24–31, 2004.

[98] M. Cestari, D. Sanz-Merodio, J. C. Arevalo, and E. Garcia, "An adjustable compliant joint for lower-limb exoskeletons," *IEEE/ASME Trans. Mechatronics*, vol. 20, no. 2, pp. 889–898, 2015.

[99] S. Yamamoto, M. Ebina, M. Iwasaki, S. Kubo, H. Kawai, and T. Hayashi, "Comparative Study of Mechanical Characteristics of Plastic AFOs," *JPO J. Prosthetics Orthot.*, vol. 5, no. 2, p. 59, 1993.

[100] M. D. J. J. Bregman, V. De Groot, P. Van Diggele, H. Meulman, H. Houdijk, and J. Harlaar, "Polypropylene Ankle Foot Orthoses to Overcome Drop-Foot Gait in Central Neurological Patients: A Mechanical and Functional Evaluation," *Prosthet. Orthot. Int.*, vol. 34, no. 3, pp. 293–304, 2010.

[101] S. Yamamoto, M. Ebina, S. Miyazaki, H. Kawai, and T. Kubota, "Development of a New Ankle-Foot Orthosis with Dorsiflexion Assist, Part 1: Desirable Characteristics of Ankle-Foot Orthoses for Hemiplegic Patients," *JPO J. Prosthetics Orthot.*, vol. 9, no. 4, pp. 174–179, 1997.

[102] J. Romkes and R. Brunner, "Comparison of a dynamic and a hinged ankle–foot orthosis by gait analysis in patients with hemiplegic cerebral palsy," *Gait Posture*, vol. 15, no. 1, pp. 18–24, 2002.

[103] S. Fatone, S. A. Gard, and B. S. Malas, “Effect of ankle-foot orthosis alignment and foot-plate length on the gait of adults with poststroke hemiplegia,” *Arch. Phys. Med. Rehabil.*, vol. 90, no. 5, pp. 810–818, 2009.

[104] S. Miyazaki, S. Yamamoto, and T. Kubota, “Effect of ankle-foot orthosis on active ankle moment in patients with hemiparesis,” *Med. Biol. Eng. Comput.*, vol. 35, no. 4, pp. 381–385, 1997.

[105] S. Yamamoto, N. Tomokiyo, T. Yasui, and T. Kawaguchi, “Effects of plantar flexion resistive moment generated by an ankle-foot orthosis with an oil damper on the gait of stroke patients: a pilot study,” *Prosthet. Orthot. Int.*, vol. 37, no. 3, pp. 212–221, 2013.

[106] T. Kitago and J. W. Krakauer, “Motor learning principles for neurorehabilitation,” in *Handbook of clinical neurology*, vol. 110, Elsevier, 2013, pp. 93–103.

[107] A. J. Bastian, “Understanding sensorimotor adaptation and learning for rehabilitation,” *Curr. Opin. Neurol.*, vol. 21, no. 6, p. 628, 2008.

[108] D. S. Reisman, H. J. Block, and A. J. Bastian, “Interlimb coordination during locomotion: what can be adapted and stored?,” *J. Neurophysiol.*, vol. 94, no. 4, pp. 2403–2415, 2005.

[109] G. S. Sawicki, K. E. Gordon, and D. P. Ferris, “Powered lower limb orthoses: applications in motor adaptation and rehabilitation,” in *Rehabilitation Robotics, 2005. ICORR 2005. 9th International Conference on*, 2005, pp. 206–211.

[110] A. D. Kuo and J. M. Donelan, “Dynamic principles of gait and their clinical implications,” *Phys. Ther.*, vol. 90, no. 2, pp. 157–74, Feb. 2010.

[111] R. L. Waters and S. Mulroy, “The energy expenditure of normal and pathologic gait,” *Gait Posture*, vol. 9, no. 3, pp. 207–231, 1999.

[112] S. F. Tyson, E. Sadeghi-Demneh, and C. J. Nester, “A systematic review and meta-analysis of the effect of an ankle-foot orthosis on gait biomechanics after stroke,” *Clin. Rehabil.*, vol. 27, no. 10, pp. 879–891, 2013.

[113] M. L. Singer, T. Kobayashi, L. S. Lincoln, M. S. Orendurff, and K. B. Foreman, “The effect of ankle–foot orthosis plantarflexion stiffness on ankle and knee joint

kinematics and kinetics during first and second rockers of gait in individuals with stroke," *Clin. Biomech.*, vol. 29, no. 9, pp. 1077–1080, 2014.

[114] M. Rafiaei *et al.*, "The gait and energy efficiency of stance control knee–ankle–foot orthoses: A literature review," *Prosthet. Orthot. Int.*, vol. 40, no. 2, pp. 202–214, 2016.

[115] M. B. Wiggin, G. S. Sawicki, and S. H. Collins, "An exoskeleton using controlled energy storage and release to aid ankle propulsion," in *Rehabilitation Robotics (ICORR), 2011 IEEE International Conference on*, 2011, pp. 1–5.

[116] S. H. Collins, M. B. Wiggin, and G. S. Sawicki, "Reducing the energy cost of human walking using an unpowered exoskeleton," *Nature*, vol. 522, no. 7555, p. 212, 2015.

[117] D. J. J. Bregman, A. Rozumalski, D. Koops, V. De Groot, M. Schwartz, and J. Harlaar, "A new method for evaluating ankle foot orthosis characteristics: BRUCE," *Gait Posture*, vol. 30, no. 2, pp. 144–149, 2009.

[118] T. Morita and S. Sugano, "Design and development of a new robot joint using a mechanical impedance adjuster," in *Proceedings of 1995 IEEE International Conference on Robotics and Automation*, 1995, vol. 3, pp. 2469–2475 vol.3.

[119] Y. Ding *et al.*, "Biomechanical and physiological evaluation of multi-joint assistance with soft exosuits," *IEEE Trans. neural Syst. Rehabil. Eng.*, vol. 25, no. 2, pp. 119–130, 2017.

[120] A. T. Asbeck, S. M. M. De Rossi, K. G. Holt, and C. J. Walsh, "A biologically inspired soft exosuit for walking assistance," *Int. J. Rob. Res.*, vol. 34, no. 6, pp. 744–762, 2015.

[121] M. L. Chu, I. A. Gradisar, M. R. Railey, and G. F. Bowling, "Detection of knee joint diseases using acoustical pattern recognition technique," *J. Biomech.*, vol. 9, no. 3, pp. 113–114, 1976.

[122] C. B. Frank, R. M. Rangayyan, and G. D. Bell, "Analysis of knee joint sound signals for non-invasive diagnosis of cartilage pathology," *IEEE Eng. Med. Biol. Mag.*, vol. 9, no. 1, pp. 65–68, 1990.

[123] H. Töreyin, H. K. Jeong, S. Hersek, C. N. Teague, and O. T. Inan, "Quantifying the

consistency of wearable knee acoustical emission measurements during complex motions," *IEEE J. Biomed. Heal. informatics*, vol. 20, no. 5, pp. 1265–1272, 2016.

[124] C. N. Teague *et al.*, "Novel methods for sensing acoustical emissions from the knee for wearable joint health assessment," *IEEE Trans. Biomed. Eng.*, vol. 63, no. 8, pp. 1581–1590, 2016.

[125] C. Teague *et al.*, "Novel approaches to measure acoustic emissions as biomarkers for joint health assessment," in *Wearable and Implantable Body Sensor Networks (BSN), 2015 IEEE 12th International Conference on*, 2015, pp. 1–6.

[126] T. K. Koo and M. Y. Li, "A guideline of selecting and reporting intraclass correlation coefficients for reliability research," *J. Chiropr. Med.*, vol. 15, no. 2, pp. 155–163, 2016.

[127] G. G. Koch, "Intraclass correlation coefficient," *Wiley StatsRef Stat. Ref. Online*, 2014.

[128] T. J. Roberts, "Contribution of elastic tissues to the mechanics and energetics of muscle function during movement," *J. Exp. Biol.*, vol. 219, no. 2, pp. 266–275, Jan. 2016.

[129] T. J. Roberts, "The integrated function of muscles and tendons during locomotion," *Comp. Biochem. Physiol. Part A Mol. Integr. Physiol.*, vol. 133, no. 4, pp. 1087–1099, Dec. 2002.

[130] A. Wilson and G. Lichtwark, "The anatomical arrangement of muscle and tendon enhances limb versatility and locomotor performance," *Philos. Trans. R. Soc. Lond. B. Biol. Sci.*, vol. 366, no. 1570, pp. 1540–53, May 2011.

[131] T. J. Roberts and E. Azizi, "Flexible mechanisms: the diverse roles of biological springs in vertebrate movement," *J. Exp. Biol.*, vol. 214, no. 3, pp. 353–361, Feb. 2011.

[132] T. J. Roberts and N. Konow, "How tendons buffer energy dissipation by muscle," *Exerc. Sport Sci. Rev.*, vol. 41, no. 4, pp. 186–93, Oct. 2013.

[133] N. Konow and T. J. Roberts, "The series elastic shock absorber: tendon elasticity modulates energy dissipation by muscle during burst deceleration," *Proc. R. Soc. B*

Biol. Sci., vol. 282, no. 1804, p. 20142800, Apr. 2015.

[134] M. O'Brien, "The anatomy of the Achilles tendon," *Foot Ankle Clin.*, vol. 10, no. 2, pp. 225–38, Jun. 2005.

[135] R. F. Ker, R. M. Alexander, and M. B. Bennett, "Why are mammalian tendons so thick?," *J. Zool.*, vol. 216, no. 2, pp. 309–324, Oct. 1988.

[136] T. A. L. Wren, S. A. Yerby, G. S. Beaupré, and D. R. Carter, "Mechanical properties of the human achilles tendon," *Clin. Biomech.*, vol. 16, no. 3, pp. 245–251, Mar. 2001.

[137] P. Kannus and L. Józsa, "Histopathological changes preceding spontaneous rupture of a tendon. A controlled study of 891 patients," *J. Bone Joint Surg. Am.*, vol. 73, no. 10, pp. 1507–25, Dec. 1991.

[138] S. B. Weinfeld, "Achilles Tendon Disorders," *Med. Clin. North Am.*, vol. 98, no. 2, pp. 331–338, Mar. 2014.

[139] S. M. Raikin, D. N. Garras, and P. V. Krapchev, "Achilles Tendon Injuries in a United States Population," *Foot Ankle Int.*, vol. 34, no. 4, pp. 475–480, Apr. 2013.

[140] C. Rosso *et al.*, "Long-term biomechanical outcomes after Achilles tendon ruptures," *Knee Surgery, Sport. Traumatol. Arthrosc.*, vol. 23, no. 3, pp. 890–898, Mar. 2015.

[141] C. Holm, M. Kjaer, and P. Eliasson, "Achilles tendon rupture - treatment and complications: A systematic review," *Scand. J. Med. Sci. Sports*, vol. 25, no. 1, pp. e1–e10, Feb. 2015.

[142] O. C. Dams *et al.*, "The recovery after Achilles tendon rupture: a protocol for a multicenter prospective cohort study," *BMC Musculoskelet. Disord.*, vol. 20, no. 1, p. 69, Dec. 2019.

[143] B. Frankewycz *et al.*, "Achilles tendon elastic properties remain decreased in long term after rupture," *Knee Surgery, Sport. Traumatol. Arthrosc.*, vol. 26, no. 7, pp. 2080–2087, Jul. 2018.

[144] D. P. Trofa, J. C. Miller, E. S. Jang, D. R. Woode, J. K. Greisberg, and J. T. Vosseller, "Professional Athletes' Return to Play and Performance After Operative Repair of an Achilles Tendon Rupture," *Am. J. Sports Med.*, vol. 45, no. 12, pp. 2864–2871, Oct. 2017.

[145] J. A. Zellers, M. R. Carmont, and K. Grävare Silbernagel, "Return to play post-Achilles tendon rupture: a systematic review and meta-analysis of rate and measures of return to play," *Br. J. Sports Med.*, vol. 50, no. 21, pp. 1325–1332, Nov. 2016.

[146] N. H. Amin, A. B. Old, L. P. Tabb, R. Garg, N. Toossi, and D. L. Cerynik, "Performance Outcomes After Repair of Complete Achilles Tendon Ruptures in National Basketball Association Players," *Am. J. Sports Med.*, vol. 41, no. 8, pp. 1864–1868, Aug. 2013.

[147] P. V. Komi, A. Belli, V. Huttunen, R. Bonnefoy, A. Geyssant, and J. R. Lacour, "Optic fibre as a transducer of tendomuscular forces," *Eur. J. Appl. Physiol. Occup. Physiol.*, vol. 72, no. 3, pp. 278–280, 1996.

[148] T. Finni, P. V. Komi, and J. Lukkariniemi, "Achilles tendon loading during walking: application of a novel optic fiber technique," *Eur. J. Appl. Physiol.*, vol. 77, no. 3, pp. 289–291, Feb. 1998.

[149] Å. Fröberg, P. Komi, M. Ishikawa, T. Movin, and A. Arndt, "Force in the Achilles Tendon During Walking With Ankle Foot Orthosis," *Am. J. Sports Med.*, vol. 37, no. 6, pp. 1200–1207, Jun. 2009.

[150] K. Killian Bouillard, A. Nordez, and F. Hug, "Estimation of Individual Muscle Force Using Elastography," *PLoS One*, vol. 6, no. 12, p. e29261, Dec. 2011.

[151] M. Salman and K. Sabra, "Non-invasive monitoring of Achille's tendon stiffness variations *in-vivo* using mechanical vibrations," *J. Acoust. Soc. Am.*, vol. 137, no. 4, pp. 2424–2424, Apr. 2015.

[152] C. Helfenstein-Didier *et al.*, "*In vivo* quantification of the shear modulus of the human Achilles tendon during passive loading using shear wave dispersion analysis," *Phys. Med. Biol.*, vol. 61, no. 6, pp. 2485–2496, Mar. 2016.

[153] J. A. Martin *et al.*, "Gauging force by tapping tendons," *Nat. Commun.*, vol. 9, no. 1, p. 1592, Dec. 2018.

[154] E. M. Keuler, I. F. Loegering, J. A. Martin, J. D. Roth, and D. G. Thelen, "Shear Wave Predictions of Achilles Tendon Loading during Human Walking," *Sci. Rep.*, vol. 9, no. 1, p. 13419, Dec. 2019.

[155] L. D. Duffell, N. Hope, and A. H. McGregor, "Comparison of kinematic and kinetic parameters calculated using a cluster-based model and Vicon's plug-in gait," *Proc. Inst. Mech. Eng. Part H J. Eng. Med.*, vol. 228, no. 2, pp. 206–210, Jan. 2014.

[156] H. J. Woltring, "A Fortran package for generalized, cross-validatory spline smoothing and differentiation," *Adv. Eng. Softw.*, vol. 8, no. 2, pp. 104–113, Apr. 1986.

[157] D. Winter, *Biomechanics and motor control of human movement*. 2009.

[158] A. Leardini, C. Belvedere, F. Nardini, N. Sancisi, M. Conconi, and V. Parenti-Castelli, "Kinematic models of lower limb joints for musculo-skeletal modelling and optimization in gait analysis," *J. Biomech.*, vol. 62, pp. 77–86, Sep. 2017.

[159] I. W. Charlton, P. Tate, P. Smyth, and L. Roren, "Repeatability of an optimised lower body model," *Gait Posture*, vol. 20, no. 2, pp. 213–221, Oct. 2004.

[160] C. Wright, A. Seitz, B. Arnold, and L. Michener, "Repearability of Ankle Joint Kinematic Data at Heel Strike Using the Vicon Plug-in Gait Model," Jan. 2011.

[161] B. J. Raiteri, A. G. Cresswell, and G. A. Lichtwark, "Ultrasound reveals negligible cocontraction during isometric plantar flexion and dorsiflexion despite the presence of antagonist electromyographic activity," *J. Appl. Physiol.*, vol. 118, no. 10, pp. 1193–1199, May 2015.

[162] B. J. Raiteri, F. Hug, A. G. Cresswell, and G. A. Lichtwark, "Quantification of muscle co-contraction using supersonic shear wave imaging," *J. Biomech.*, vol. 49, no. 3, pp. 493–495, Feb. 2016.

[163] A. Erdemir, S. McLean, W. Herzog, and A. J. van den Bogert, "Model-based estimation of muscle forces exerted during movements," *Clin. Biomech.*, vol. 22, no. 2, pp. 131–154, Feb. 2007.

[164] J. Duysens, M. Trippel, G. A. Horstmann, and V. Dietz, "Gating and reversal of reflexes in ankle muscles during human walking," *Exp. Brain Res.*, vol. 82, no. 2,

pp. 351–358, Oct. 1990.

[165] S. Fukashiro, P. V. Komi, M. Järvinen, and M. Miyashita, “Comparison between the directly measured achilles tendon force and the tendon force calculated from the ankle joint moment during vertical jumps,” *Clin. Biomech.*, vol. 8, no. 1, pp. 25–30, Jan. 1993.

[166] K. Rasske, D. G. Thelen, and J. R. Franz, “Variation in the human Achilles tendon moment arm during walking,” *Comput. Methods Biomech. Biomed. Engin.*, vol. 20, no. 2, pp. 201–205, Jan. 2017.

[167] L. Breiman, “Bagging Predictors,” *Mach. Learn.*, vol. 24, no. 2, pp. 123–140, 1996.

[168] D. T. Kirkendall and W. E. Garrett, “Function and biomechanics of tendons,” *Scand. J. Med. Sci. Sports*, vol. 7, no. 2, pp. 62–66, Jan. 2007.

[169] G. M. Revel, A. Scalise, and L. Scalise, “Measurement of stress–strain and vibrational properties of tendons,” *Meas. Sci. Technol.*, vol. 14, no. 8, pp. 1427–1436, Aug. 2003.

[170] J. A. Hannafin and S. P. Arnoczky, “Effect of cyclic and static tensile loading on water content and solute diffusion in canine flexor tendons: An in Vitro study,” *J. Orthop. Res.*, vol. 12, no. 3, pp. 350–356, May 1994.

[171] S. Han *et al.*, “Changes in ADC Caused by Tensile Loading of Rabbit Achilles Tendon: Evidence for Water Transport,” *J. Magn. Reson.*, vol. 144, no. 2, pp. 217–227, Jun. 2000.

[172] S.-J. Kim and H.-K. Kim, “Reliability of the anterior drawer test, the pivot shift test, and the Lachman test.,” *Clin. Orthop. Relat. Res.*, no. 317, pp. 237–242, 1995.

[173] J. W. Katz and R. J. Fingeroth, “The diagnostic accuracy of ruptures of the anterior cruciate ligament comparing the Lachman test, the anterior drawer sign, and the pivot shift test in acute and chronic knee injuries,” *Am. J. Sports Med.*, vol. 14, no. 1, pp. 88–91, 1986.

[174] R. A. Magnussen, E. K. Reinke, L. J. Huston, M. Group, T. E. Hewett, and K. P. Spindler, “Factors Associated With High-Grade Lachman, Pivot Shift, and Anterior Drawer at the Time of Anterior Cruciate Ligament Reconstruction,” *Arthroscopy*,

vol. 32, no. 6, pp. 1080–1085, Jun. 2016.

[175] N. B. Bolus, V. G. Ganti, and O. T. Inan, “A 3D-printed, adjustable-stiffness knee brace with embedded magnetic angle sensor,” in *2018 40th Annual International Conference of the IEEE Engineering in Medicine and Biology Society (EMBC)*, 2018, pp. 1624–1627.